



I-ImaS – Workpackage 3

Deliverable No D.8

“Translating information signatures to a sequence of well-defined processing functions”

Last Updated: 23-Feb-2005

I-ImaS: Intelligent Imaging Sensors for Industry, Health and Security

FP6-505593-1

Work package No.3 – Image Analysis

Deliverable D.8 – “Translating information signatures to a sequence of well-defined processing functions”

Corresponding Author: Harris Georgiou (UOA/CTI)

mailto: xgeorgio@di.uoa.gr

Contributing Author: Angela Peterzol (UoT), sections 2.0 & 2.9.*

mailto: peterzol@ts.infn.it

Last Updated: 25-Feb-2005

Contents:

Executive Summary	4
1. General Task Overview	5
2. Overview of work plan	6
2.1 Web-based mammographic image database (DB1)	6
2.2 Experiment documentation (RIEDS)	7
2.3 Preliminary phantom image database (DB2)	7
2.4 SimModel-1A: Exposure Simulation	8
2.4.1 Model Design Parameters	9
2.4.2 Model Overview	14
2.4.3 Results and Verification	16
2.5 PredModel-1A: Textural Features Extraction	18
2.5.1 Model Design Parameters – Progressive Image Scanning	18
2.5.2 Textural Feature Functions	19
2.5.3 Intermediate 2-D Texture Matrices	21
2.6 PredModel-1B: Textural Features Evaluation	27
2.6.1 Texture “signatures” against exposure rates	27
2.6.2 Comparative results & discussion	39
2.7 Real breast tissue image database (DB3)	41
2.8 PredModel-2A/B: Textural Features Validation	43
2.8.1 Confirmation of SimModel-1A over exposure and OD response	45
2.8.2 Global statistics against exposure rates	48
2.8.3 Texture “signatures” against exposure rates	53
2.8.4 Effects of special areas and background artifacts	65
2.9 Textural characterization of images of mammographic test objects	74
2.9.1 Study of the effect of pre-processing	75
2.9.2 Study of statistical quantities for feature detection	84
3. Implementation & Performance Issues	94
4. Further Progress Requirements	97
Suggestive References	98
Appendix A: RIEDS – Radiographic Imaging Evaluation & Documentation System	100
Appendix B: PredModel-1A: Sample source code for textural feature functions (Matlab)	116

Executive Summary

The current study focuses on the core issue of identifying information signatures that can capture the content-rich image data and translate them into a compact set of processing functions that can be implemented and embedded into the sensor IC logic.

The preliminary image analysis was based on publicly available, well-documented sets of mammographic images. A complete and thorough documentation set of templates was designed in order to record and file all equipment-related information during image acquisition experiments, as well as the technical and clinical aspects of image quality assessments.

A simulation model (SimModel-1A) was created for processing initial mammographic images, acquired at optimal exposure settings, and produce simulated versions of the same image at overexposed and underexposed conditions. The model was verified by comparing its results with a real independent set of phantom images, acquired at similar overexposure and underexposure settings.

Simulated image sets, along with the initial (optimal) images, were used as the base for PredModel-1A. This new model was used to implement a full set of 20 textural feature functions, including 1st order statistics, signal "roughness" metrics, as well as a set of specially designed synthetic features. Image processing and feature values extraction was adapted according to the real functionality and data acquisition of the final line-scanning system.

Intermediate 2-D texture matrices from PredModel-1A were reduced to 1-D simple curves and combined with the simulation model for acquiring all texture features at different exposure settings. The combined system, PredModel-1B, produced clear results on the main issue of establishing a consistent functional link between texture analysis and exposure conditions. A set of 8 most prominent candidates, from the total of 20 textural feature functions, was identified as well-suited for this task.

Finally, the preliminary textural feature results and selections were confirmed by applying the same analytical procedure over a new image database (DB3), containing X-ray images of real breast tissue samples, exposed at various ranges of kVp and mAs.

Implementation of all feature functions was confirmed to be fully compatible with the sensor IC requirement for SIMD architecture. However, before the choices for feedback control are finalized, further verification and adjustment test have to be conducted, using real (instead of simulated) sets of sub-optimally exposed X-ray images.

1. General Task Overview

With relation to the core image analysis process, sensor intelligence is based on a limited set of fast and efficient textural features that can encode the bulk of the information content of the underlying image in real-time. Limited hardware and software resources will be available in the final sensor IC design, thus only simple, stable and robust texture functions were to be investigated as possible candidates.

In order to study textural features performance and dependence with X-ray exposure parameters, a standard, publicly available, image database had to be used instead of real experimentally acquired images. Preliminary analysis on this initial image set will be followed by clinical performance evaluation of the same feature functions on the experimental image sets, when they are available.

As the sensor specifications and performance profile will also be available later, a compact simulation model had to be designed and implemented in order to produce sub-optimal exposure image sets from the initial (optimal) images. The simulation model was designed according to the performance profiles of current digital mammographic equipment and the results were verified independently by comparing them with actual sub-optimal exposure test images, acquired by a digital mammographic system, using a quality-assessment mammographic phantom.

WP3 tasks:

1. Acquire a web-available mammographic image database for preliminary analysis.
2. Identify a set of suitable texture feature functions for image analysis.
3. Evaluate feature values and select best candidates for further study.

Current Specifications & Constraints:

- Publicly available mammographic databases contain images of optimal exposure only, usually through conventional Automatic Exposure Rate Control (AERC).
- Images of sub-optimal exposures must be simulated in order to investigate effects on textural feature functions.
- Final set of textural feature functions will be verified when new sensor-specific image sets, acquired through acquisition experiments, are available and evaluated by expert physicians.

2. Overview of work plan

The complete work of preliminary texture feature functions evaluation was decomposed into seven distinct areas of work. Specifically, a set of optimally exposed mammographic images (DB1) was used as a base for the simulation, while an additional set of sub-optimally exposed mammographic phantom images (DB2) was acquired and used for independent model verification and validation purposes:

1. Acquire real mammographic images using optimal exposure settings (DB1).
2. Acquire phantom images using sub-optimal manual exposure settings (DB2).
3. Formulate a realistic exposure simulation model for constructing extensive sets of sub-optimal images from DB1.
4. Use phantom images from DB2 to validate the simulation model.
5. Construct a set of content-rich textural feature functions for image analysis, according to the current hardware and software (platform) constraints.
6. Apply complete set of textural feature functions set to both optimal and sub-optimal images, in order to evaluate performance profiles for each one of them.
7. Investigate the results and select best candidates with smooth and consistent behavior over the entire image set and exposure settings ranges (kVp, mAs).
8. Acquire a new set of X-ray images for real breast tissue samples, using sub-optimal manual exposure settings (DB3).
9. Validate the simulation model and the preliminary feature selections by investigating the texture analysis results over the new image sets (DB3).
10. Evaluate the behavior of important statistical quantities extracted from the images of a mammographic phantom in order to detect the sample edges and the presence of particular features.
11. Evaluate of the effect of some preprocessing procedures on the behavior of the same important statistical quantities.

2.1 Web-based mammographic image database (DB1)

According to the initial design specifications, various mammographic databases that are currently available in the WWW were considered. Specifically, selection was based on the core

requirements for medium or high resolution images (60µm or better), at least 8-bit grayscale depth and compact organization of both normal and abnormal (pathological) cases.

The MiniMIAS mammographic database [01] was selected as the most suitable candidate in terms of resolution, quality and overall size. The MiniMIAS is publicly available by the Mammographic Image Analysis Society (MIAS), Royal Marsden Hospital, Department of Physics, and it is used in many cases as a performance evaluation image set for various mammographic image processing and computer-aided diagnosis (CAD) systems. The base set contains 322 images of normal and abnormal cases of various pathologies, digitized at 50µm and resized to 200µm, with a final resolution of 1024x1024x8bit.

Various subsets of 20-100 images were selected in accordance to the current requirements for profile ("L" or "R") with no cropping. The selected images were cropped to the same size (500x1000x8bit) and alignment for batch processing reasons, but no pre-processing was applied for enhancement or noise-removal purposes.

2.2 Experiment documentation (RIEDS)

The final textural feature functions are to be verified when experimentally acquired image sets will be available by sensor-specific equipment. In order to provide detailed and consistent evaluation results, image acquisition experiments have to be recorded and documented thoroughly.

The RIEDS framework (Radiographic Imaging Evaluation & Documentation System) combines the needs for technical X-ray equipment description in fine detail, along with a formal set of templates for planning and logging image acquisition experiments. The main documentation templates cover the following tasks:

- Document mammographic equipment specifications
- Document experiment settings and environment
- Log experiment progress and image acquisition (samples)
- Document technical aspects of image quality for each sample
- Document clinical aspects of image quality for each sample

RIEDS was designed in accordance to standard practices and document forms that are already in clinical use for quality assessment and quality assurance procedures, as well as thorough descriptive lists of technical and clinical aspects of image quality evaluation [02-05]. Currently, the RIEDS templates for technical and clinical image quality assessment cover acquisition experiments for mammographic and dental images, which is the main target of the I-ImaS project. The same documentation organization was used as the base for an electronic version of the RIEDS system, which is to be used as a full-featured organized image database for supporting all image acquisition experiments for the I-ImaS and other similar projects.

Appendix A contains a detailed description and the full set of document templates (Forms A-F) of RIEDS. Additionally, a sample experiment planning matrix is included with exposure settings ranges coverage over kVp and mAs parameters.

2.3 Preliminary phantom image database (DB2)

As there was need for verifying the results produced by the exposure simulation model, an additional image set was constructed. Specifically, a quality-assessment mammographic phantom (Mammochip C141), containing high-resolution tissue-mimicing areas, was used as a target in an organized series of image acquisition experiments at EUROMEDICA medical center, Athens, using a typical digital mammographic system with storage phosphor arrays. The RIEDS forms were used to document the experiment and log the acquired images into specific subsets.

A limited set of 32 images was created, using manual settings for producing specific overexposure and underexposure conditions for the specific target. The exposure settings ranges applied were extended sets of the ones used in typical clinical practice for mammography, namely [25...29] kVp and [4...180] mAs. No automatic exposure control (AERC) was used in the experiments, except for specific verification and calibration cases. Absorption layers of the phantom were adjusted accordingly, in order to produce realistic exposure results for these specific settings ranges. The overall experiment planning against kVp and mAs selections in presented in Figure 1.

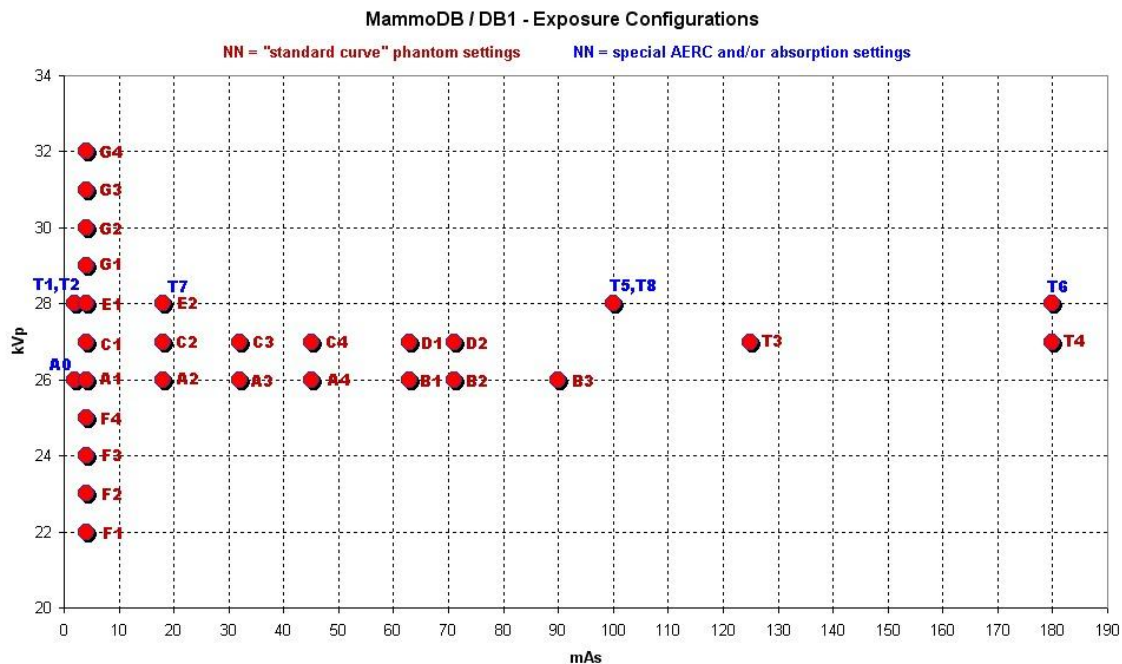


Figure 1: Experiment planning for acquired phantom images of DB2.

2.4 SimModel-1A: Exposure Simulation

A compact exposure simulation model was created in order to produce overexposed and underexposed conditions from a limited set of optimal images. The main task was to formulate a fully adjustable virtual exposure system that could effectively transpose an image of given initial exposure conditions to another arbitrary set of exposure conditions.

In accordance to the general specifications of the overall procedure of evaluating the efficiency of various textural features functions under varying exposure conditions, an initial set of 20 base images were used to produce 21 simulated exposures for each one of them, thus producing a total set of 420 images of excessive, reduced and optimal exposure. This combined set constituted the base of further processing in subsequent feature functions performance evaluation.

2.4.1 Model Design Parameters

The simulation model (SimModel-1A) was decomposed into four basic exposure attributes that subsequently correlate with each other to produce the final X-ray image. Specifically, these parameters relate to the intermediate stages of translating the X-ray exposure radiation level (Rx) into standard optical density level (OD), then into gray value at the sensor (GL) and finally into the graylevel pixel value of the digital image (GI):

1. *Rx : Radiation Exposure Level (dose)*
2. *OD : Optical Density of X-ray projected subject*
3. *GL : Gray Value of (digital) sensors*
4. *GI : Graylevel of pixels in the resulting image*

The implementation of SimModel-1A was based on reference sheets and typical performance charts of digital mammographic equipment [06-12]. All four parameters were combined into a four-stage (F1-F4), bi-directional, processing pipeline, using equation modeling and interpolation within the operational ranges for each one of them.

Input parameters, namely kVp and mAs, were limited within typical operational ranges for mammography, at [25...29] and [50...200] accordingly. All inherent model parameters were scaled accordingly in order to provide a fixed set of operational ranges for each one of them. Specifically, radiation exposure levels were modeled for mGy values between: [0,0...4,0]. However, the validity of the model is based on the transfer function given specific kVp and mAs input settings, whereas mGy extremes are used merely to scale the transfer function F1 within the required range.

F1:

kVp: [25...29] , mAs: [50...200]

Rx : [0,0128...4,000] mGy

$$Rx : f_1(kVp, mAs) = C_{1,1} \cdot \log_{10}\{(kVp)^2 \cdot (mAs)\} + C_{1,0}$$

$$C_{1,0} = -0,897021103$$

$$C_{1,1} = 0,000029114$$

Table 1: SimModel-1A, stage-F1: Radiation Exposure Level function (model).

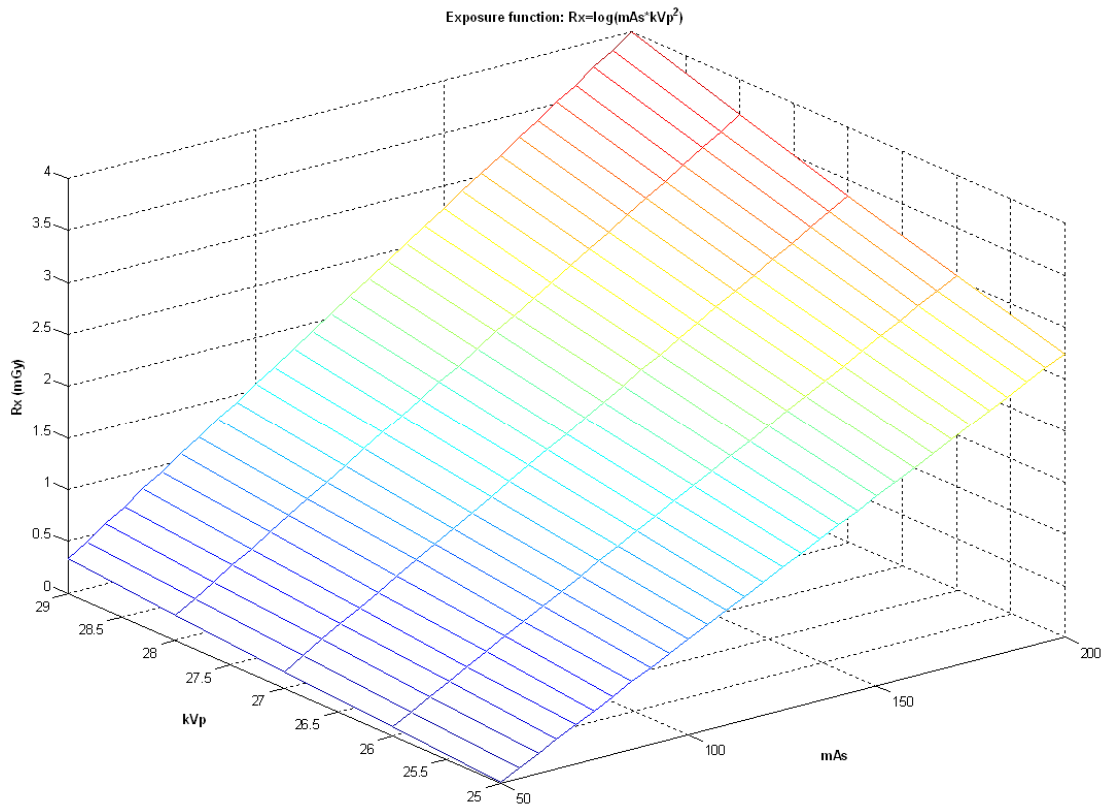


Figure 2: SimModel-1A, stage-F1: Radiation Exposure Level function (plot).

The same approach was applied to the next level of processing, i.e. converting radiation exposure level to optical density (OD). Although optical density is typically used to characterize attributes of analogue imaging systems that use conventional films (instead of direct digital conversion), it was necessary to introduce this intermediate stage in order to adapt the simulation model to verified performance charts that correlate optical density measurements to typical digital sensor values [06-07,09-10]. Using these intermediate results, it was possible to verify the logarithmic correlation between radiation exposure (dose) and optical density in analogue films, thus suggesting the implementation of the F2 stage as a simple logarithmic function. Extreme values are, again, adjusted accordingly in order for the F2 function to produce results within standard optical density values, namely: [0,04...3,60].

F2:

Rx : [0,0128...4,000] mGy

OD: [0,04...3,60]

$$OD: f_2(Rx) = C_{2,1} \cdot \log_{10}(Rx) + C_{2,0}$$

$$C_{2,0} = 2,740896827$$

$$C_{2,1} = 1,426939483$$

Table 2: SimModel-1A, stage-F2: Optical Density function (model).

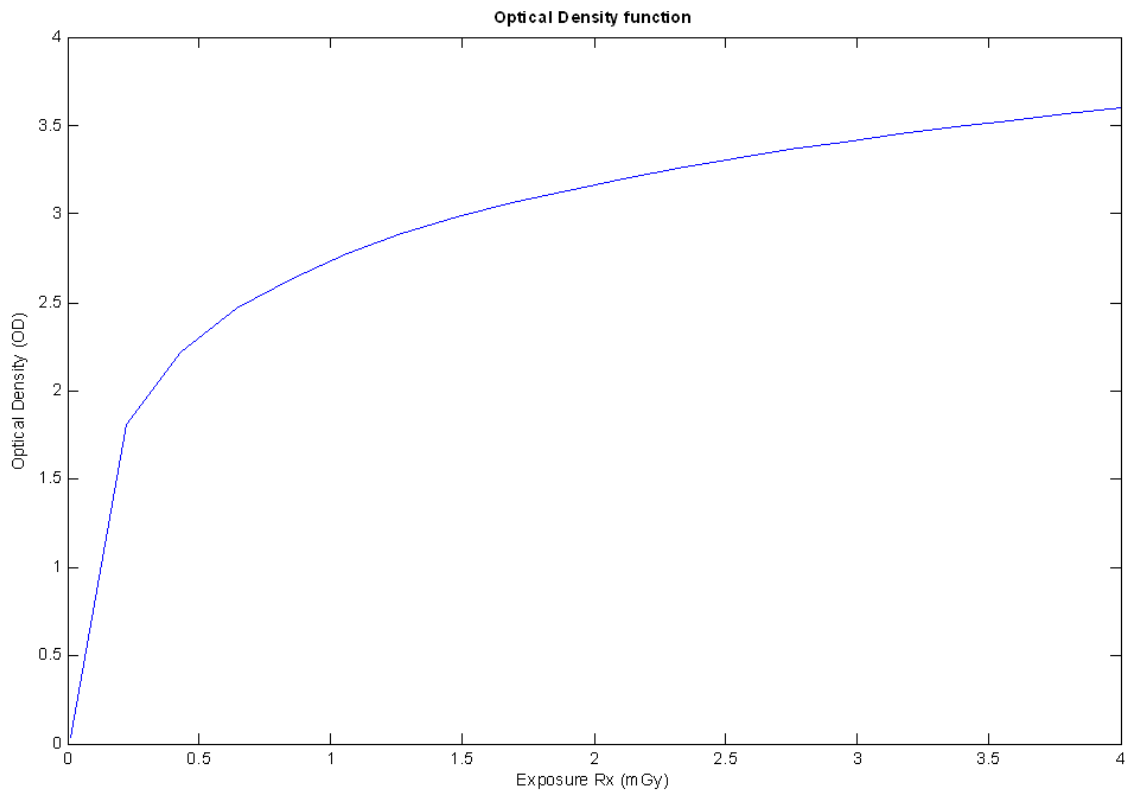


Figure 3: SimModel-1A, stage-F2: Optical Density function (plot).

The conversion of optical density into gray values of digital sensors (GL) was investigated in comparative reference sheets of typical digital mammographic equipment. Correlation between analogue and digital imaging pixel values was confirmed to closely follow linear translation mapping for the largest portion of operational ranges, thus the F3 processing stage was implemented as a simple linear transfer function. Extreme gray values for typical 12-bit digital sensors were established at: [495...4069], in accordance to the extreme values of the optical density values at the previous stage.

F3:

OD: [0,04 ...3,60]

GL: [495 ...4069]

$$GL: f_3(OD) = (OD - C_{3,0}) \cdot \frac{1}{C_{3,1}}$$

$$C_{3,0} = 4,093060996$$

$$C_{3,1} = -0,000996083$$

Table 3: SimModel-1A, stage-F3: Sensor Gray Value function (model).

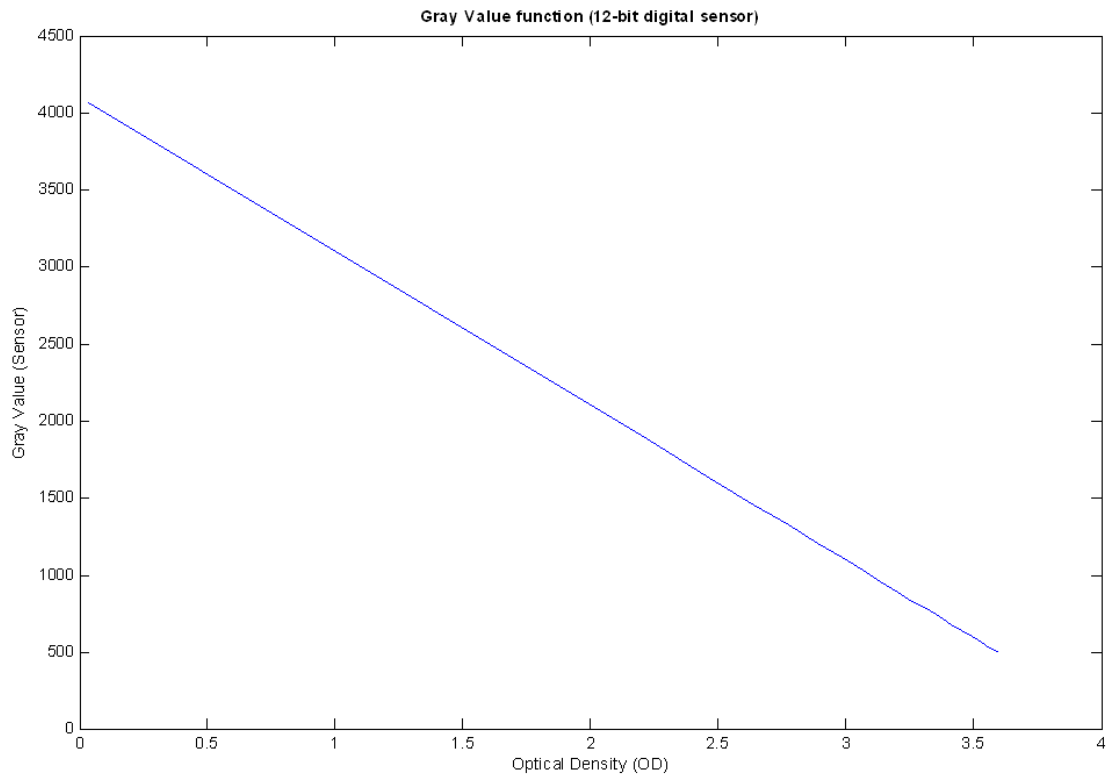


Figure 4: SimModel-1A, stage-F3: Sensor Gray Value function (plot).

Finally, the digital image creation stage was the simple translation of the gray values from the digital sensors into pixel graylevel values (GI), using a linear mapping function. As the sensor values are translated into pixel values at full range, only a simple conversion from 12-bit down to 8-bit was necessary, thus producing a standard grayscale of [0...255].

F4:

GL: [4095 ...0]

GI: [0 ...255]

$$GI : F_4(GL) = C_{4,1} \cdot (GL) + C_{4,0}$$

$$C_{4,0} = 255$$

$$C_{4,1} = -0,062271062$$

Table 4: SimModel-1A, stage-F4: Pixel Graylevel function (model).

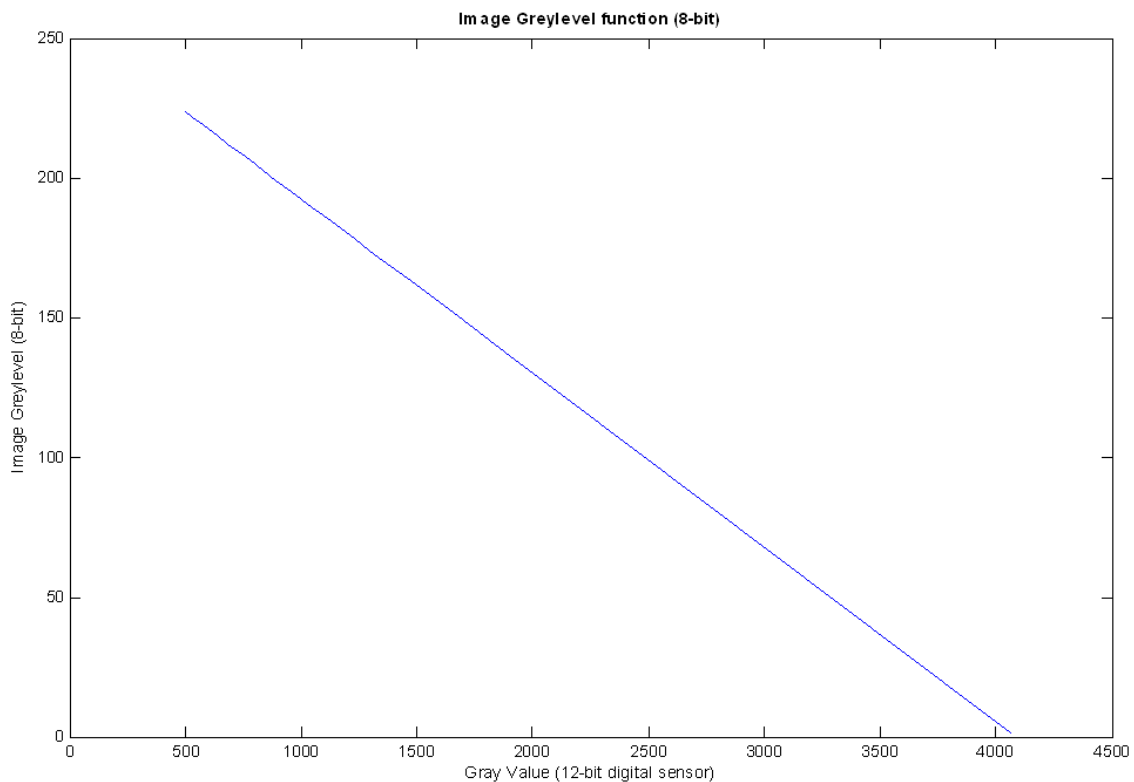


Figure 5: SimModel-1A, stage-F4: Pixel Graylevel function (plot).

It should be noted that, as optical density (OD) essentially measures the “darkness” of the projected image on the analogue film, high gray values (GL) at the sensor are translated into dark pixel values, i.e. low graylevel values (GI). For reasons of clarity and better understanding of the simulation model, the scale inversion of the sensor values were introduced, not between stages F3 and F4 (GL to GI), but rather earlier between stages F2 and F3 (OD to GL), in order to end up with resembling linear forms for both GL and GI. As all processing after stage F2 is essentially based on linear transformations, this adaptation does not affect the functionality of the overall simulation model.

2.4.2 Model Overview

The four-stage (F1-F4) processing pipeline of SimModel-1A is the base framework for translating radiation exposure levels into pixel values in the final (digital) image. However, since the input consists only of the initial image of optimal exposure, there are no detailed content information about the structure and the absorption levels of the real projected target, i.e. tissue properties. Thus, in order to acquire a reference level for the new radiation exposure, a good estimation of the exposure settings (kVp, mAs) has to be made for every optimally exposed image that is used as an input for the simulation.

For the specific set of the 20 initial mammographic images, a reference point was established at 27 kVp and 125 mAs, which is a standard exposure profile in clinical mammography both for analogue and digital mammographic equipment. Although there is some deviation between these typical values and the true exposure settings of images within the initial image set, the real value of the simulation is to investigate the transition of the textural characteristics of the image content in relation to the associated transition of the exposure settings (kVp, mAs), rather than to create a very accurate final image through simulated exposure. Therefore, it is safe to say that, given the comprehensive modular structure of the simulation model and a valid set of operational ranges for all the parameters involved, a good estimation of textural feature functions performance against exposure settings can be conducted.

In order to exploit the information content of the initial (input) image with regard to the real structure and radiation absorption of the projected target, the reference level of the initial radiation exposure is used to estimate the required transition of Rx from its starting value. Adjusting any one, or both, kVp and mAs exposure settings, results in a new value for the exposure level Rx, according to the model function F1. Given the initial (input) image and the initial exposure level, the new (simulated) image can be reconstructed in pixel-by-pixel using the initial pixel value and the required exposure adjustment. Although the new exposure level is the same for the entire reconstructed image, the same simulation model is used in reverse mode to translate initial pixel values into raw radiation value, adjust to the new exposure level, and then back to a new pixel value again.

It should be noted that this procedure is completely different from adjusting the input image directly to new pixel values, applying some form of graylevel histogram transformation (windowing, equalization, gamma correction, etc). As the basic control parameters for the final system are the exposure settings of kVp and mAs, any pixel-based transformation that does not involve the first processing stage (F1) of the simulation model cannot be used to investigate direct statistical correlation between variations of exposure settings (kVp, mAs) against performance of textural feature functions on the final (altered) image. Model inversion is necessary only for processing stages F2 to F4, as F1 functionality is the same for both the initial and the new image. Table 5 summarizes the complete SimModel-1A, including the inverse functions for GI, GL and OD, and Table 6 describes the detailed simulation procedure.

MODEL:

$$\{image_0[x, y]\} \longrightarrow [Rx] \xrightarrow{f^2} [OD] \xrightarrow{f^3} [GL] \xrightarrow{f^4} [GI] \longrightarrow \{image_1[x, y]\}$$

$$\left. \begin{array}{l} \{kVp(0), mAs(0)\} \xrightarrow{f^1} [Rx(0)] \\ \{kVp(z), mAs(z)\} \xrightarrow{f^1} [Rx(z)] \end{array} \right\} \Rightarrow r = \frac{Rx(0)}{Rx(z)}$$

Inverse Model Functions:

$$GL: f_4^{-1}(GI) = (GI - C_{4,0}) \cdot \frac{1}{C_{4,1}}$$

$$OD: f_3^{-1}(GL) = C_{3,1} \cdot OD + C_{3,0}$$

$$Rx: f_2^{-1}(OD) = 10^{\frac{OD - C_{2,0}}{C_{2,1}}}$$

Table 5: SimModel-1A, overview of reconstruction procedure and inverse model functions

FULL SIMULATION PROCEDURE:

1. $Input : \{kVp(0), mAs(0)\}, \{image(0)_{x,y}\}, \{kVp(z), mAs(z)\}$
2.
$$\left. \begin{array}{l} \{kVp(0), mAs(0)\} \xrightarrow{f_1} [Rx(0)] \\ \{kVp(z), mAs(z)\} \xrightarrow{f_1} [Rx(z)] \end{array} \right\} \Rightarrow r = \frac{Rx(z)}{Rx(0)}$$
3.
$$\{image(0)_{x,y}\} \longrightarrow GI(0)_{x,y} \xrightarrow{f_4^{-1}} GL(0)_{x,y} \xrightarrow{f_3^{-1}} OD(0)_{x,y} \xrightarrow{f_2^{-1}} Rx(0)_{x,y}$$
4.
$$Rx(z)_{x,y} = \frac{Rx(0)_{x,y}}{r}$$
5.
$$Rx(z)_{x,y} \xrightarrow{f_2} GL(z)_{x,y} \xrightarrow{f_3} GI(z)_{x,y} \longrightarrow \{image(z)_{x,y}\}$$
6. $Output : \{image(z)_{x,y}\}$

Table 6: SimModel-1A, complete exposure simulation procedure. Calculation of the exposure adjustment parameter (r) is consistent with the expected visual results of overexposure and underexposure conditions, i.e. brighter darker images, accordingly.

2.4.3 Results and Verification

The results from the final SimModel-1A were investigated through comparative studies of simulated mammographic images of sub-optimal exposure with real phantom images acquired at similar exposure conditions, and verified by an expert radiologist. The apparent visual differences between simulated versions of the same image at different exposure settings were evaluated as realistic and consistent with the expected results. Simulated images at fixed exposure settings closely matched the visual result of real phantom images at proportionally analogous radiation absorption conditions, i.e. roughly the same kVp settings at adjusted mAs rates, appropriate to physical differences between real breast and phantom. Figures 6 and 7 display examples of simulated (mammographic) and real (phantom) images.

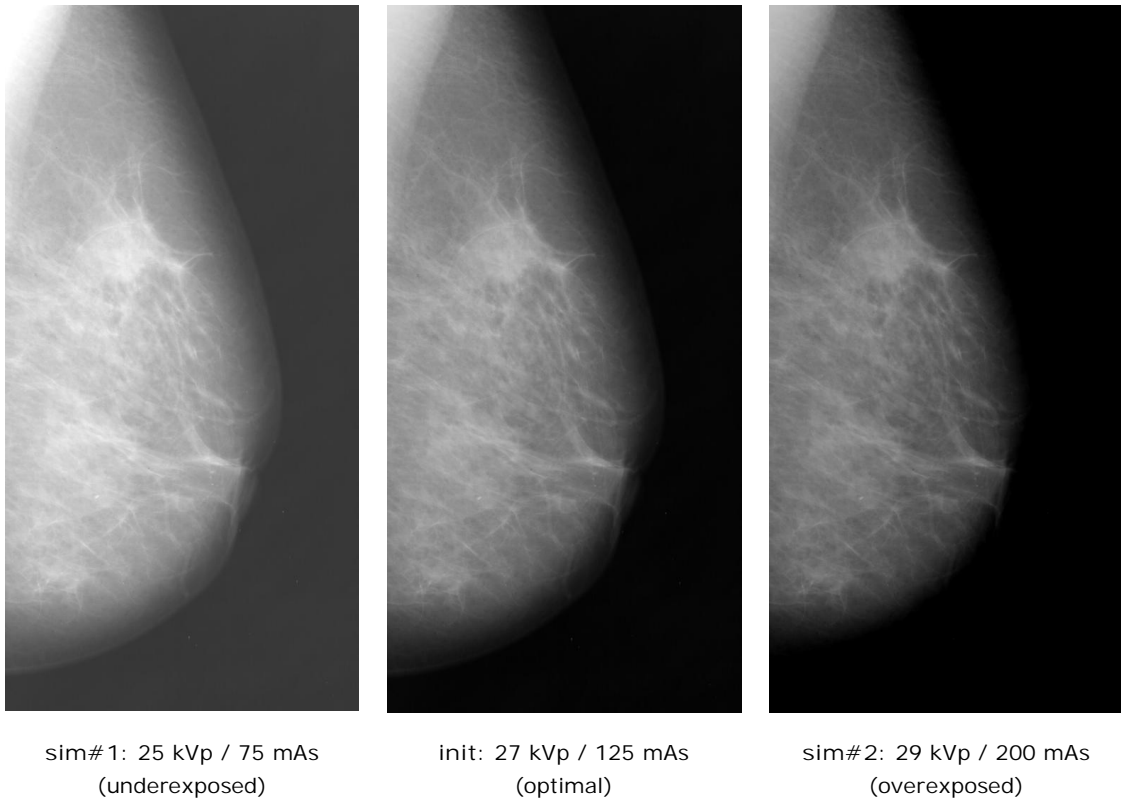


Figure 6: SimModel-1A, sample simulated mammographic images (DB1).

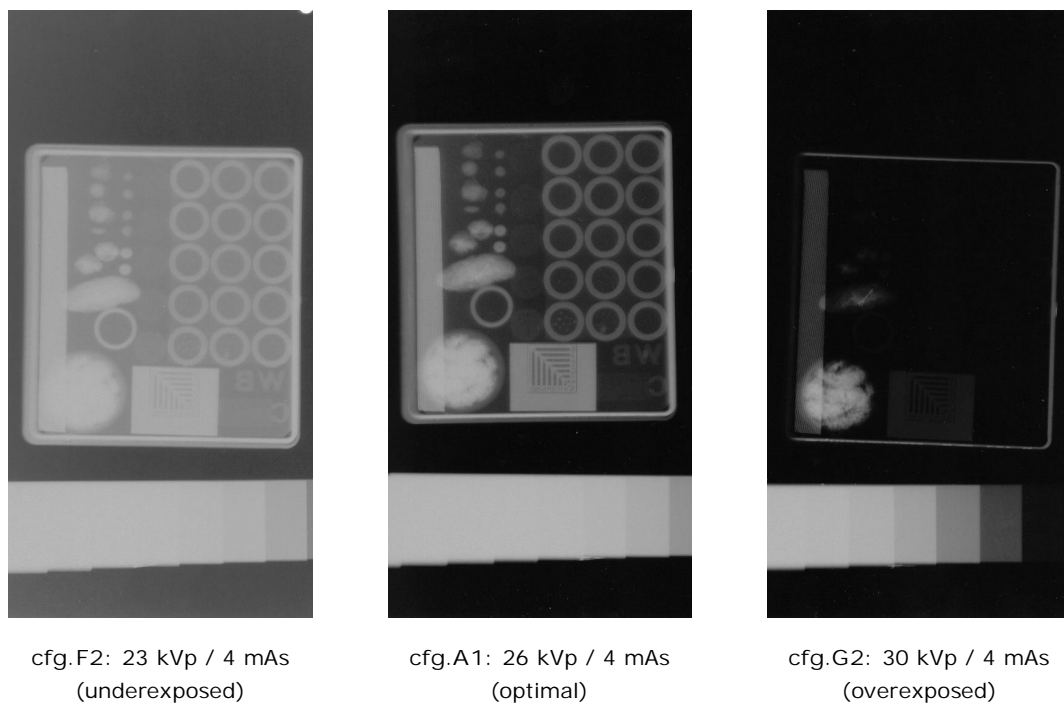


Figure 7: Samples of real sub-optimally exposed phantom images (DB2).

2.5 PredModel-1A: Textural Features Extraction

A comprehensive set of textural feature functions was created in order to investigate the best candidates for fast image analysis and quality assessment during the line-scanning procedure. All feature functions had to be well-suited for mammographic and dental image analysis, with inherent low computational complexity and stable performance.

As the target platform specifications demanded very limited resource availability and time constraints were very strict, image analysis had to be limited to local processing, in order to avoid excessive data transfers, and simple functionality based on 1st order graylevel statistics, in order to avoid excessive calculation times.

2.5.1 Model Design Specifications – Progressive Image Scanning

In accordance to the general design of the line-scanning and sensor system, all image analysis had to be limited to “columns” of buffered pixel data of complete image height and fixed width. The use of multiple autonomous IC modules introduces the capability of trully parallel data processing at segments of any arbitrary “column” of currently available image data, as long as the feature functions depend solely on local input of a limited image area and their implementation is simple enough to integrate within the IC of each sensor, instead of transferring the data elsewhere for some sort of centralized processing.

Furthermore, each feature function had to be able to produce a single characteristic value for every local image sample, i.e. a simple 1-D curve for every “column” of buffered pixel data. This way, the line-scanning procedure would create a reduced 2-D mesh of characteristic texture values that can be used effectively and efficiently and a content-rich “signature” of the underlying image data.

As the textural data had to be investigated against the exposure settings (kVp, mAs), further dimensionality reduction is required. Specifically, instead of creating a full 2-D mesh of textural data, all values acquired for a specific “column” of buffered pixel data are averaged, essentially producing a single combined data component, instead of a data vector (1-D curve). In the final implementation, the combined data component contains two descriptive statistical values, namely the mean and standard deviation of all feature values calculated for the current image “column”. This way, the overall result of applying a textural feature function during the line-scanning procedure is two simple 1-D curves of column-wise averaged local feature values, one for mean and one for standard deviation. Figure 8 depicts the actual procedure of calculating localized texture feature functions during the line-scanning procedure.

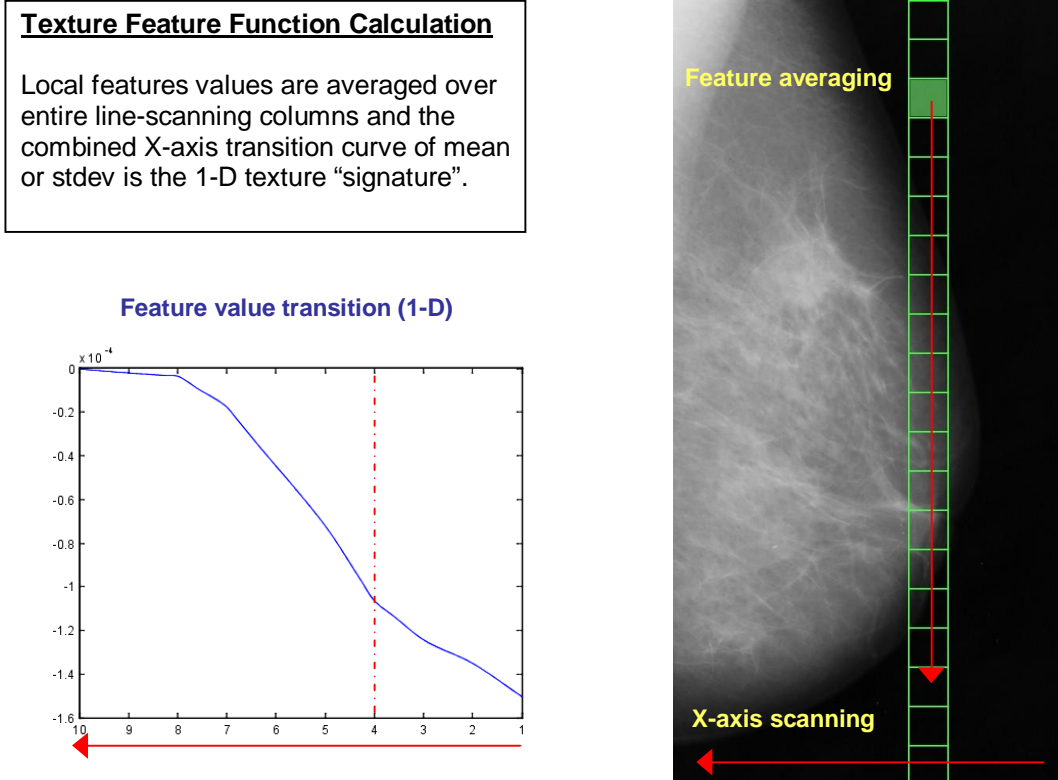


Figure 8: Texture feature function calculation during the line-scanning procedure.

2.5.2 Textural Feature Functions

All feature functions were selected according to their suitability for texture analysis on mammographic and dental images, as well as their low complexity in terms of storage requirements and processing time.

An initial set of 6 standard 1st order statistical functions were used as the base for typical measurements like minimum value, maximum value, mean value, etc. An additional set 5 of signal power, entropy and surface “roughness” estimators were also used in some simple form of implementation, using only raw pixel data values from the local image area, i.e. no spectrum analysis was involved in these cases [11-17].

The initial set of 11 statistical feature functions was extended by creating another 9 synthetic estimators, using normalized versions of the previous ones, combining the results of two or more simple features, or extending the functionality of the “roughness” estimators to a more generalized form in order to produce unbiased results. The last 5 of the 9 synthetic feature functions can be considered as a very simplistic approximation of techniques and algorithms, normally used to extend the notion of image “roughness” to more general structural analysis approaches like calculating the fractal dimension of an image area. Although their results do not coincide with fractal analysis of the image data, they inherit similar capability in capturing a fairly descriptive indication of the complexity of the underlying image, usually available only when using 2nd or higher order statistics.

Table 7 contains all 20 textural feature functions that were implemented in PredModel-1A. Appendix B contains sample implementation source code (Matlab).

Texture Feature Function (Name)	Mathematical Formula
1. Min value	$I_{\min} = \min_{XY} \{I(x, y)\}$
2. Max value	$I_{\max} = \max_{XY} \{I(x, y)\}$
3. Mean value	$\mu = \frac{1}{XY} \sum_{i=1}^X \sum_{j=1}^Y I(x, y)$
4. Std.Deviation	$\sigma = \sqrt{\frac{1}{(XY-1)} \sum_{i=1}^X \sum_{j=1}^Y (I(x, y) - \mu)^2}$
5. Skewness	$sk = \frac{1}{XY} \sum_{i=1}^X \sum_{j=1}^Y \left(\frac{I(x, y) - \mu}{\sigma} \right)^3$
6. Kurtosis	$kr = \left(\frac{1}{XY} \sum_{i=1}^X \sum_{j=1}^Y \left(\frac{I(x, y) - \mu}{\sigma} \right)^4 \right) - 3$
7. Signal Power	$P_{XY} = \sum_{i=1}^X \sum_{j=1}^Y \ I(x, y)\ ^2$
8. Entropy	$E = \sum_{k=1}^{100} P_{Ghist(k)} \cdot \log(P_{Ghist(k)})$
9. Zero-Crossings	$ZC = \sum \{k : (I_k(x, y) - \mu) \cdot (I_{k+1}(x, y) - \mu) \leq 0\}$
10. Surface	$S_{XY} = \sum_{i=1}^{X-1} \sum_{j=1}^{Y-1} (I(x, y) + 1 + \ I(x+1, y) - I(x, y)\ + \ I(x, y+1) - I(x, y)\)$
11. Volume	$V_{XY} = \sum_{i=1}^X \sum_{j=1}^Y I(x, y)$
12. Synth.Feat-12	$SF_{12} = \frac{(I_{\max} - I_{\min})^2}{\mu}$
13. Synth.Feat-13	$SF_{13} = \frac{\mu - I_{\min}}{I_{\max} - I_{\min}}$
14. Synth.Feat-14	$SF_{14} = \frac{\mu}{\sigma}$

15. Synth.Feat-15	$SF_{15} = \frac{P_{XY}}{\mu^2}$
16. Synth.Feat-16	$SF_{16} = \frac{\sqrt{S_{XY}}}{\sqrt[3]{V_{XY}}}$
17. Synth.Feat-17	$SF_{17} = \frac{S_{XY}}{XY}$
18. Synth.Feat-18	$SF_{18} = \frac{ZC}{XY}$
19. Synth.Feat-19	$SF_{19} = \frac{P_{XY}}{XY}$
20. Synth.Feat-20	$SF_{20} = \log\left(1 - \frac{SF_{19}}{255^2}\right)$

Table 7: PredModel-1A, texture feature functions and mathematical formulas.

2.5.3 Intermediate 2-D Texture Matrices

In order to assess the effectiveness and robustness of the various texture feature functions, it was necessary to visually evaluate the 2-D output of each function before the individual texture values are averaged throughout the entire column. The intermediate result is a 2-D mesh of single texture values that are calculated for each local image area.

The general line-scanning and sensor system design permits some degree of flexibility with regard to the exact size of the local image sample that is to be used as input for the texture feature functions. Thus, it was necessary to investigate the effects of using image samples of various sizes in relation to the efficiency and stability of the functions, especially in the extreme cases of using very small or very large sampling boxes. While small samples permit very fast image processing, the information content that is captured by each individual texture value is limited and the resulting data flow becomes excessive for the subsequent processing stages. On the other hand, large sampling boxes produce structural details at large scales, but they can create a performance bottleneck at the image processing modules due to excessive calculations.

PredModel-1A was applied with three distinct sampling configurations, namely at (square) box sizes of 10, 25 and 50 pixels wide. All 1st order and synthetic feature functions employ computational complexity proportionally analogous to the total number of pixels contained in the input sample, i.e. $O(N^2)$ where N is the width of the (square) sampling box. This means that a sampling square box of 50 pixels contains 25 times larger input data volume than in the case of a 10 pixel box. Analytical study on the issue of sampling box sizes was conducted

subsequently with PredModel-1B, in combination with the overall task of evaluating feature functions performance against exposure settings (kVp, mAs).

Figures 9 through 16 present the intermediate 2-D texture value results against different exposure settings, using a fixed set of simulated exposure mammographic images. As it is described in detail subsequently in the section for PredModel-1B, the 7 feature functions that are presented in these figures actually constitute the best candidates for capturing the textural information content of the underlying image. All 2-D texture matrices were constructed using sampling box size of 10 pixels, in order to produce visual results of the best possible resolution (larger 2-D mesh sizes).

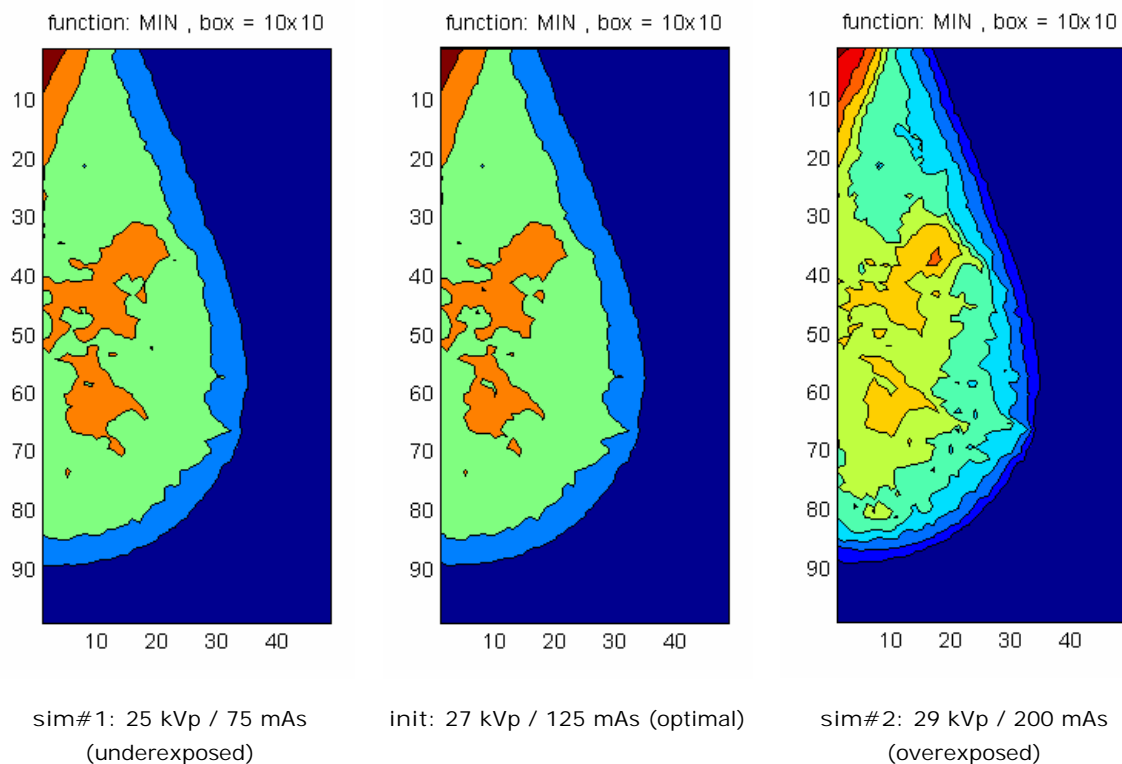


Figure 9: PredModel-1A, intermediate 2-D texture results for MIN feature function at different exposure settings.

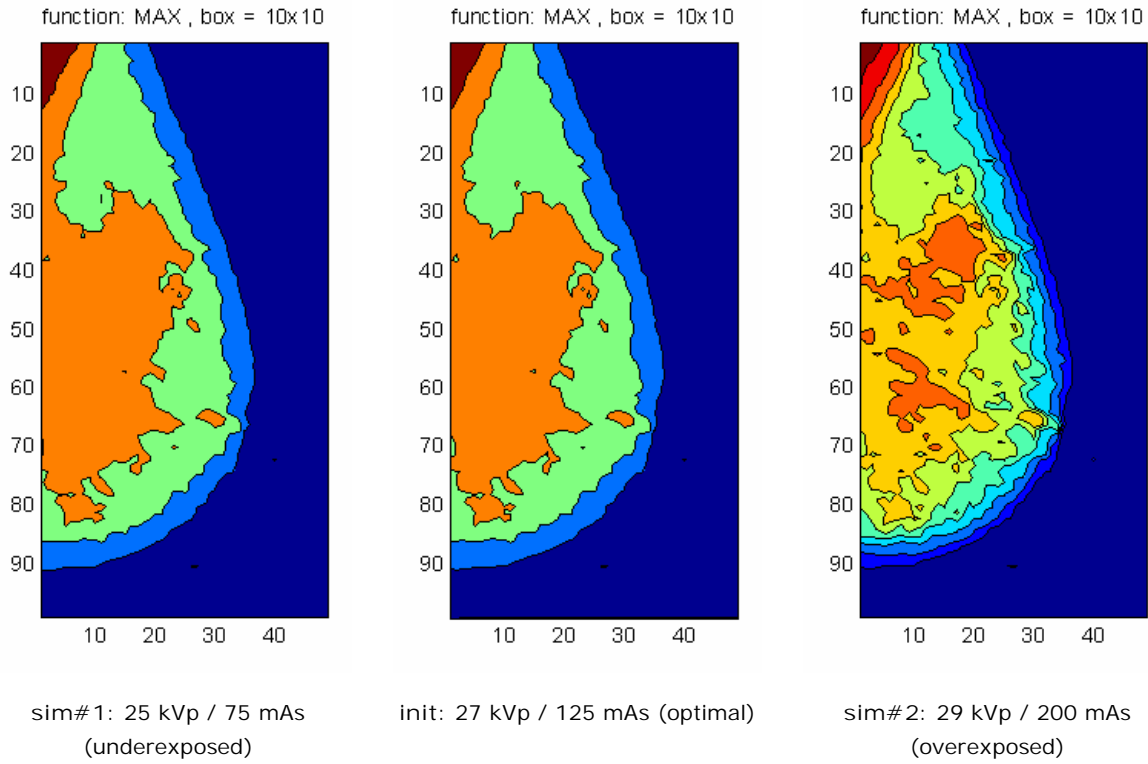


Figure 10: PredModel-1A, intermediate 2-D texture results for MAX feature function at different exposure settings.

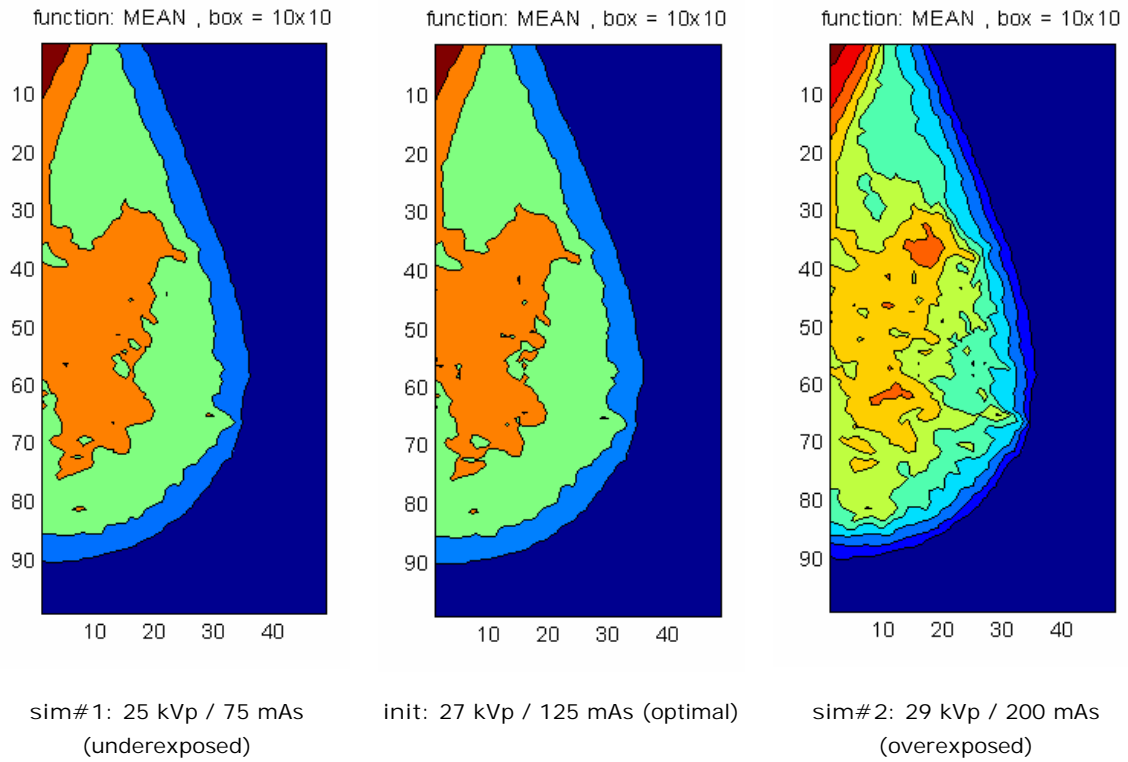


Figure 11: PredModel-1A, intermediate 2-D texture results for MEAN feature function at different exposure settings.

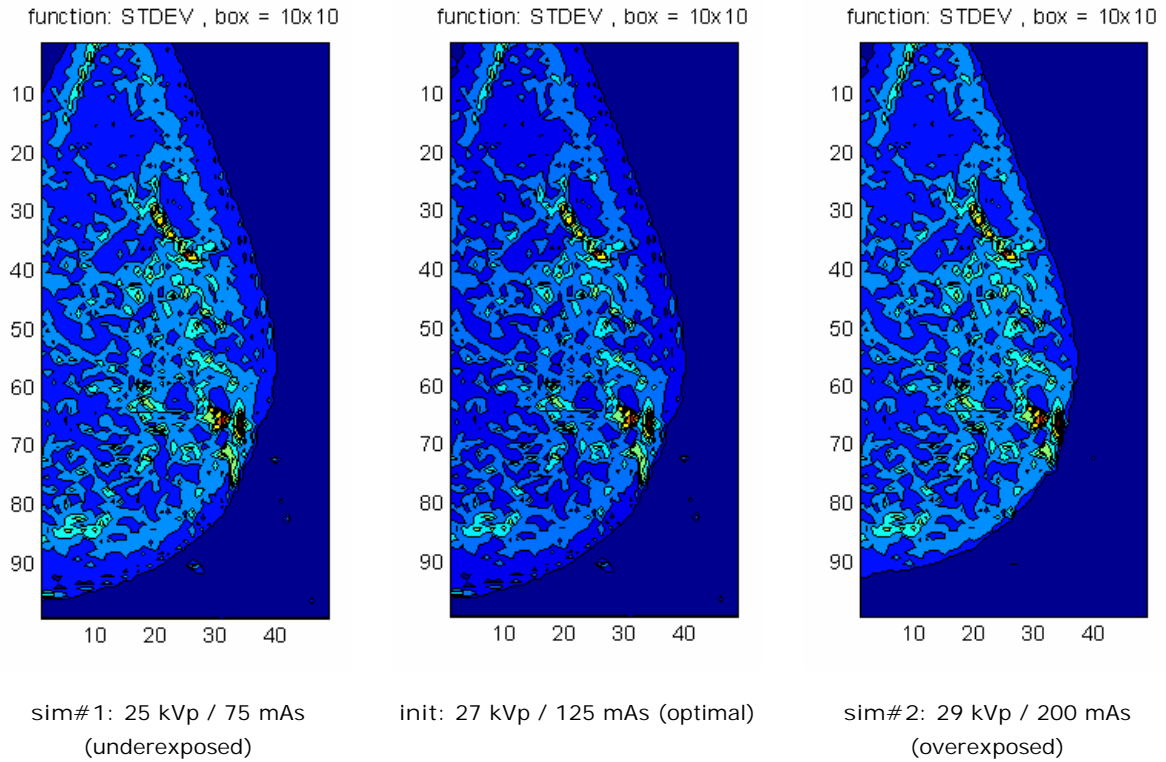


Figure 12: PredModel-1A, intermediate 2-D texture results for STDEV feature function at different exposure settings.

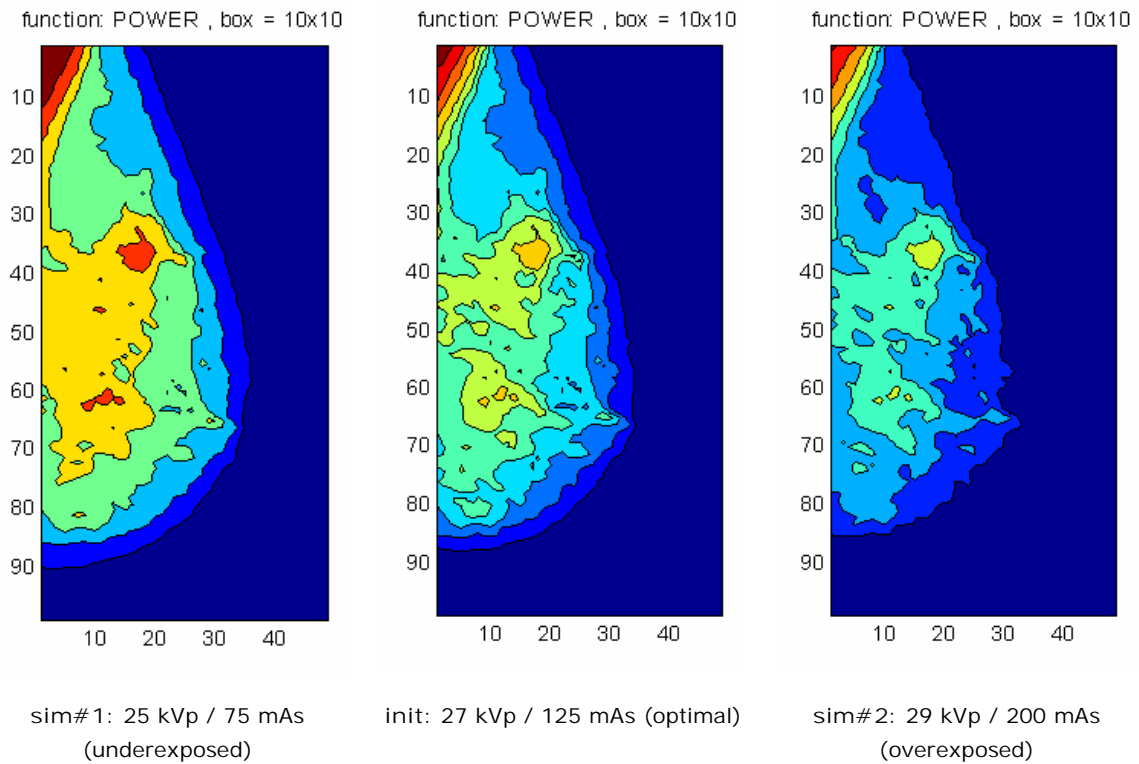


Figure 13: PredModel-1A, intermediate 2-D texture results for POWER feature function at different exposure settings.

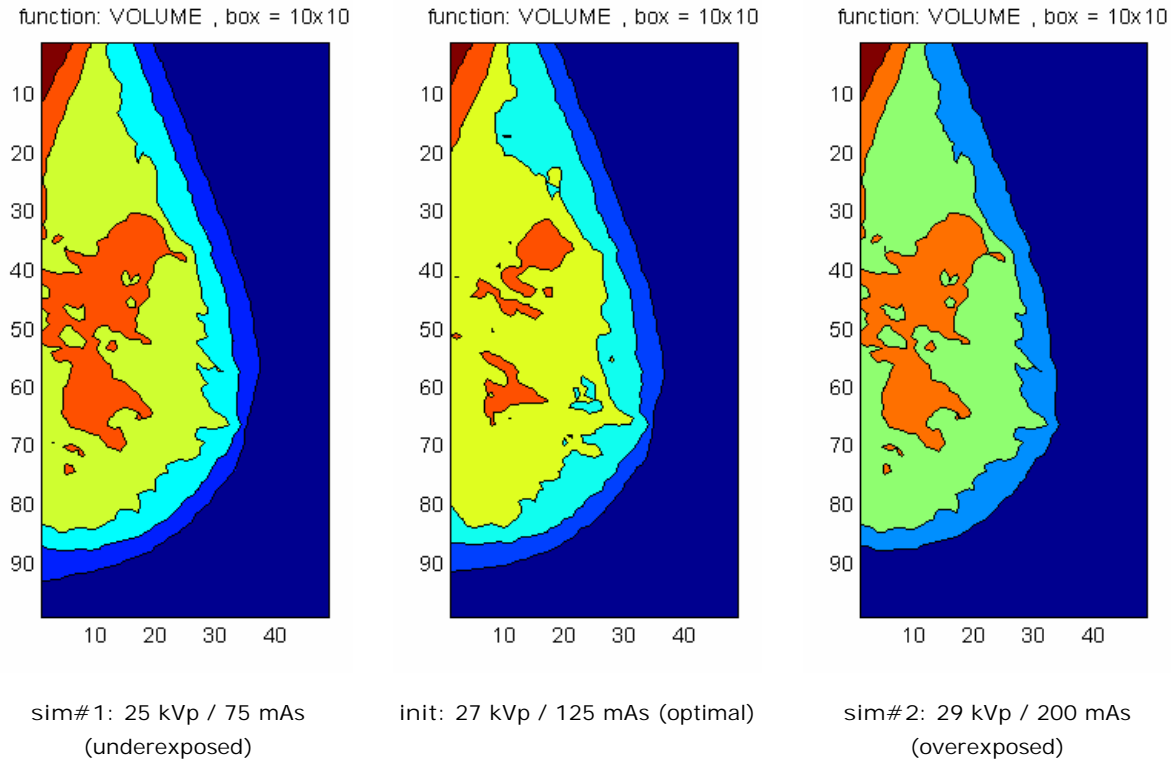


Figure 14: PredModel-1A, intermediate 2-D texture results for VOLUME feature function at different exposure settings.

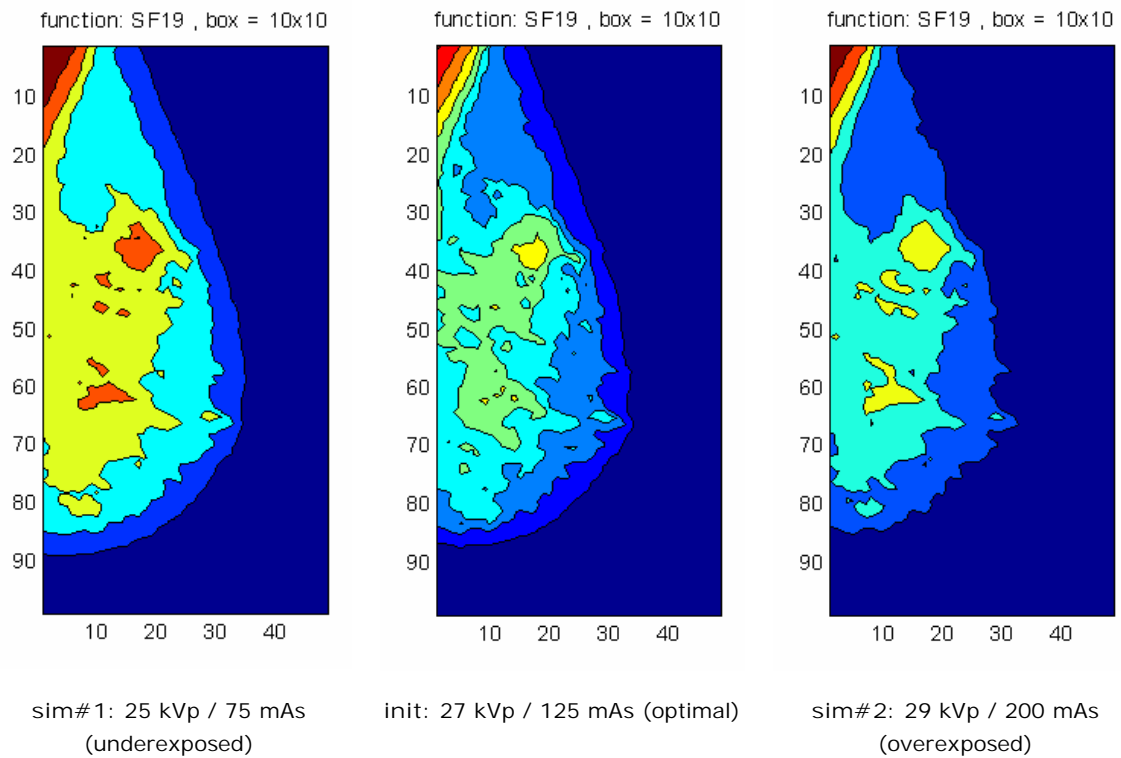


Figure 15: PredModel-1A, intermediate 2-D texture results for SF19 feature function at different exposure settings.

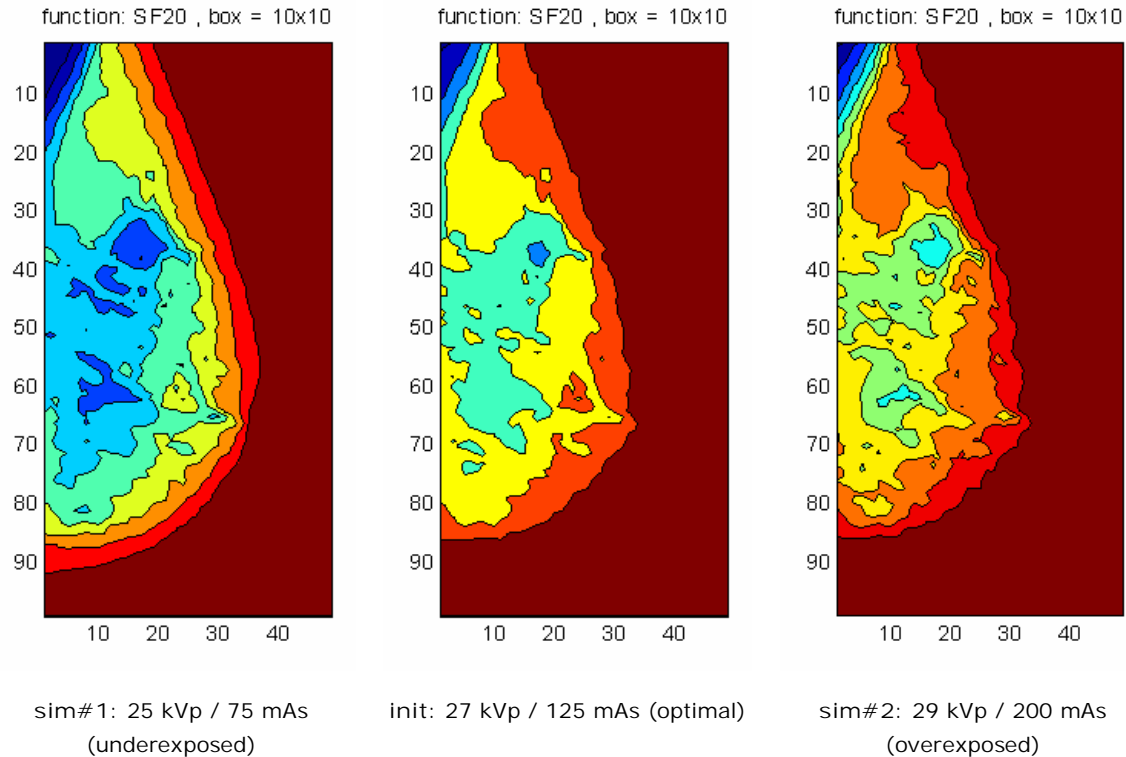


Figure 16: PredModel-1A, intermediate 2-D texture results for SF20 feature function at different exposure settings.

Although these intermediate 2-D texture results have to be reduced into 1-D data before they can be used as feedback for the exposure control system, it is clearly evident that these simple feature functions capture a great amount of significant content information. All functions a great level of discrimination capability between the background and the tissue areas, whereas some of them perform equally well in distinguishing the internal tissue structural details equally well.

The STDEV function seems to be very effective in recognizing tissue areas with no significant sensitivity to the actual exposure levels, but at the same time there is little gain in using it as feedback for the exposure control system. The MIN, MAX and MEAN functions perform very well at high exposure levels, but their discriminative content changes little to none in medium to low exposure levels. The POWER, VOLUME, SF19 and SF20 functions perform very well at low exposure levels and have the best discriminative behavior at various exposure ranges, but seem to loose their capability of tracking closely onto the tissue boundaries.

As the PredModel-1B results confirm, no one function is adequate of tracking both the information content of image texture and changes in the exposure level. Therefore, it is most probable that more than one of these candidate functions will be used in combination as the final feedback for the sensor intelligent control.

2.6 PredModel-1B: Textural Features Evaluation

Using the overall framework and results from PredModel-1A, the final phase of the analysis consisted of the evaluation of textural feature functions performance against changes in the exposure settings (kVp, mAs). This step is necessary in order to identify the best candidate functions that, not only capture significant information content from the image at minimal cost, but at the same time provide a solid “description” of the input parameter space throughout the entire range of exposure levels.

2.6.1 Texture “signatures” against exposure rates

Standard clinical practices and regulations impose strict regulations on maximum patient dose during an X-ray examination and as a result there are specific upper bounds to the exposure levels that the sensor control would permit. Furthermore, it is necessary to adopt a design that permits constant image quality at minimal dose for the patient. Therefore, it is necessary to provide a well-defined functional relation between textural feature values that could be used as feedback for the controller and the main exposure parameters, namely kVp and mAs. This means that any candidate textural feature function has to provide smooth, consistent and stable transfer hyperplane in both dimensions, similar to the actual radiation exposure function that is used in SimModel-1A for Rx.

In PredModel-1B, all 2-D intermediate results from textural feature functions were reduced into 1-D transfer functions in accordance to the line-scanning direction (conventionally, from nipple to chest). Furthermore, texture data were grouped according to their location, i.e. the same image “column”, and the radiation exposure level (Rx). The resulting 3-D plot represents the way a complete set of image “columns” is translated into a 1-D “signature” at various exposure rates.

Figures 17 through 36 demonstrate the performance of the complete set of 20 feature functions, including the 8 candidates that were investigated thoroughly at the previous section. All plots were constructed using a sampling box size of 10 pixels in order to produce better resolution for the resulting matrices. The X-axis represents the X-axis of the image, i.e. the actual line-scanning direction. The overall exposure level, calculated by the same Rx function (F1) that was used in the SimModel-1A implementation, is presented in the Z-axis. Finally, the Y-axis shows the specific feature function values in relation to both the scanning direction and the exposure level. Each plot essentially captures the transition of the “signature” that the specific feature function creates for the same image, throughout various exposure settings.

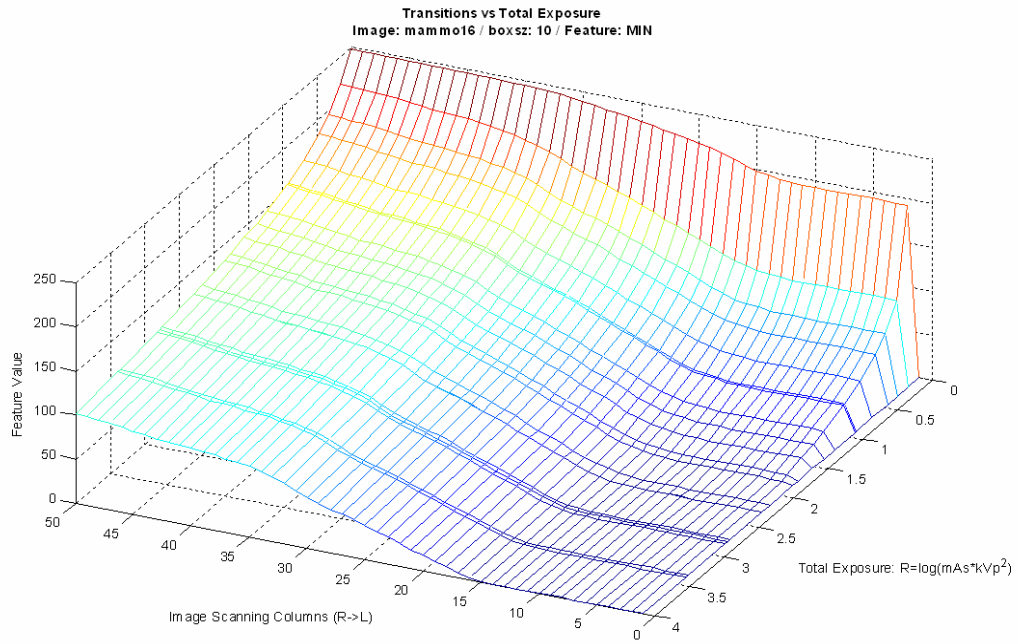


Figure 17: PredModel-1B, textural “signature” profile for MIN feature function at different exposure settings.

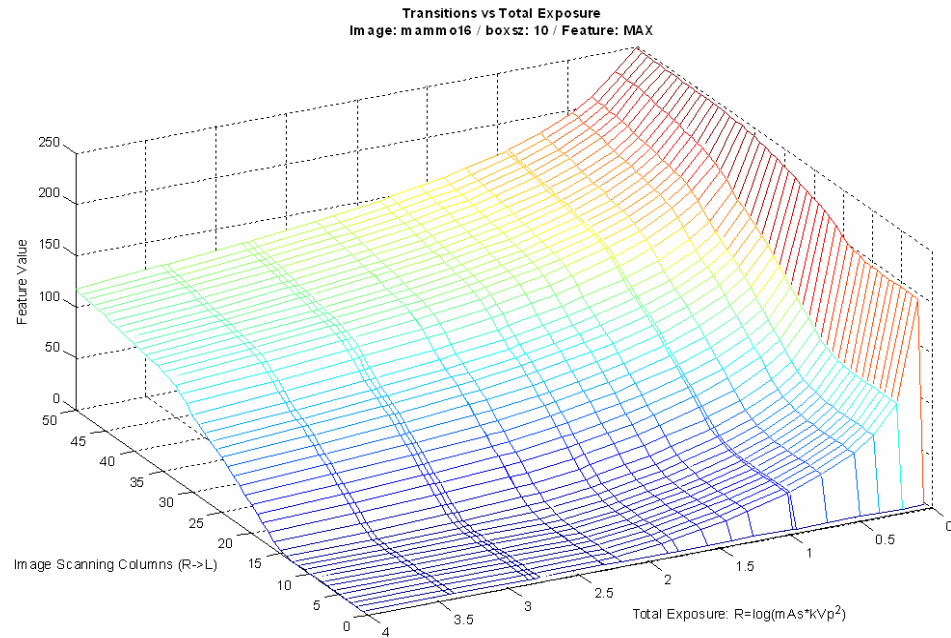


Figure 18: PredModel-1B, textural “signature” profile for MAX feature function at different exposure settings.

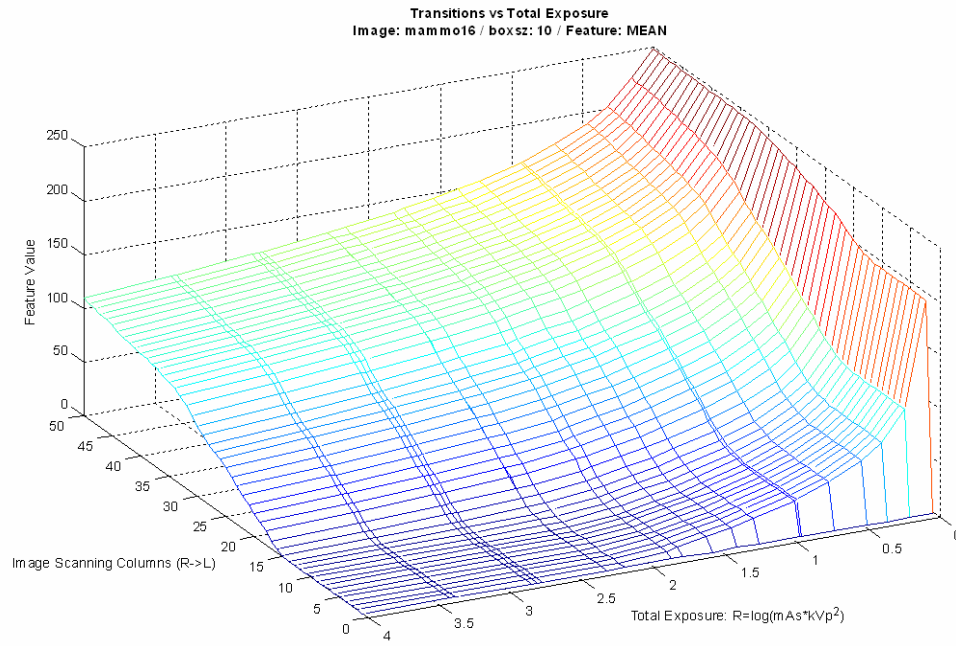


Figure 19: PredModel-1B, textural “signature” profile for MEAN feature function at different exposure settings.

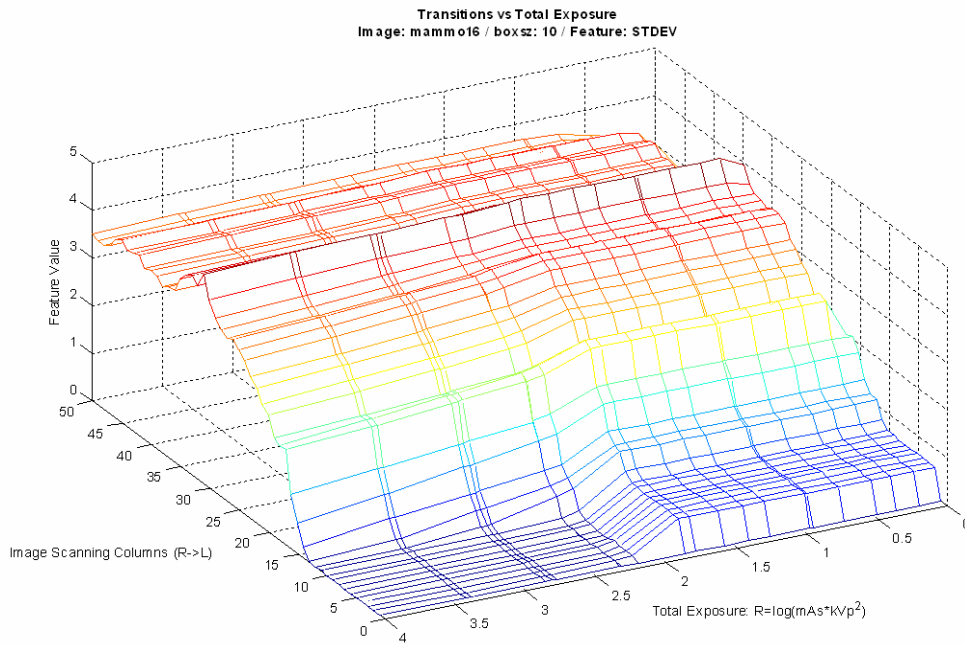


Figure 20: PredModel-1B, textural “signature” profile for STDEV feature function at different exposure settings.

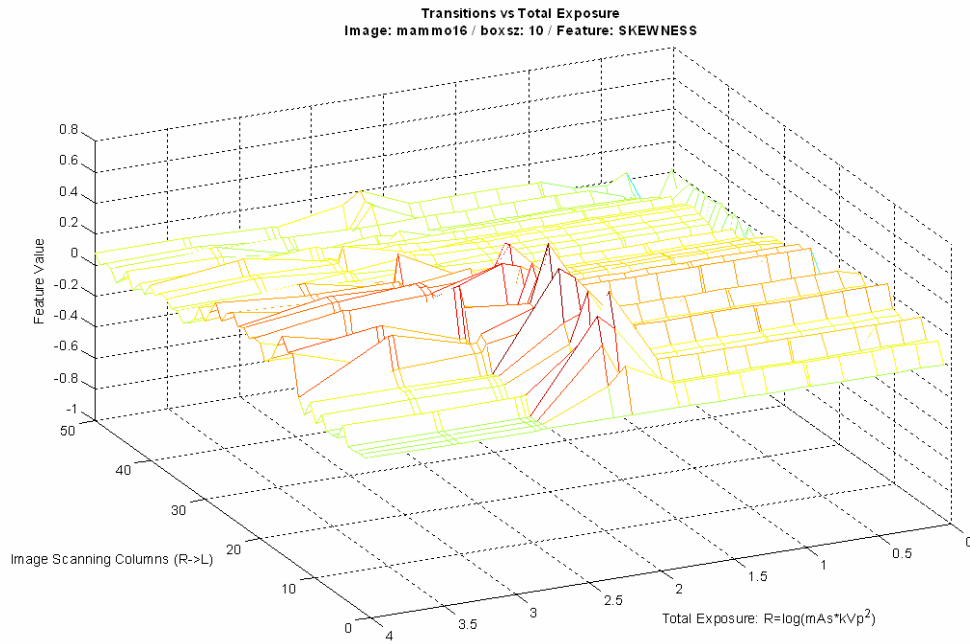


Figure 21: PredModel-1B, textural “signature” profile for SKEWNESS feature function at different exposure settings.

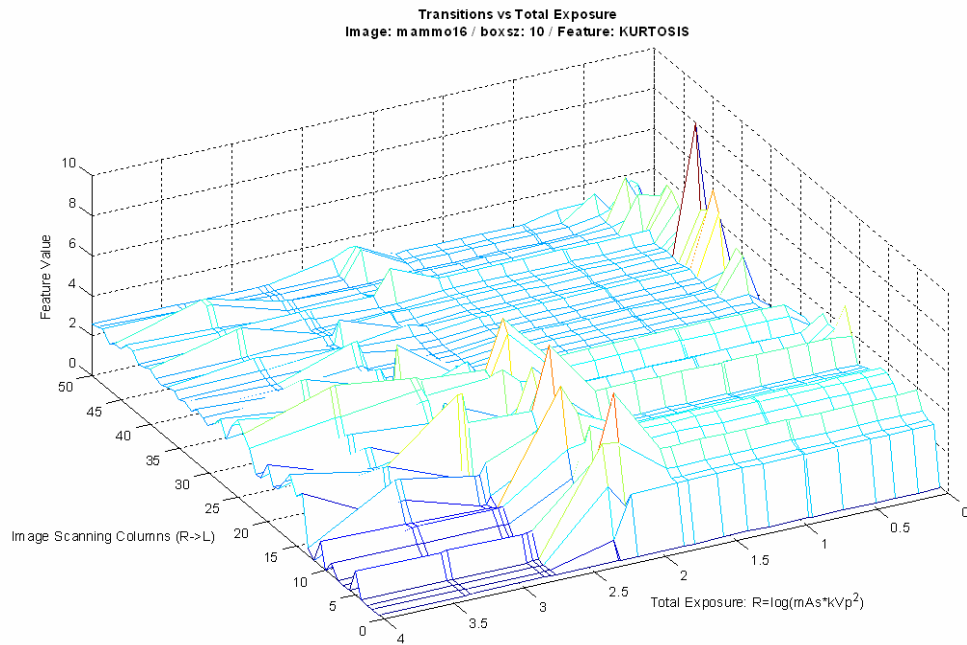


Figure 22: PredModel-1B, textural “signature” profile for KURTOSIS feature function at different exposure settings.

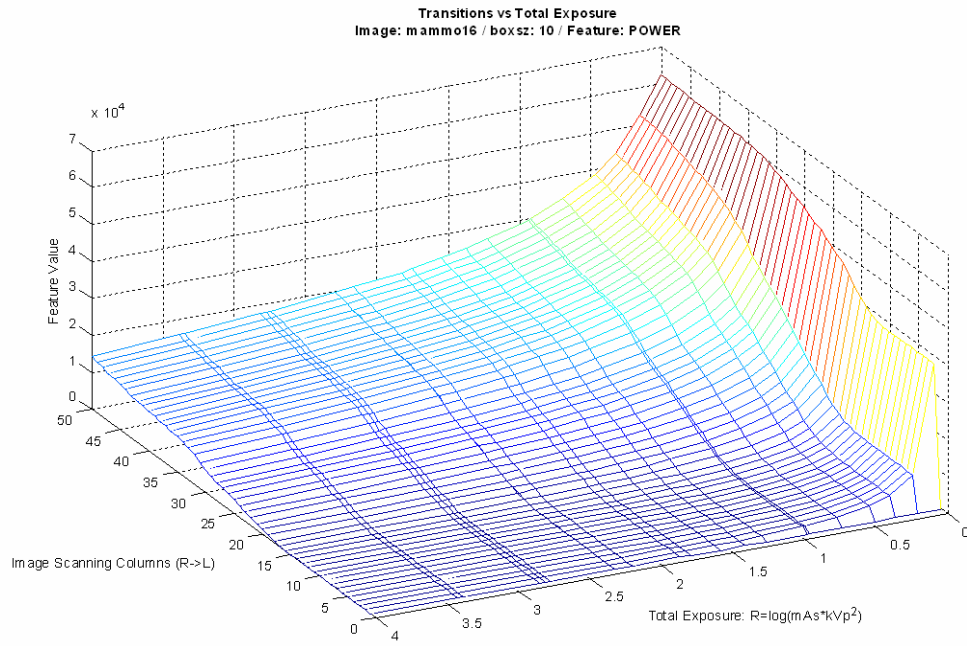


Figure 23: PredModel-1B, textural “signature” profile for POWER feature function at different exposure settings.

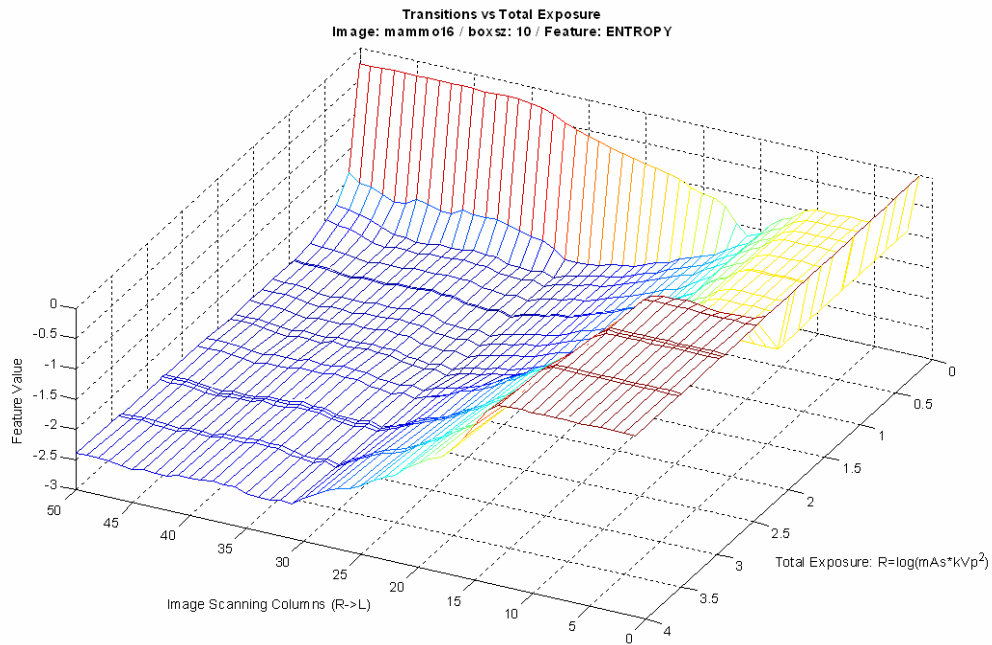


Figure 24: PredModel-1B, textural “signature” profile for ENTROPY feature function at different exposure settings.

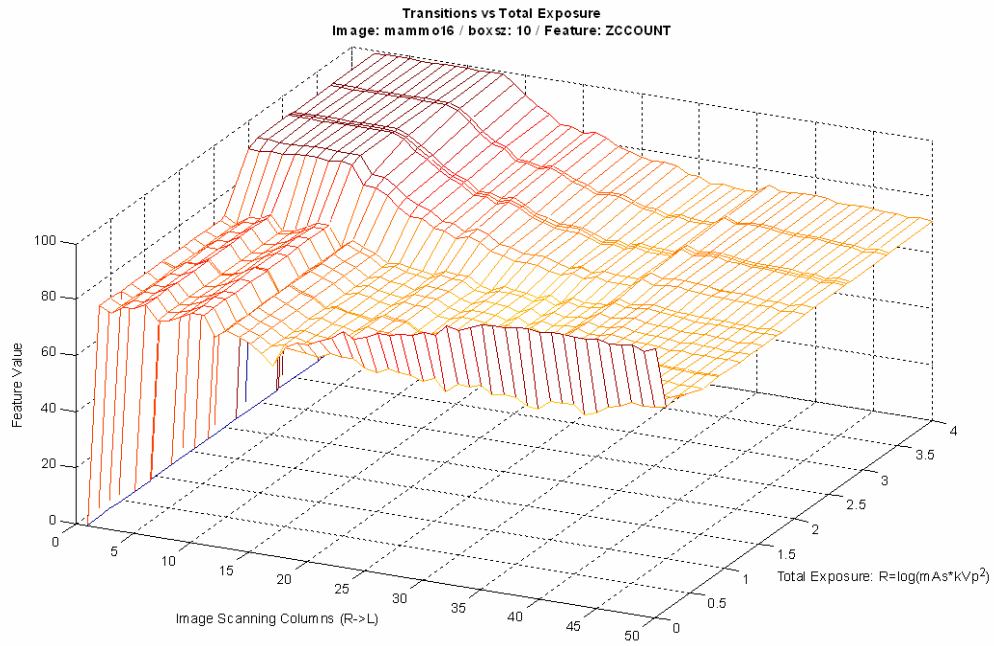


Figure 25: PredModel-1B, textural “signature” profile for ZCCOUNT feature function at different exposure settings.

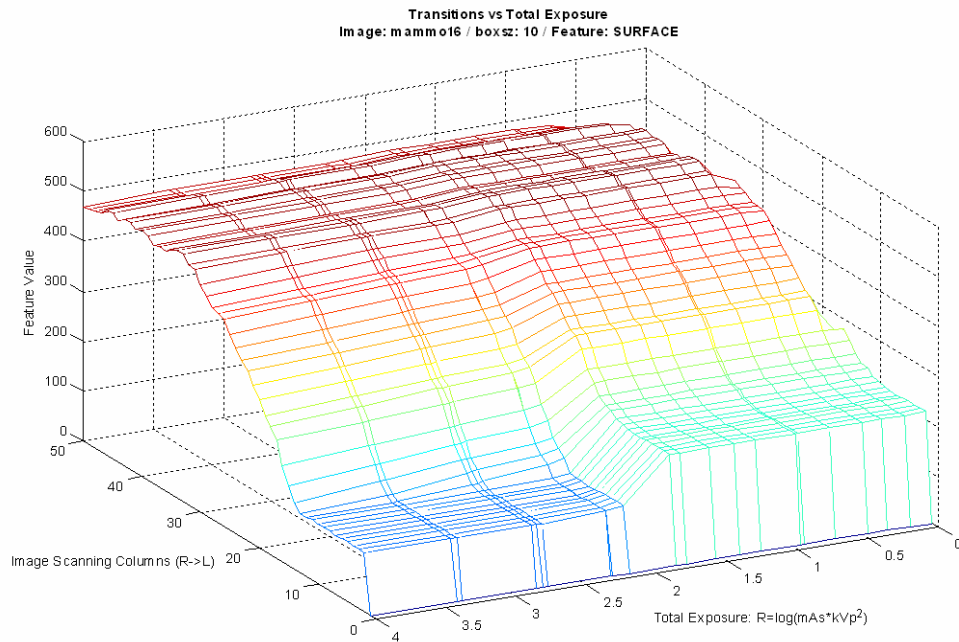


Figure 26: PredModel-1B, textural “signature” profile for SURFACE feature function at different exposure settings.

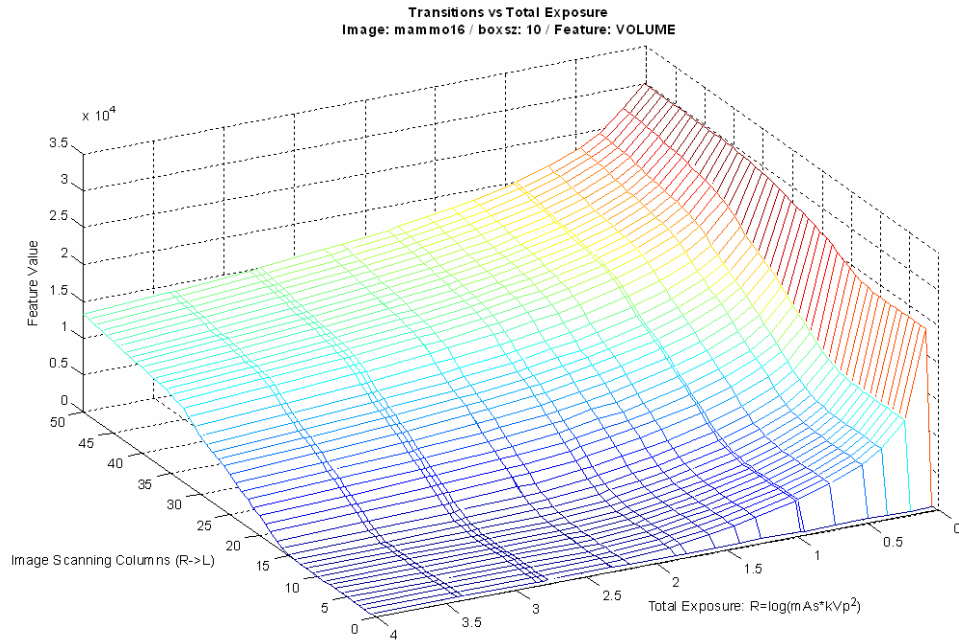


Figure 27: PredModel-1B, textural “signature” profile for VOLUME feature function at different exposure settings.

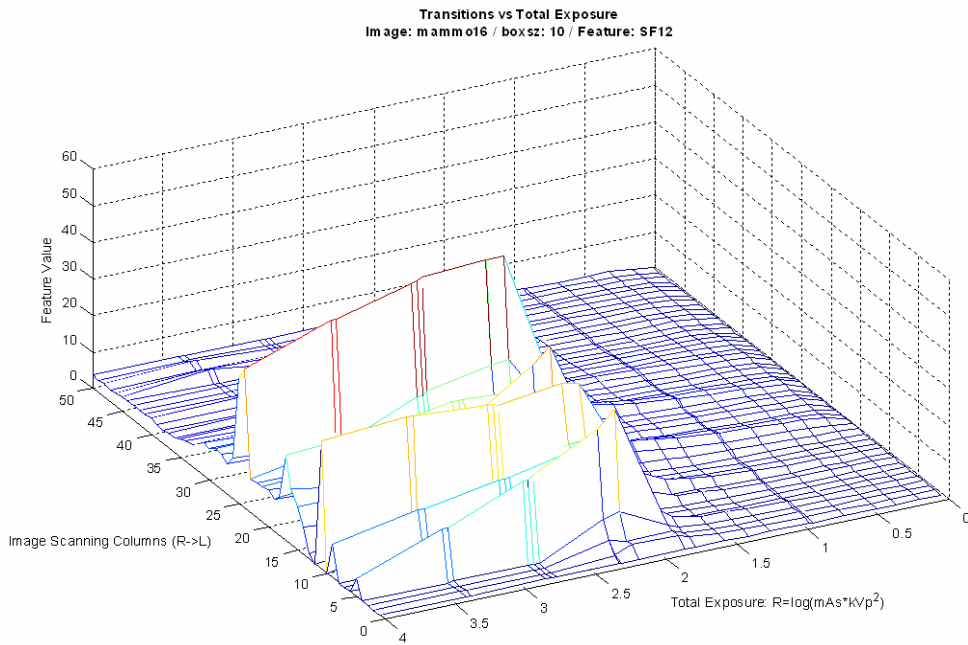


Figure 28: PredModel-1B, textural “signature” profile for SF12 feature function at different exposure settings.

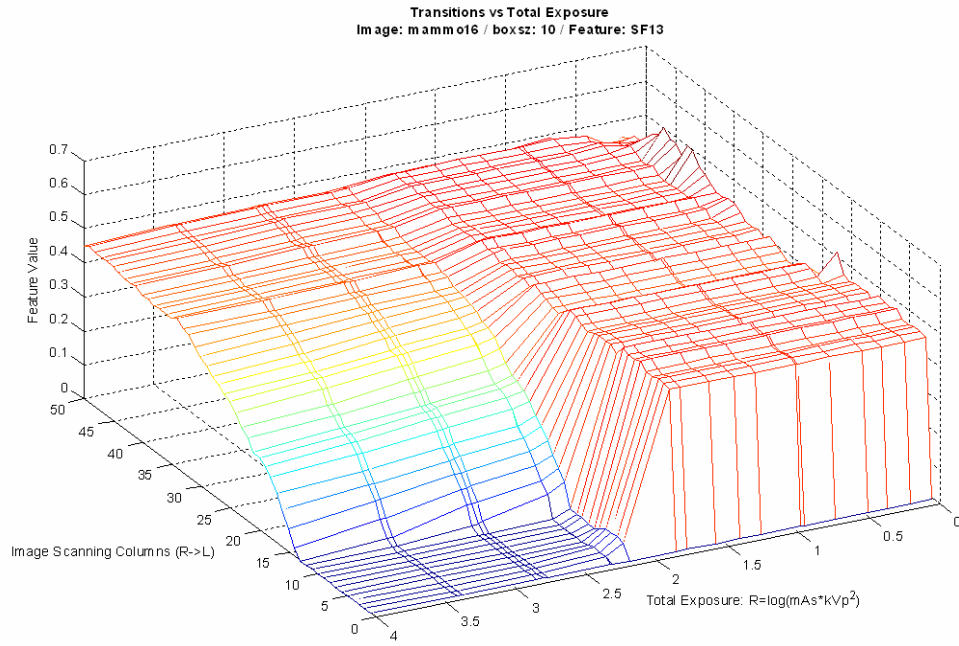


Figure 29: PredModel-1B, textural "signature" profile for SF13 feature function at different exposure settings.

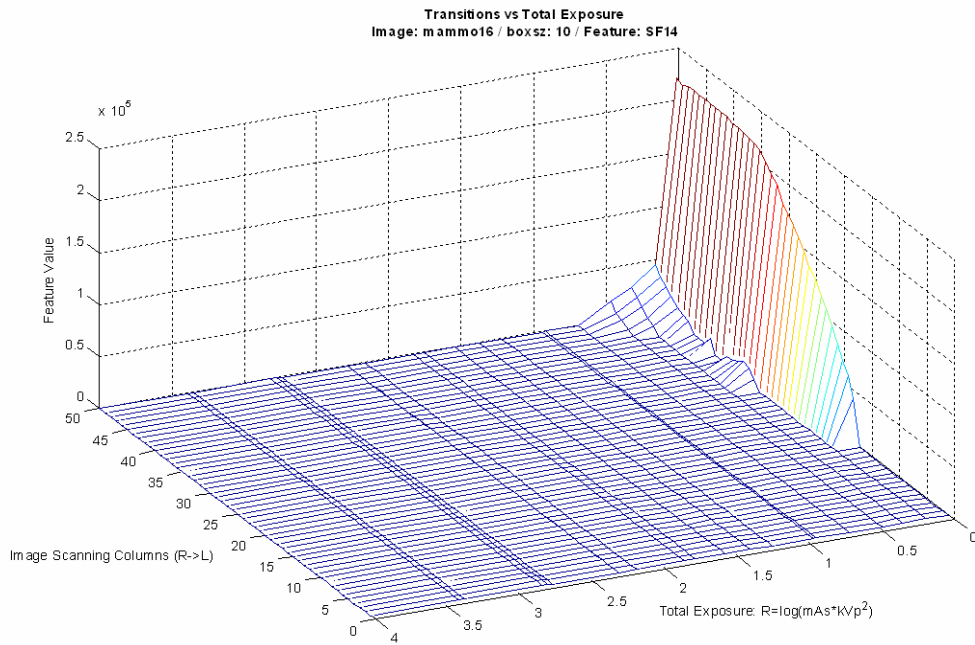


Figure 30: PredModel-1B, textural "signature" profile for SF14 feature function at different exposure settings.

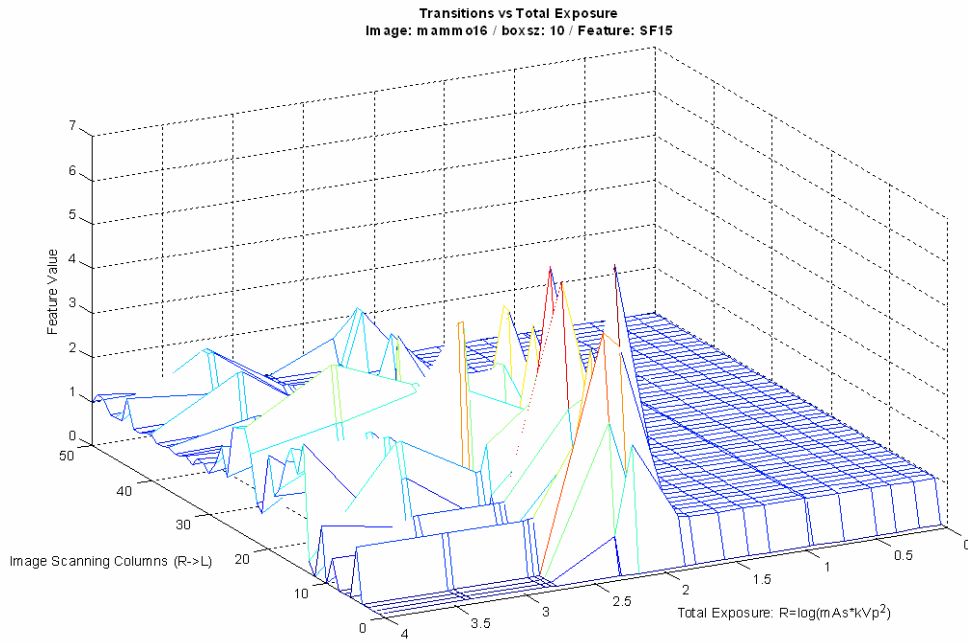


Figure 31: PredModel-1B, textural "signature" profile for SF15 feature function at different exposure settings.

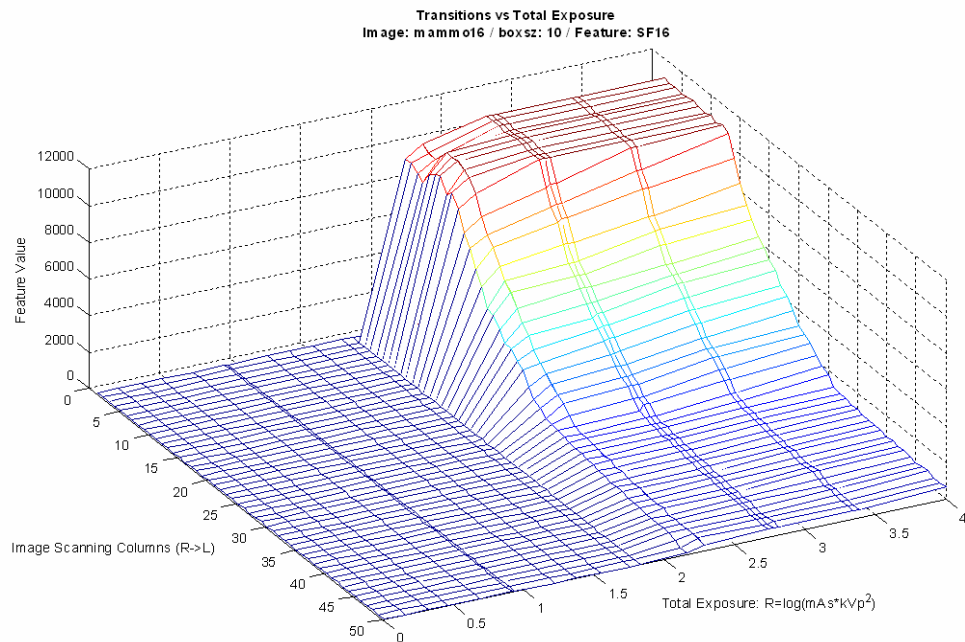


Figure 32: PredModel-1B, textural "signature" profile for SF16 feature function at different exposure settings.

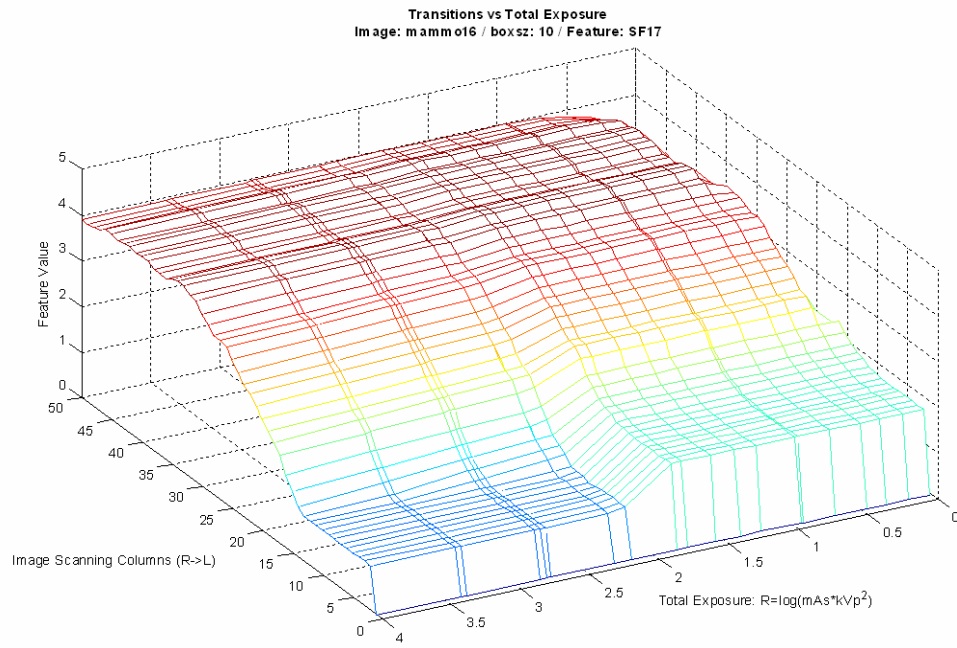


Figure 33: PredModel-1B, textural “signature” profile for SF17 feature function at different exposure settings.

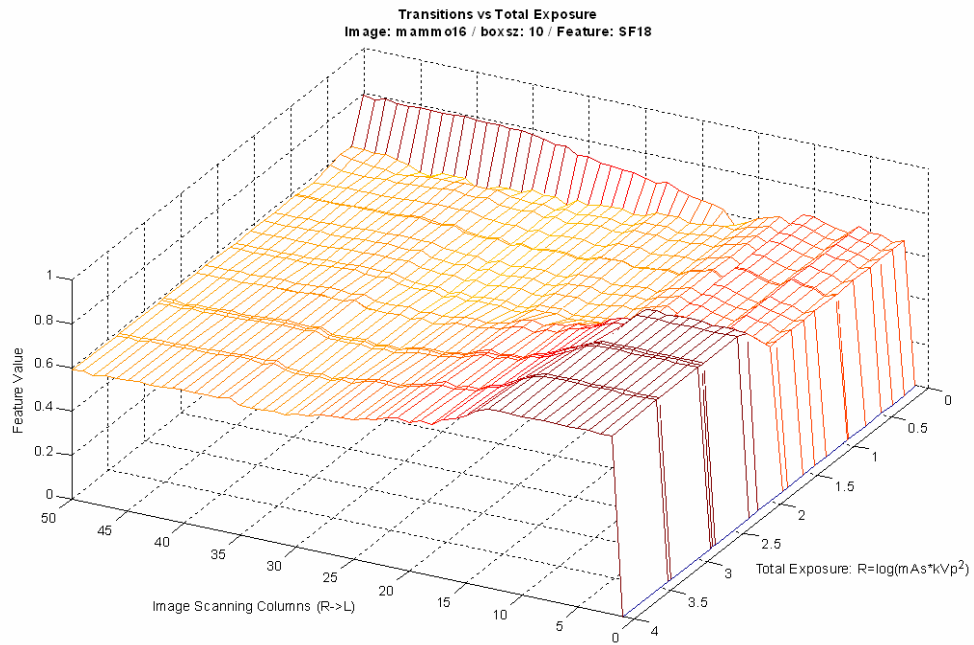


Figure 34: PredModel-1B, textural “signature” profile for SF18 feature function at different exposure settings.

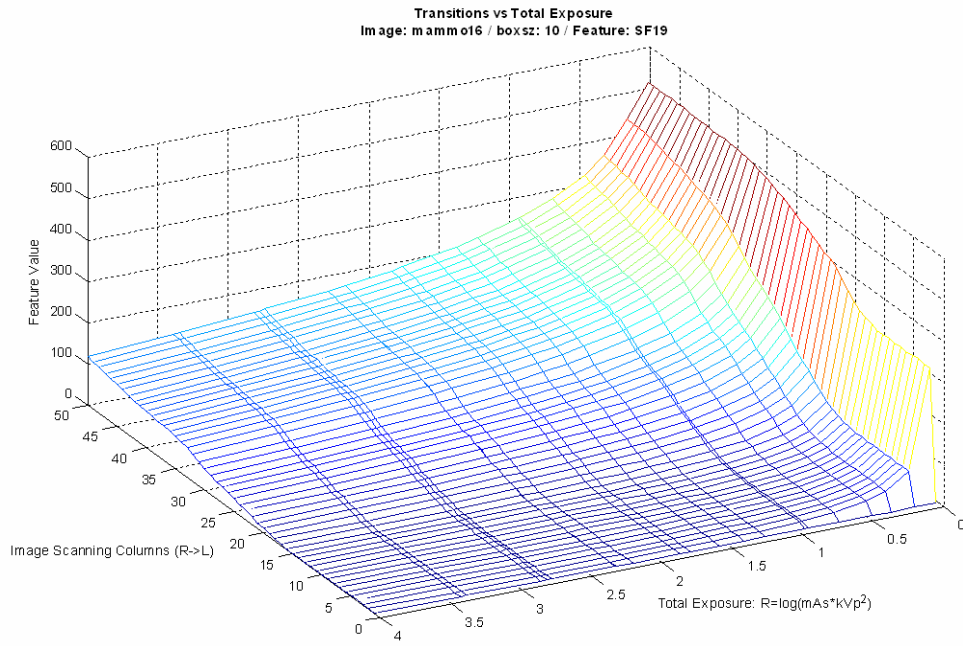


Figure 35: PredModel-1B, textural “signature” profile for SF19 feature function at different exposure settings.

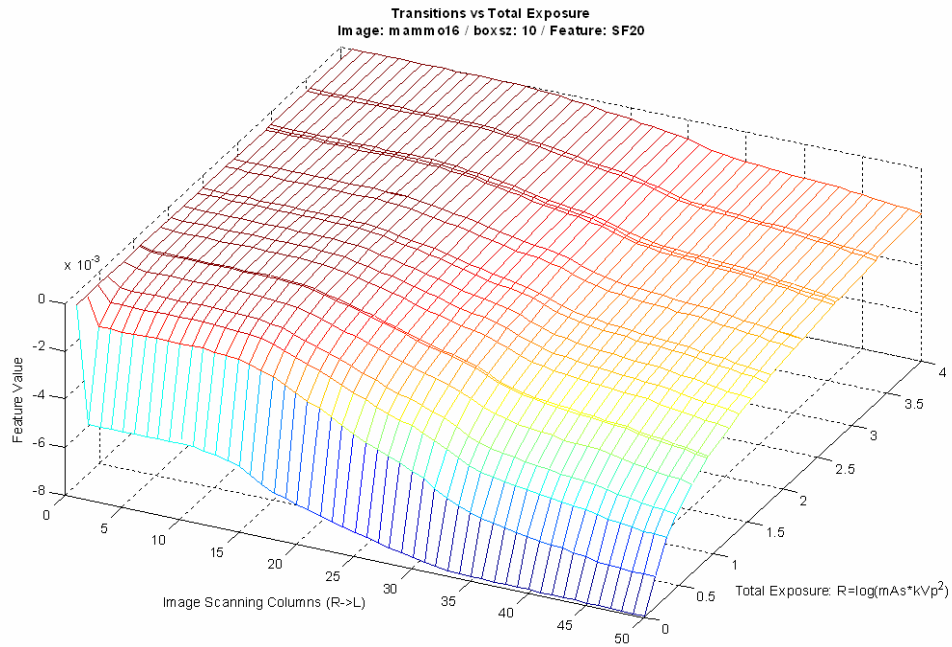


Figure 36: PredModel-1B, textural “signature” profile for SF20 feature function at different exposure settings.

In relation to the sampling box size, Figures 37 and 38 show the resulting plots for SF20 feature function for box sizes of 25 and 50, accordingly.

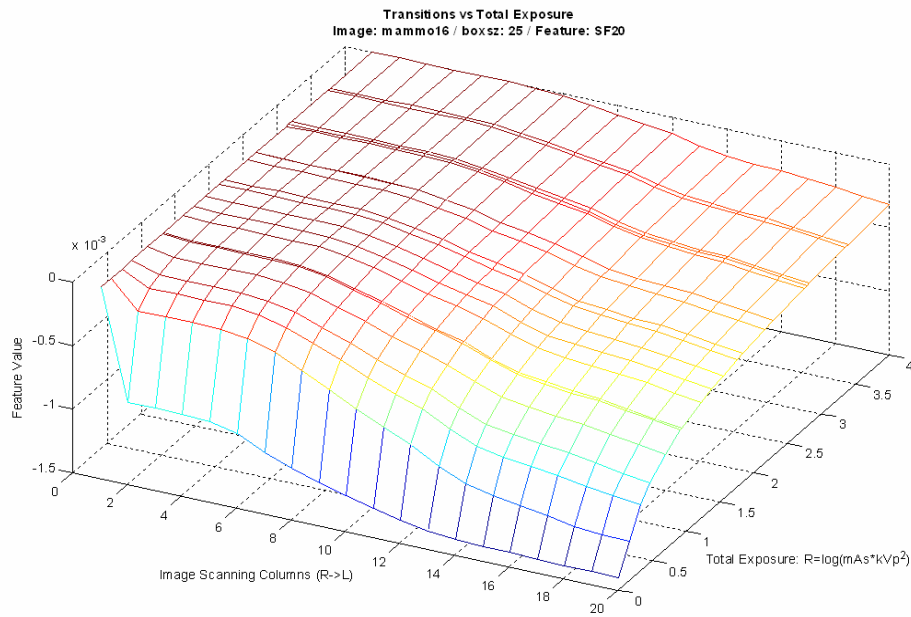


Figure 37: PredModel-1B, textural "signature" profile for SF20 feature function at different exposure settings, for sampling box size $N=25$.

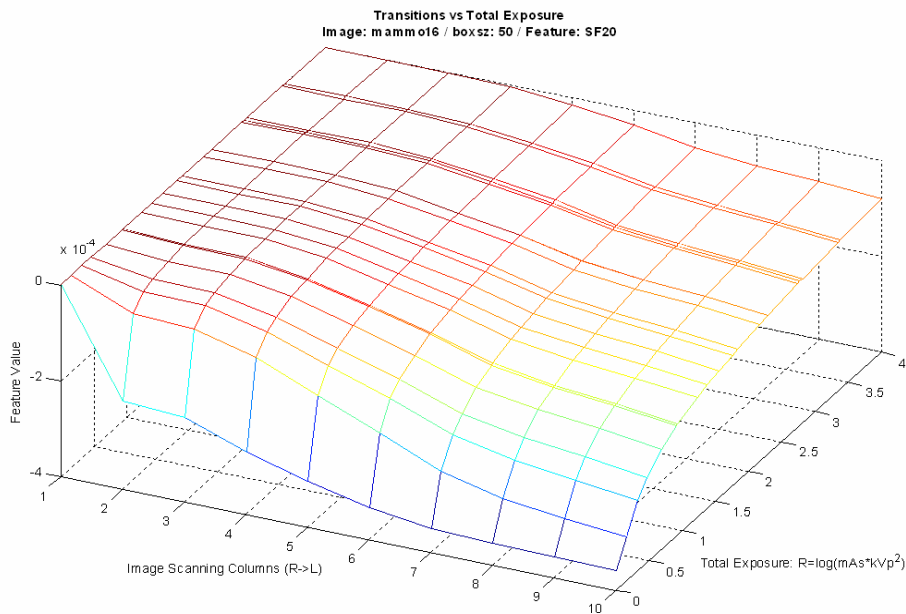


Figure 38: PredModel-1B, textural "signature" profile for SF20 feature function at different exposure settings, for sampling box size $N=50$.

2.6.2 Comparative results & discussion

The results presented in Figures 17 through 38 essentially constitute the visual representation of the textural feature functions performance with regard to their capability to track image quality fluctuations when exposure level changes with respect to either kVp or mAs. Good choices for candidate functions should be able to produce smooth and consistent transitions in both dimensions, namely the line-scanning direction (detection of tissue structures) and the exposure level (image quality versus kVp and/or mAs).

According to these desired properties, Tables 8 through 10 summarize the efficiency of all 20 feature functions, applied for sampling box sizes of 10, 25 and 50 pixels. The final evaluation was conducted through the entire set of 20 initial images (DB1) and their simulated overexposed and underexposed versions.

BOX=10	F01	F02	F03	F04	F05	F06	F07	F08	F09	F10	F11	SF12	SF13	SF14	SF15	SF16	SF17	SF18	SF19	SF20	Sum
Mammo_01																					0
Mammo_02																					0
Mammo_03		√																			1
Mammo_04										√							√				2
Mammo_05	√																			√	2
Mammo_06	√	√	√								√								√	√	6
Mammo_07	√	√	√				√				√								√	√	7
Mammo_08	√	√	√				√				√		√						√		7
Mammo_09	√	√	√							√	√						√		√		7
Mammo_10	√	√	√				√				√		√						√	√	8
Mammo_11	√	√	√				√				√						√		√	√	8
Mammo_12	√																√				2
Mammo_13	√	√	√				√				√		√						√	√	8
Mammo_14										√							√				2
Mammo_15	√	√	√				√				√		√						√		7
Mammo_16	√	√	√				√				√								√	√	7
Mammo_17		√	√				√				√						√		√		6
Mammo_18	√						√				√								√	√	5
Mammo_19	√																			√	2
Mammo_20	√	√	√				√				√								√	√	7
Sum	14	12	11	0	0	0	10	0	0	3	12	0	4	0	0	0	6	0	12	10	

Table 8: PredModel-1B, textural “signature” performance sheet for all feature functions and test images, for sampling box size N=10.

BOX=25	F01	F02	F03	F04	F05	F06	F07	F08	F09	F10	F11	SF12	SF13	SF14	SF15	SF16	SF17	SF18	SF19	SF20	Sum
Mammo_01																					0
Mammo_02																					0
Mammo_03																				√	1
Mammo_04										√							√				2
Mammo_05	√		√				√				√								√	√	6
Mammo_06	√	√	√				√				√								√	√	7
Mammo_07	√	√	√				√				√								√	√	7
Mammo_08	√	√	√				√				√								√		6
Mammo_09	√	√	√				√			√	√						√		√		8
Mammo_10	√	√	√				√				√								√	√	7
Mammo_11	√	√	√				√			√	√		√						√	√	9
Mammo_12																				√	1
Mammo_13	√	√	√				√				√								√	√	7
Mammo_14										√							√				2
Mammo_15	√	√	√				√			√	√		√						√		8
Mammo_16	√	√	√				√			√	√						√		√	√	9
Mammo_17	√	√	√				√				√								√		6
Mammo_18	√	√	√				√				√								√	√	7
Mammo_19											√									√	2
Mammo_20	√	√	√				√				√								√	√	7
Sum	13	12	11	0	0	0	13	0	0	6	14	0	2	0	0	0	4	0	13	12	

Table 9: PredModel-1B, textural “signature” performance sheet for all feature functions and test images, for sampling box size N=25.

BOX=50	F01	F02	F03	F04	F05	F06	F07	F08	F09	F10	F11	SF12	SF13	SF14	SF15	SF16	SF17	SF18	SF19	SF20	Sum
Mammo_01	√		√				√												√		4
Mammo_02																					0
Mammo_03	√	√																	√	√	3
Mammo_04										√	√						√			√	4
Mammo_05	√	√	√				√				√								√	√	7
Mammo_06	√	√	√				√				√								√	√	7
Mammo_07	√	√	√				√				√								√	√	7
Mammo_08	√	√	√				√				√								√	√	7
Mammo_09	√	√	√				√			√	√						√		√	√	9
Mammo_10	√	√	√				√				√								√	√	7
Mammo_11	√	√	√				√				√								√	√	7
Mammo_12	√										√									√	3
Mammo_13	√	√	√				√				√								√	√	7
Mammo_14											√										1
Mammo_15	√	√	√				√			√	√						√		√	√	9
Mammo_16	√	√	√				√			√	√								√	√	8
Mammo_17	√	√	√				√				√								√		6
Mammo_18	√	√	√				√				√								√	√	7
Mammo_19	√	√	√				√				√								√	√	7
Mammo_20	√	√	√				√				√								√	√	7
Sum	17	14	15	0	0	0	15	0	0	4	17	0	0	0	0	0	3	0	16	10	

Table 10: PredModel-1B, textural “signature” performance sheet for all feature functions and test images, for sampling box size N=50.

It is clear that candidate feature functions that were identified by visual review of the intermediate 2-D texture data from PredModel-1A are actually verified here as the best choices for feedback to the sensor control. Feature functions with smooth and consistent behavior can be easily located in all three tables by isolating columns with large “positive” sums in the very last row. Best selections are functions that generally relate to sum of pixel values or squared pixels values. The final feature functions candidates for the final choice of feedback are:

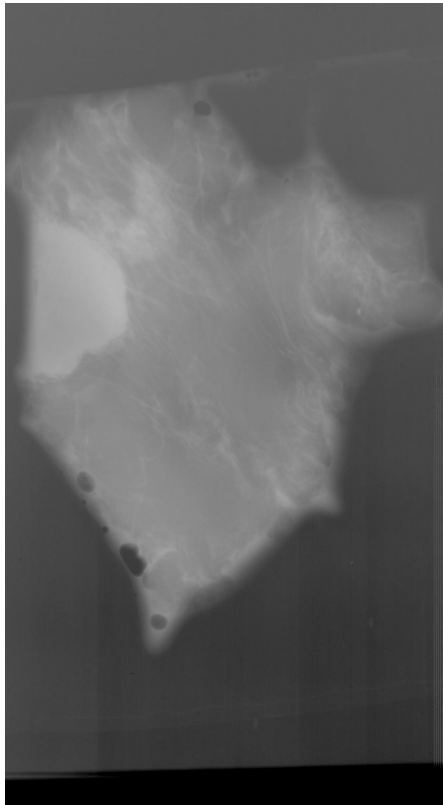
- F01: MIN value
- F02: MAX value
- F03: MEAN value
- F04: STDEV value (only for boundary detection)
- F07: signal POWER
- F11: VOLUME metrics
- SF19: (normalized POWER)
- SF20: (normalized EXPOSURE)

Although some images proved to be generally poor with regard to their information content, almost all feature functions performed consistently throughout the image set and proving that results are statistically unbiased, i.e. there are no special “preferences” of some feature functions to some images. Actually, these images are cases of very dense breast tissue where the internal tissue structure is difficult to distinguish even in the original image where the exposure settings are optimal.

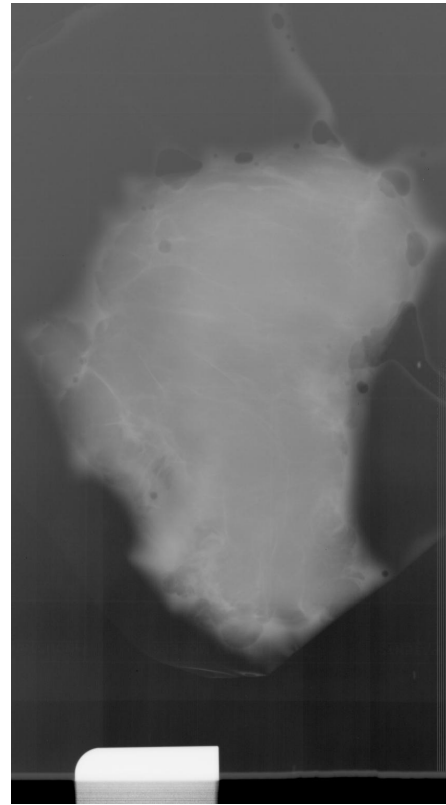
Table 10 also confirms the assertion that using larger sampling box sizes should lead to content-rich feature values. Large samples of local image areas include fine structural details at greater scales, thus producing texture “signatures” of better quality in terms of capturing the complexity and spatial morphology of the underlying image, an aspect of great importance for assessing the quality of the image itself. However, the shape and smoothness of the transition hyperplane of the best candidate feature functions does not seem to be affected by having lower or higher resolution on the texture data. This is an indication of good information content encoding into a compact texture “signature” for the scanned image, as well as stability and consistency for the feature function itself.

2.7 Real breast tissue image database (DB3)

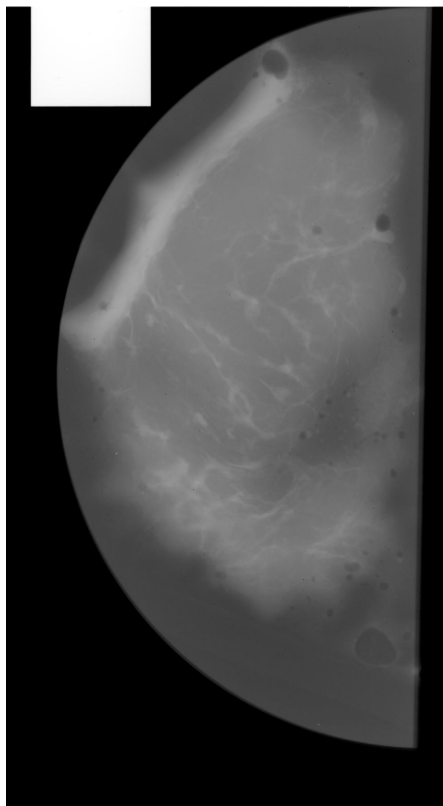
In order to assess the true efficiency of each textural feature function used in the previous phase, a new comprehensive image database was constructed (DB3). The new images were acquired in a Siemens Mammomat B X-ray machine, using real breast tissue samples as target and acquiring images of the same target at various kVp and mAs settings.



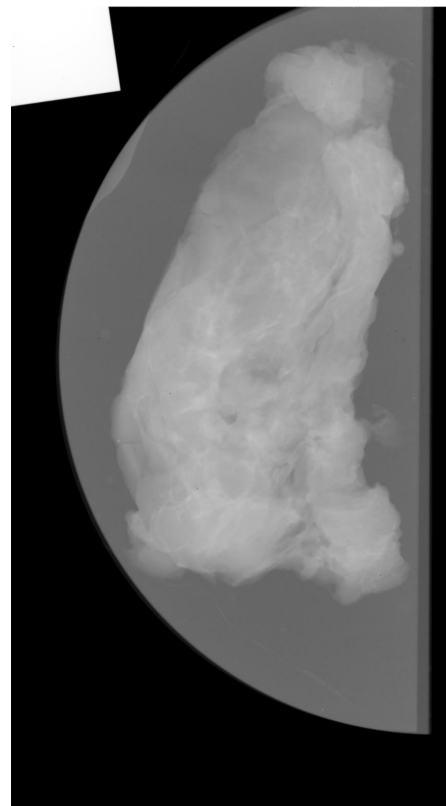
Tissue A: "U01"



Tissue B: "U02"



Tissue C: "U03.02"



Tissue D: "U04.03"

Figure 39: Samples from all four image sets contained in the DB3 image database

The Siemens Mammomat B provided an overall specifications profile adequately close to the current I-ImaS design, although the true spatial resolution (7 lp/mm) and true spatial resolution (127 μm) are both much lower. The greylevel depth used for ADC was 12-bit and the actual ranges used during these experiments were between 28 and 35 for kVp, and (selectively) between 3.2 and 80 for mAs.

The Bart's tissue phantom was used with four different breast tissue samples, packed with appropriate absorption layers to simulate the standard 4.5 cm UK breast thickness. The four distinct sets contained a total of 125 images, employing various aspects of image texture and X-ray properties including void areas for noise and artifacts estimation, normal tissue areas, malignant tumor sample and unexposed regions (Figure 39).

Due to the inherently different size and alignment of each of the four tissue samples, each set was considered and analyzed separately, before a general assessment could be made over the entire DB3 database samples and the evaluation of the specific textural features. All sets were reviewed by expert radiologists and were verified as acceptable in terms of overall quality and clinical value, before any further processing was made.

2.8 PredModel-2A/B: Textural Features Validation

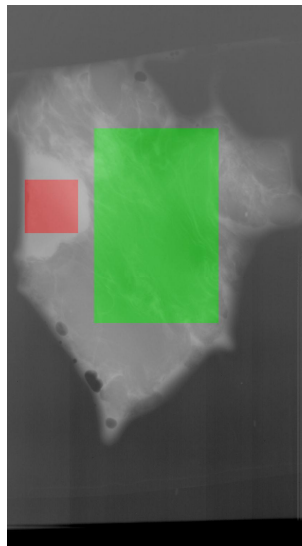
The basic application frameworks that were created for implementing both PredModel-1A, for textural features extraction, and PredModel-1B, for textural features evaluation, were combined into a compact and robust set of modules that was used for processing the new DB3 images in a similar way. Specifically, PredModel-2A/B included all the textural feature extractors and the statistical analysis code that was necessary to conduct a comparative study of the DB3 image sets, investigating the sensitivity of the results over the different tissue samples and validating the conclusions already drawn from the study thus far regarding the efficiency of the various feature functions.

Due to the nature and content of the new image sets, a slightly different approach was employed for comparative texture evaluation. Specifically, the use of tissue samples, instead of complete breast mammograms, prohibited the employment of analytical line-scanning procedure in the same way that was used in PredModel-1A. The lack of exact tissue orientation and location within the complete breast area could result into misleading conclusions, regarding the response curve of the line-scanning texture extraction procedure. Instead, texture was evaluated as before, but results were analyzed in a more compact form, using the complete sampling area as the base for the final feature value used when comparing it against different exposure rates. Thus, the efficiency of each feature function was evaluated for the same tissue and for different settings of kVp/mAs, using single values instead of the full 2-D output.

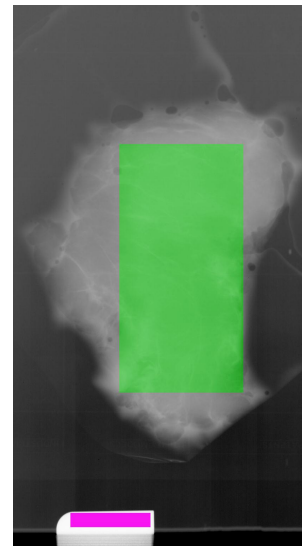
The PredModel-2A/B study was focused on four different areas:

- (a) Confirmation of SimModel-1A over exposure and optical density responses
- (b) Global statistics, including noise estimation and greyscale usage.
- (c) Efficiency and stability analysis of all 20 texture feature extractors.
- (d) Effects of standard pre-processing, acquisition artifacts, etc.

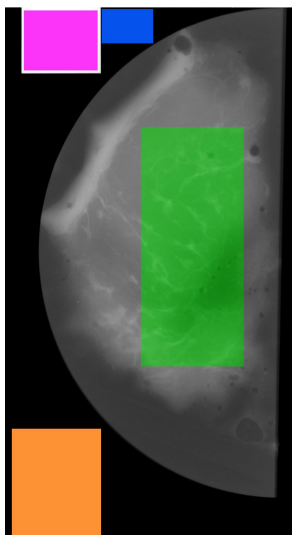
All four areas of studies were conducted separately for each of the four different tissue samples and the final results were studied comparatively in order to verify the final conclusions. Not all tissue sets contained the same content type, thus different acquisition and analysis schemes were applied to each one of them, according to the image content and clarity of the sampling areas of interest. Figure 41 presents all the scanning regions employed in each of the tissue sets, including global statistics, normal tissue, malignant tumor and background artifacts.



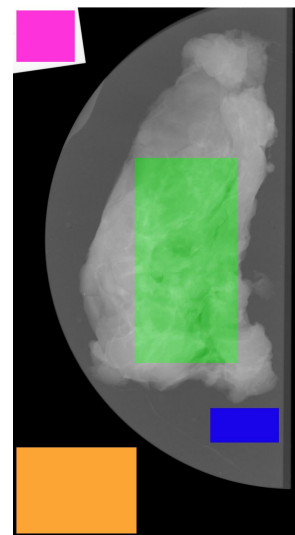
Tissue A: "U01"



Tissue B: "U02"



Tissue C: "U03.02"



Tissue D: "U04.03"

Figure 40: Sampling areas (ROIs) in all four tissue sets included in the DB3 image database, containing normal tissue (green), malignant tissue (red), saturated background (orange), unexposed area (magenta) and background patterns (blue) created by tissue wrapping and/or perspex absorption layers.

All results were investigated against the two basic control parameters, namely the kVp and mAs. For 1-D presentation of exposure rates, true surface dose was also measured during the acquisition experiments, using an ionization chamber placed next to the tissue sample at a height level with the top surface of the perspex, and with perspex below to give a more accurate estimation of the surface dose due to incident x-rays and the contribution from back scatter in the target.

Basic pre-processing of the raw image included a logarithmic re-scaling of the greyscale histogram, by employing normalized gamma correction transformation to the complete 12-bit range. Three gamma values were used, namely 0.62 (darker), 1.00 (normal) and 1.60 (brighter), effectively producing symmetric alterations of the overall illumination of the original image at $\pm 11.6\%$ respectively. The decision on using only full-range histogram manipulation, instead of local/adaptive optimization, was based on the fact that localized processing of single scanning "strips" in the final implementation are very likely to produce non-uniform greyscale transitions between subsequent scanning areas. No further pre-processing or pre-filtering of the raw image data was employed, in order to prevent any loss of significant structural details and noise statistics.

2.8.1 Confirmation of SimModel-1A over exposure and optical density responses

SimModel-1A contained rough estimations of the linear dependency of OD against exposure when simulating the effective changes of fixed images. Preliminary analysis of the efficiency of textural feature extractors was partly based on the correctness of SimModel-1A, thus it is essential to confirm these results by investigating the model parameters against the acquired image data.

First, overall SimModel-1A dose calculation was compared to true dose measurements, against the corresponding kVp and mAs. The calculation formula, i.e:

$$Rx: f_1(kVp, mAs) = C_{1,1} \cdot \log_{10}\{(kVp)^2 \cdot (mAs)\} + C_{1,0}$$

was formulated for a typical dose range and assuming logarithmic scaling, over 2nd-degree kVp and 1st-degree mAs dependence. Table 11 contains the optimal parameters for fitting the dose measurements over each of the image sets and Figures 41-44 shows the corresponding plots.

Image set	#images	$C_{1,1}$	$C_{1,0}$	Mean Error	Stdev Error
U01	22	0,000105	0,3916440	10,08%	6,77%
U02	27	0,000105	0,3958910	10,62%	6,59%
U03.02	36	0,002794	16,021653	11,75%	8,82%
U04.03	40	0,002672	19,561620	11,06%	7,99%

Table 11: SimModel-1A dose approximations for all image sets in the DB3 database.

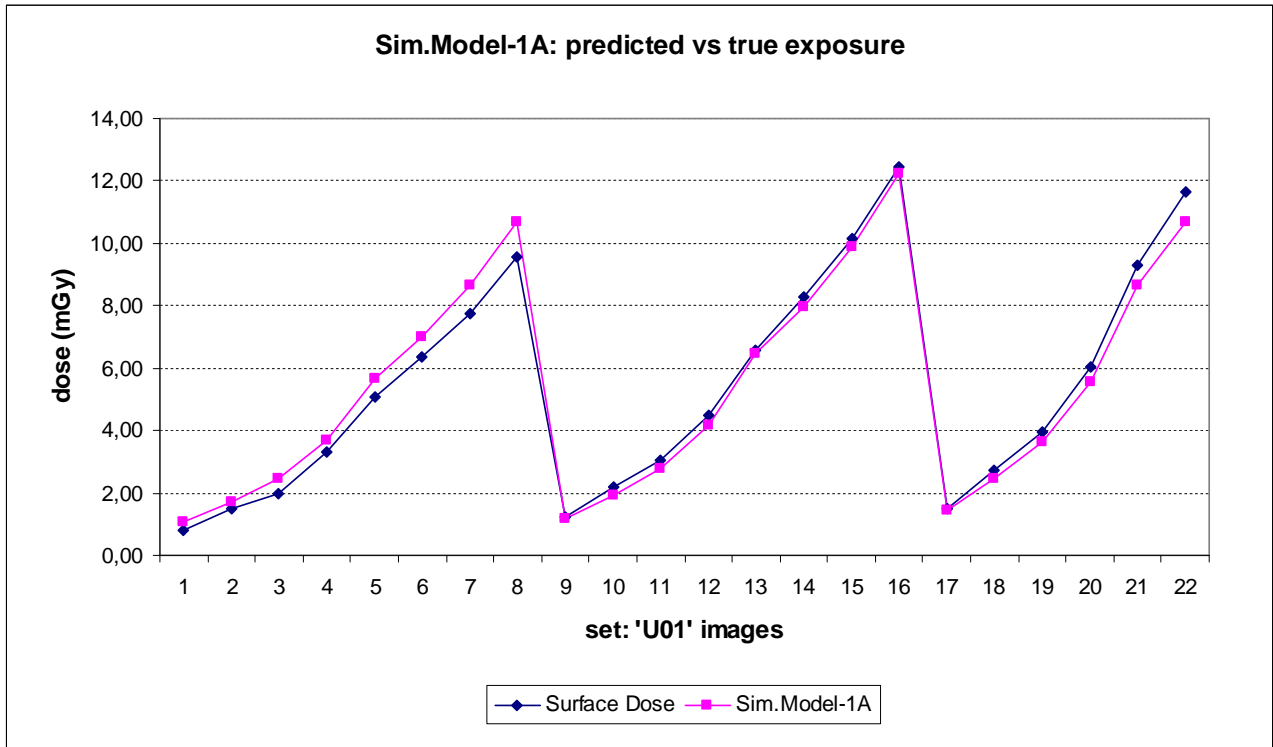


Figure 41: SimModel-1A dose approximations for all images in the “U01” set of DB3 database.

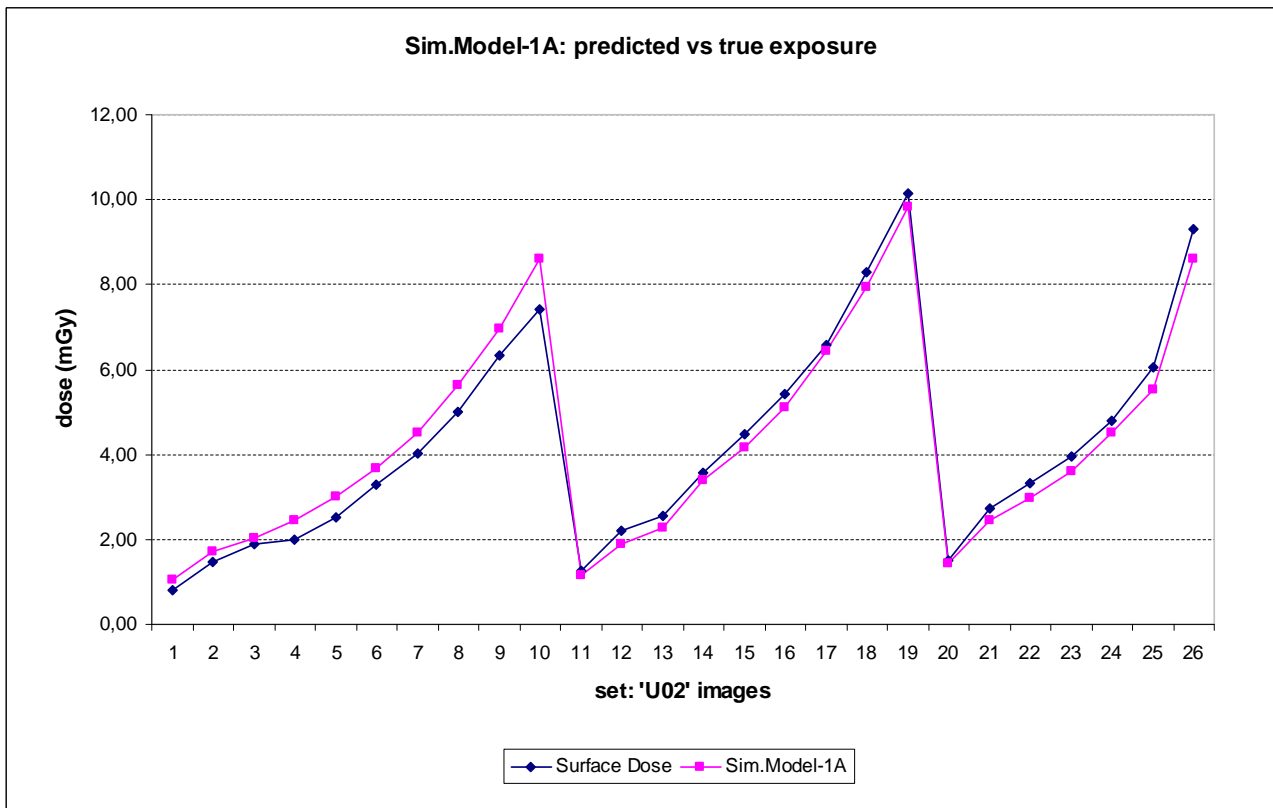


Figure 42: SimModel-1A dose approximations for all images in the “U02” set of DB3 database.

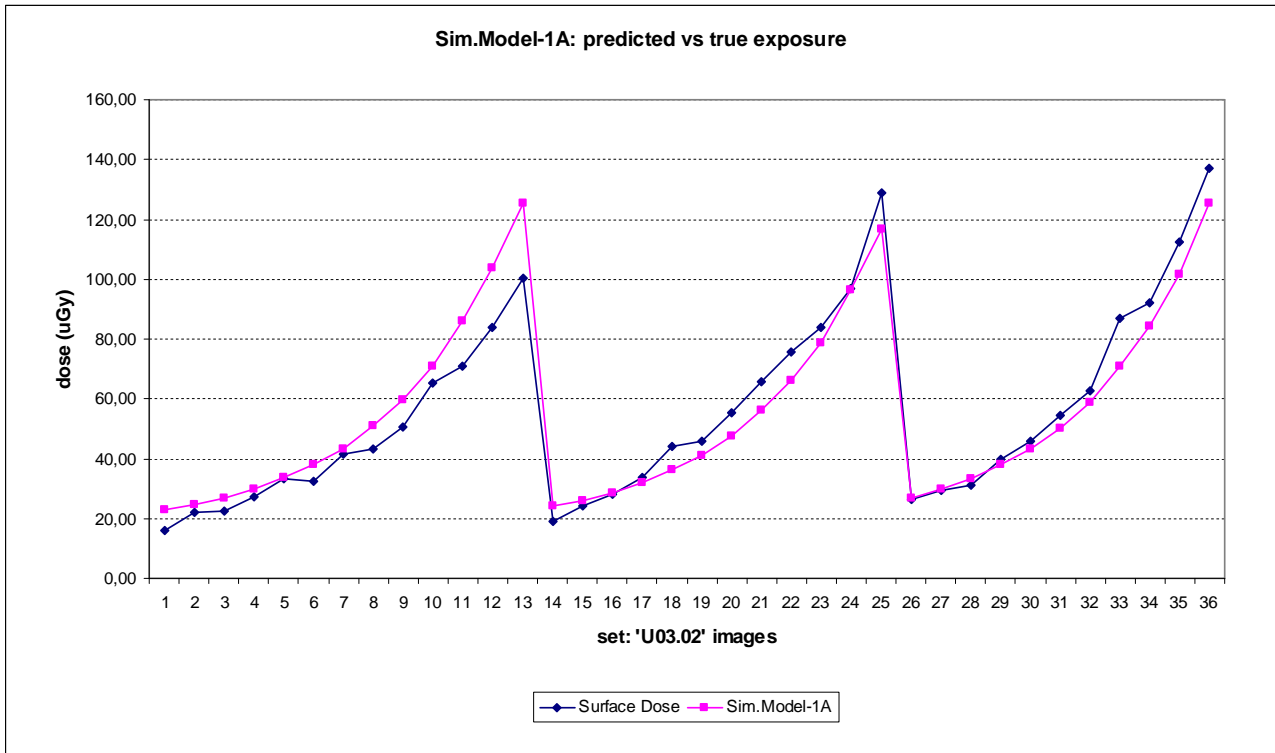


Figure 43: SimModel-1A dose approximations for all images in the “U03.02” set of DB3 database.

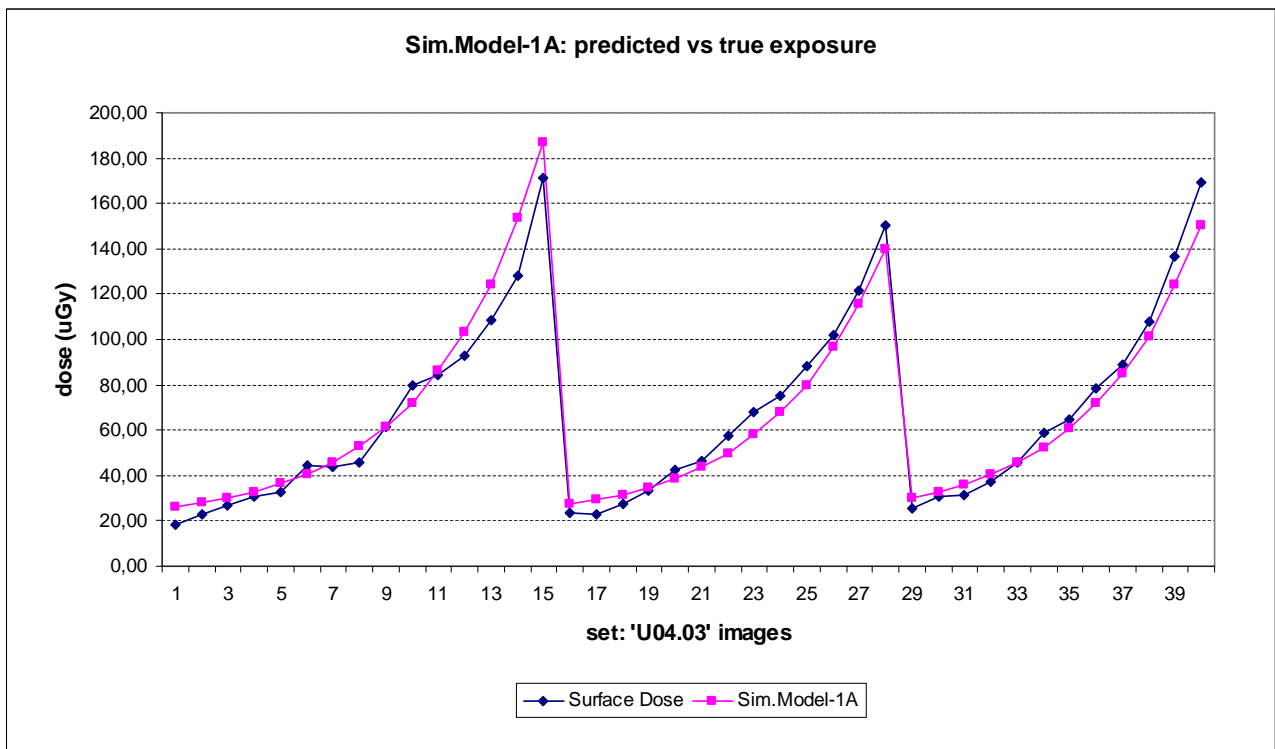


Figure 44: SimModel-1A dose approximations for all images in the “U04.03” set of DB3 database.

Results show that the formulation employed in the first stage of SimModel-1A closely approximates the real exposure measurements in all cases. Differences in the exact values of the parametric model can be justified by the fact that only two pairs of image sets were acquired in roughly the same target configurations, namely "U01" with "U02" and "U03.02" and "U04.03", and thus the resulting actual ranges for dose are not the same. In all cases, the error percentage is between 10%-12% and thus the approximation results can be considered as acceptable.

Next, before evaluating the properties of noise and greyscale, it is essential that the linear response of the detector is also confirmed. SimModel-1A assumed linear response that is characteristic to modern digital mammographic X-ray machines. Optical density was assessed via the translated mean value of homogeneous saturated (black) areas, as shown on Figure 40 (orange). Only "U03.02" and "U04.03" tissues were included in this analysis, as they were the only ones containing these sampling areas in adequate extent and quality. The following plots demonstrate the statistical correlation of optical density (OD) against measured (true) dose.

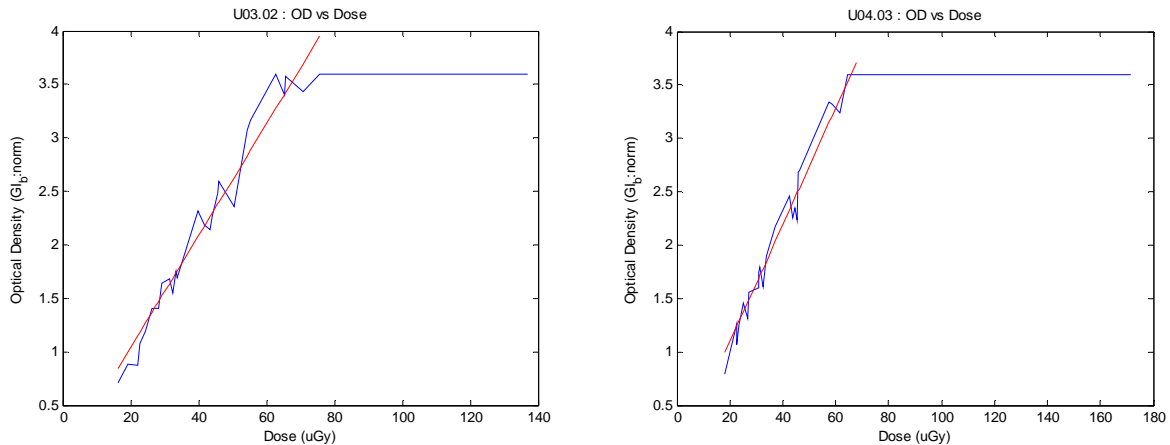


Figure 45: Optical density response against effective dose, for sets "U03.02" and "U04.03".

Although optical density becomes constant (full black) for a large part of the dose scale, it is clear that for the correlation over the normal, non-saturated ranges is mostly linear. Thus, any further calculation of global and local statistics on the raw data of any acquired image from the DB3 database can be considered fully compatible with the SimModel-1A formulation.

2.8.2 Global statistics against exposure rates

The study of global statistics was focused on RMS(%) noise estimation and greyscale utilization against various exposure rates. RMS(%) noise was evaluated via standard deviation over homogeneous saturated areas, while effective greyscale ranges were estimated by calculating the mean values over homogeneous saturated (black) and unexposed (white) areas. Corresponding sampling regions are shown in Figure 40, colored in orange and magenta, respectively. Only "U03.02" and "U04.03" tissues were included in this analysis, as they were the only ones containing both these sampling areas in adequate extent and quality.

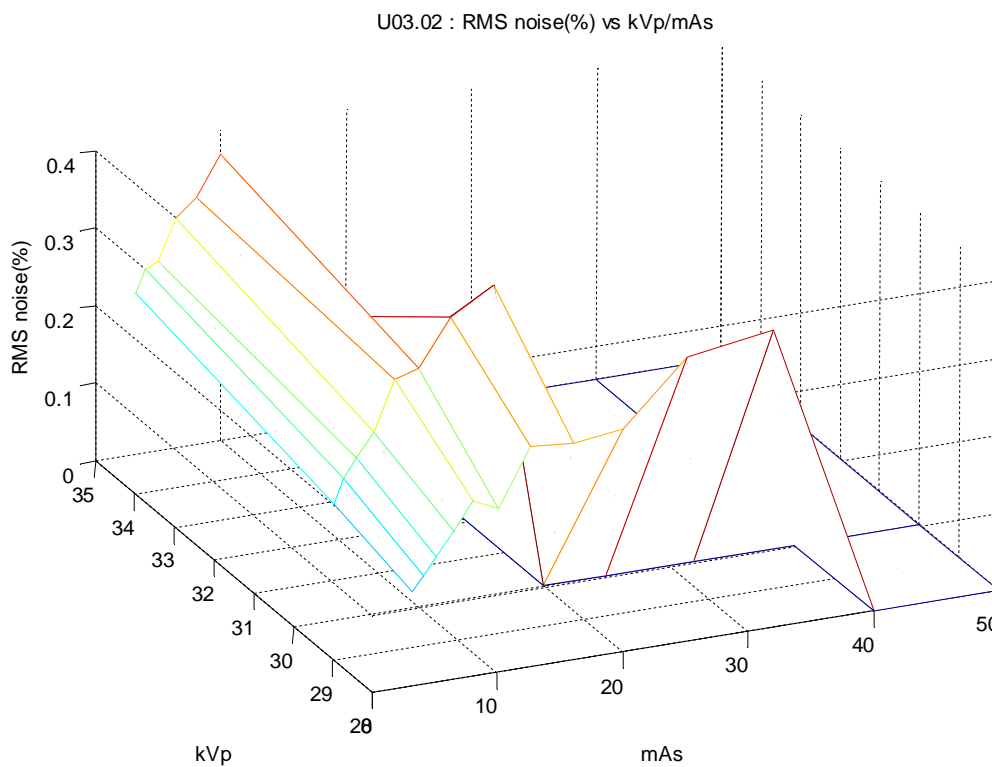


Figure 46: RMS(%) noise estimation against kVp and mAs, for image set "U03.02".

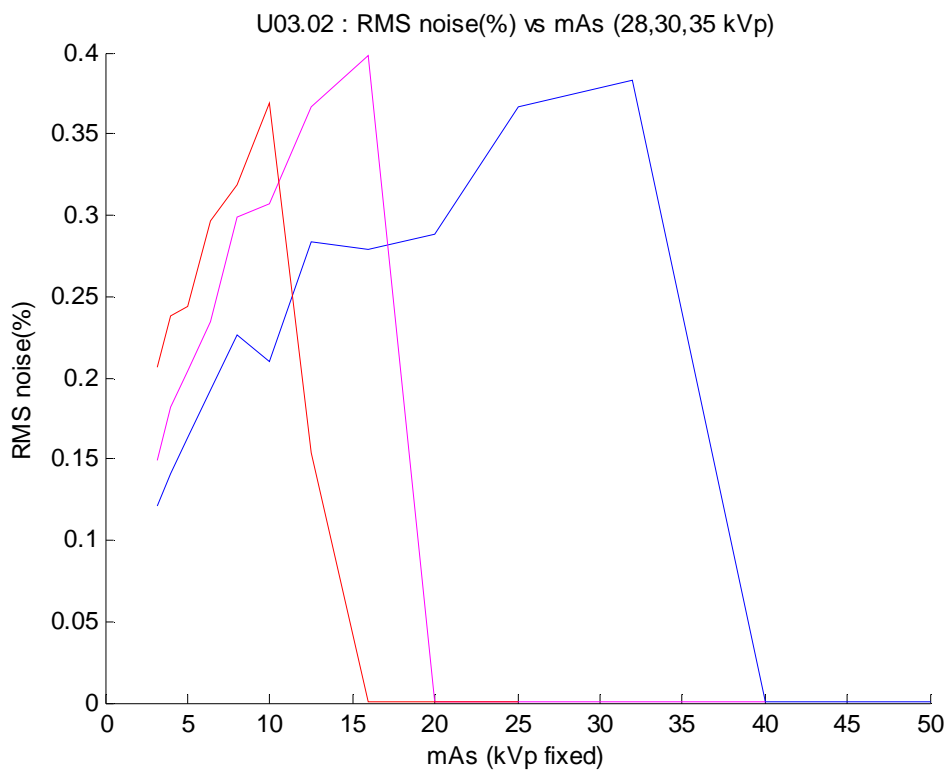


Figure 47: RMS(%) noise estimation against mAs (kVp: 28,30,35), for image set "U03.02".

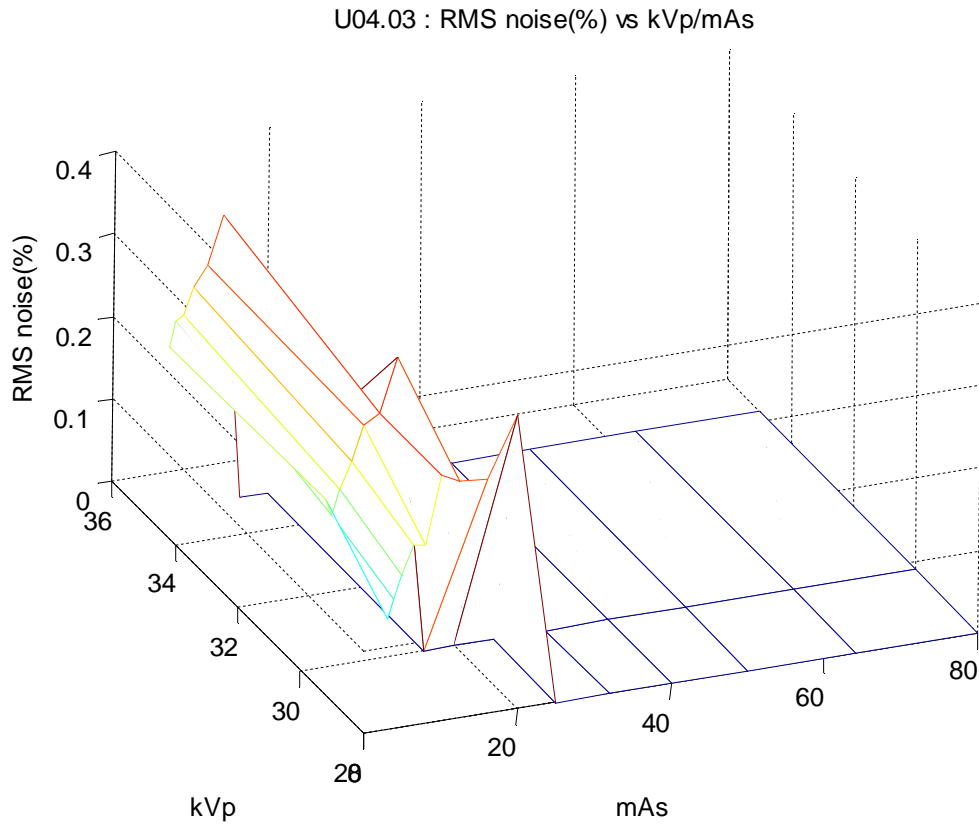


Figure 48: RMS(%) noise estimation against kVp and mAs, for image set "U04.03".

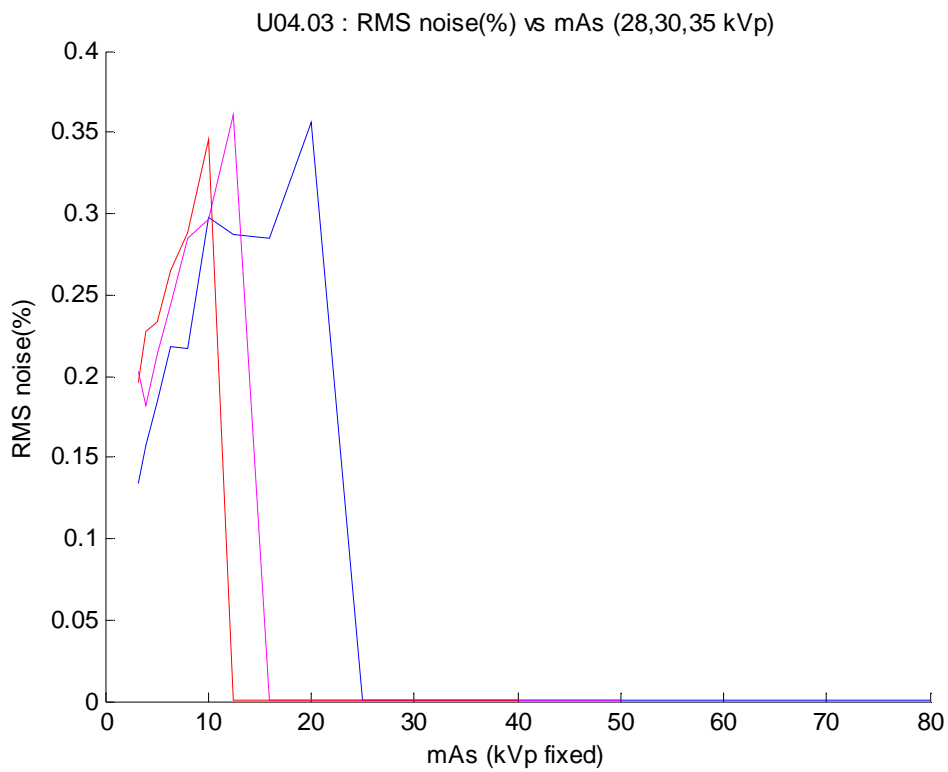


Figure 49: RMS(%) noise estimation against mAs (kVp: 28,30,35), for image set "U04.03".

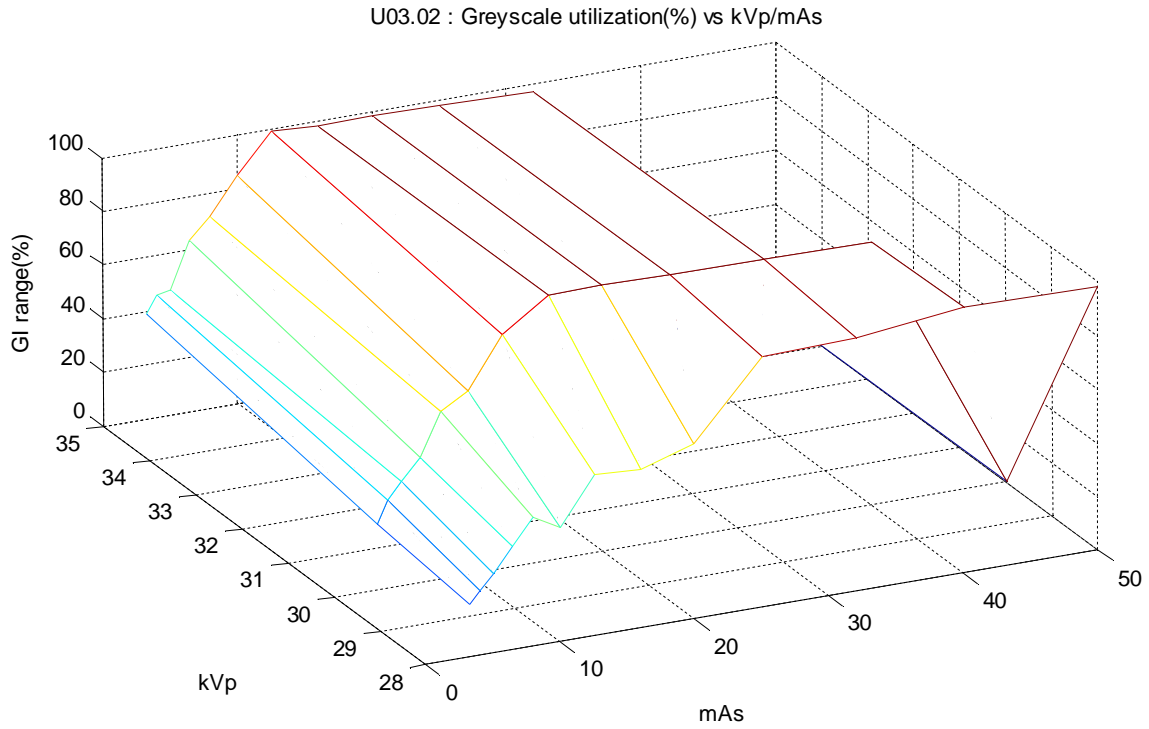


Figure 50: Greyscale utilization(%) estimation against kVp and mAs, for image set "U03.02".

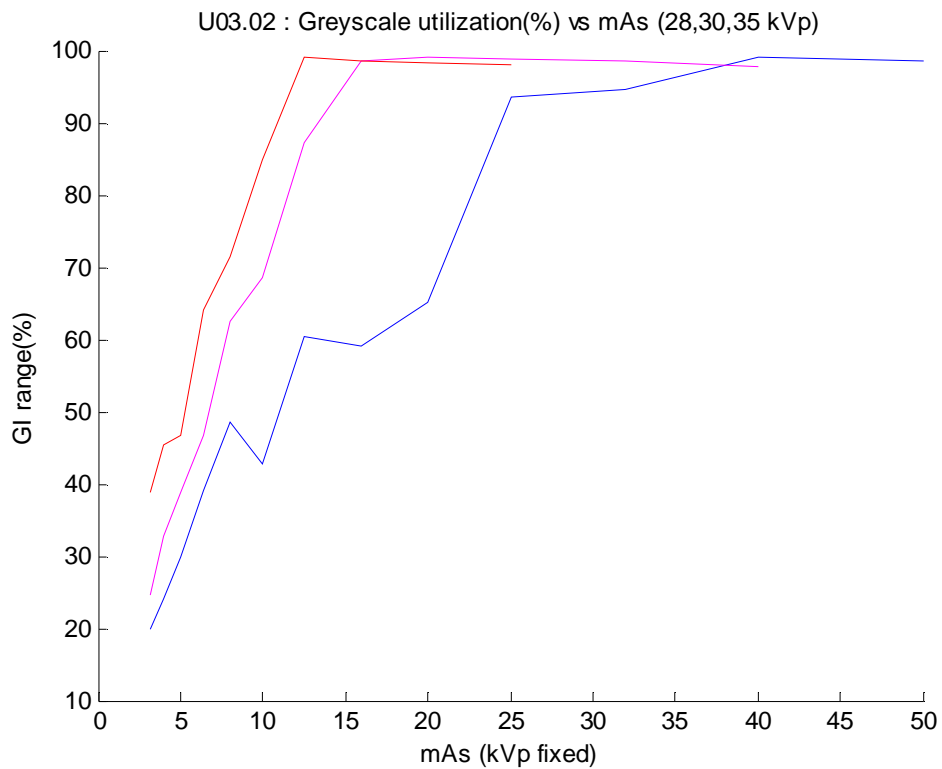


Figure 51: Greyscale utilization(%) estimation against mAs (kVp: 28,30,35), for image set "U03.02".

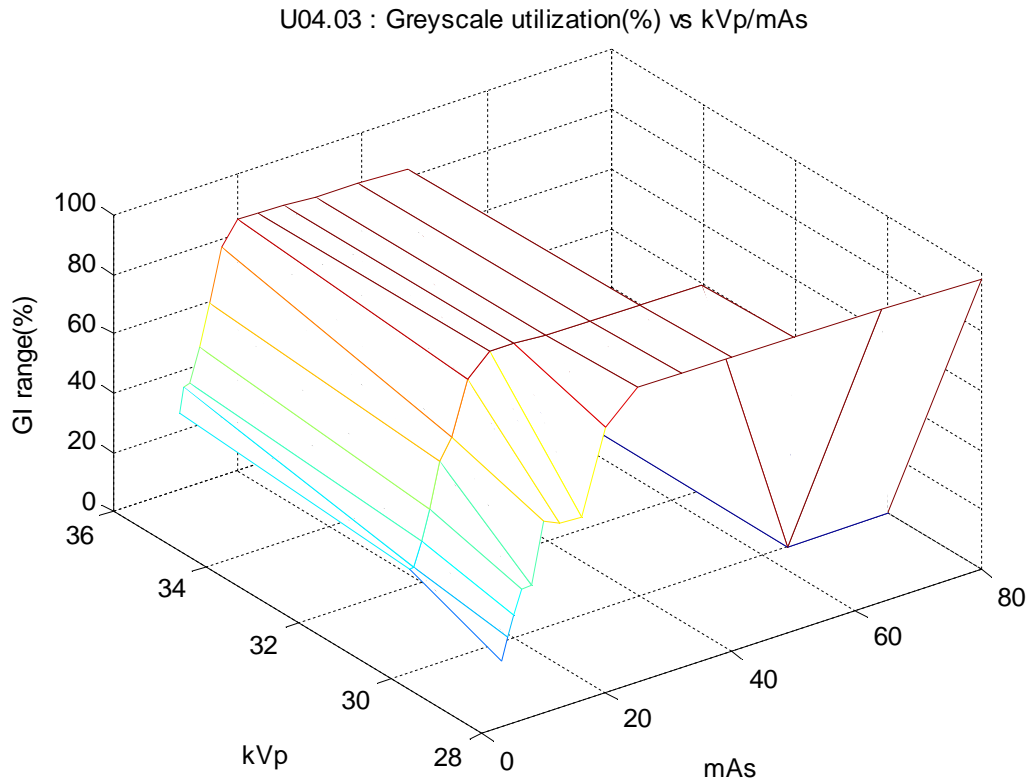


Figure 52: Greyscale utilization(%) estimation against kVp and mAs, for image set "U04.03".

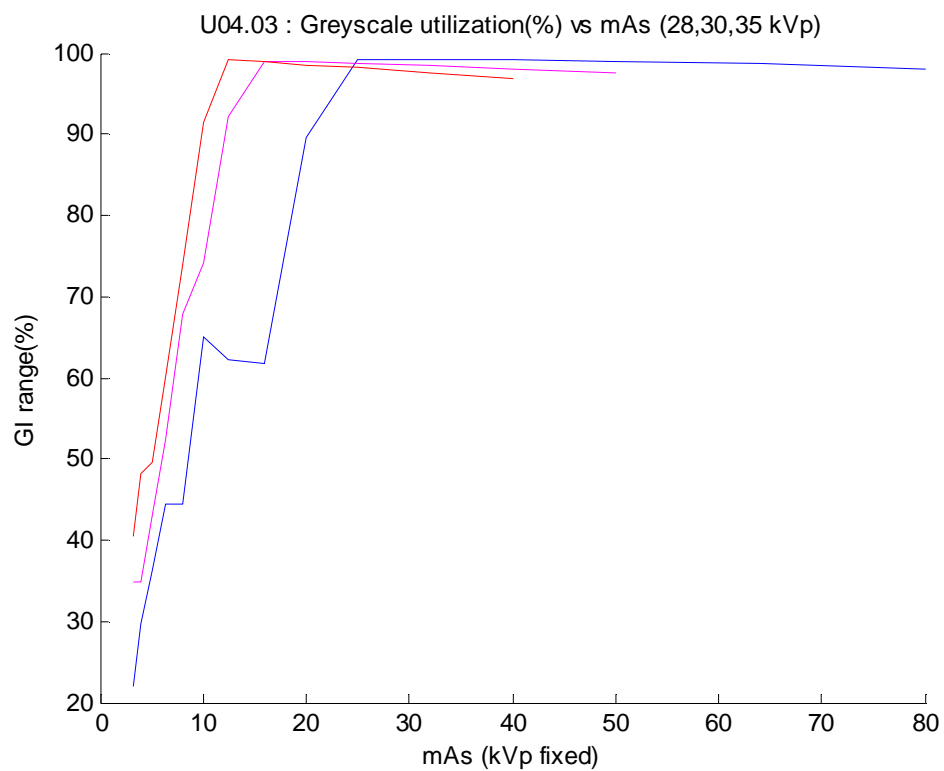


Figure 53: Greyscale utilization(%) estimation against mAs (kVp: 28,30,35), for image set "U04.03".

Figures 46-49 present the estimated RMS(%) noise calculated for images sets "U03.02" and "U04.03", for all the available settings of kVp and mAs. As the graphs show, the noise rises in a steep logarithmic momentum until a specific limit, where it drops almost instantly to zero (due to the excessive saturation of the detector). Higher settings for kVp tend to produce, higher, almost linear positive slopes, however the main factor for the noise power remains mAs. These results verify the initial assertion that noise should be considered as an important factor when increasing kVp and/or mAs in order to produce images of higher contrast, regardless of the corresponding patient's dose limitations.

Figures 50-53 demonstrate the utilization of the active greyscale range against kVp and mAs settings. Active greyscale is calculated by setting the minimum (black) to the mean value of saturated homogeneous areas and the maximum (white) to the mean value of unexposed areas. Although the full available range is always 12-bit (0...4095), excessively low exposure rates produce a limited usable range for the produced image, while excessively high exposure rates tend to saturate the whole imaging area, including the projection of the tissue. Optimal exposure rates are the ones that combine high utilization(%) of the available greyscale, while at the same time maintain normal dose and saturation characteristics within the tissue areas. Similar measurements can be easily embedded in the line-scanning procedure in order to track both the full (global) and the intra-tissue (local) utilization of the available 12-bit greyscale.

2.8.3 Texture "signatures" against exposure rates

Similarly to the feature analysis already conducted for the simulated images of DB1 and DB2 by using PredModel-1B, all the 20 prototype texture feature extractors were applied to the new DB3 database and the resulting feature datasets were analyzed in a similar way. As mentioned earlier, due to the nature and content of the new DB3 image sets, there is no information about the exact tissue orientation and location within the complete breast area. Therefore, analysis of the textural feature values was conducted using the complete sampling area as the base for comparing against different exposure rates. Furthermore, three different gamma correction values were employed as a basic step of (global) histogram pre-processing, namely 0.62 (darker), 1.00 (normal) and 1.60 (brighter), producing symmetric alterations of the overall illumination of the original image at $\pm 11.6\%$ respectively.

The efficiency of each feature function was evaluated for the same tissue and for different exposure rates, using single over the entire sampling area (instead of the full 2-D output) and for different gamma correction values. The resulting 2-D graphs contain the cumulative feature values over the entire sampling area, plotted against dose true measurement and gamma value. From the total of 500 combined graphs, Figures 54-73 present the complete set of results for all features calculated over the "U03.02" image set.

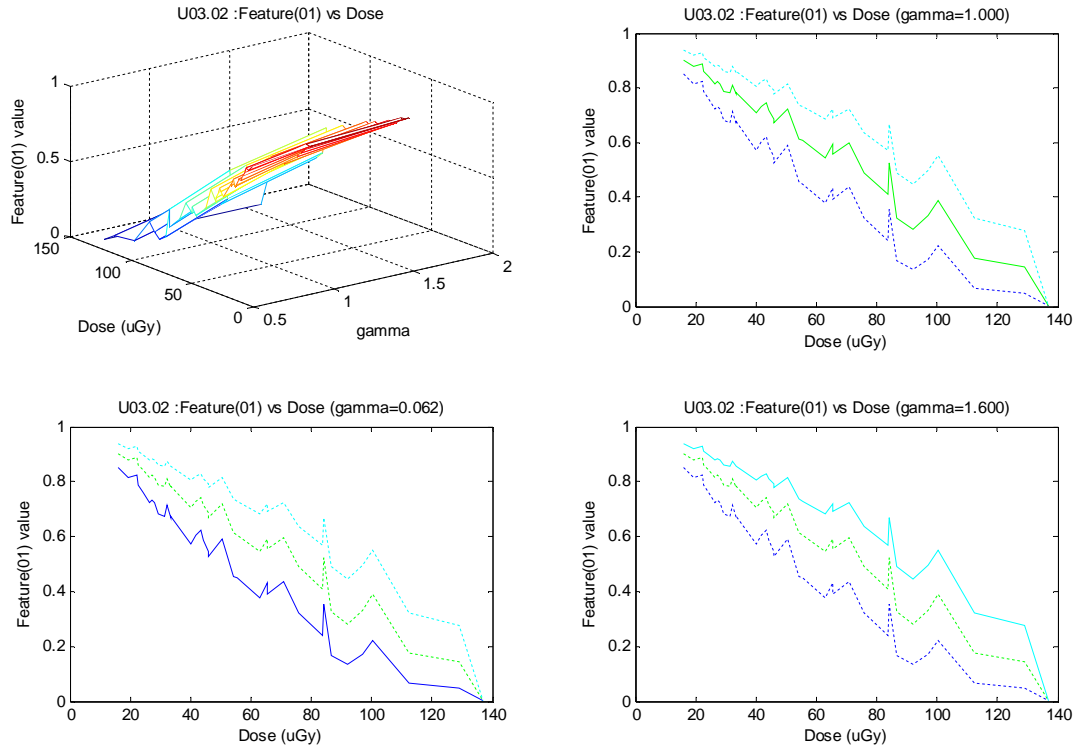


Figure 54: PredModel-2A/B, textural "signature" profile for MIN feature function at different exposure rates (dose) and gamma correction values.

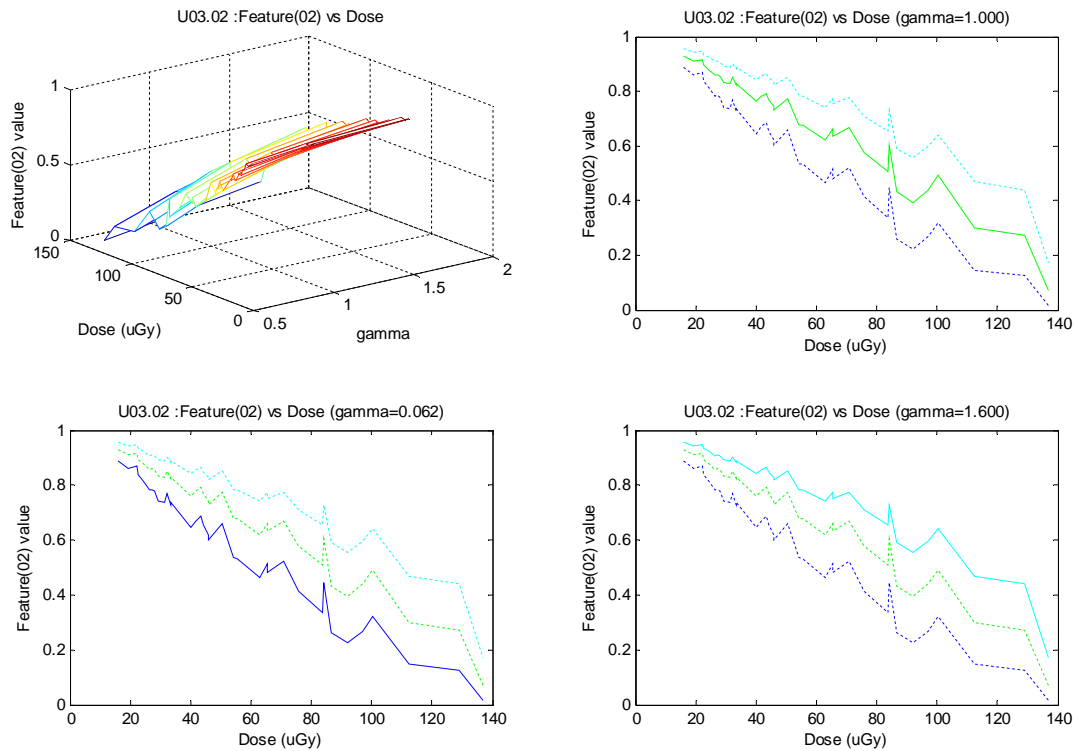


Figure 55: PredModel-2A/B, textural "signature" profile for MAX feature function at different exposure rates and gamma correction values.

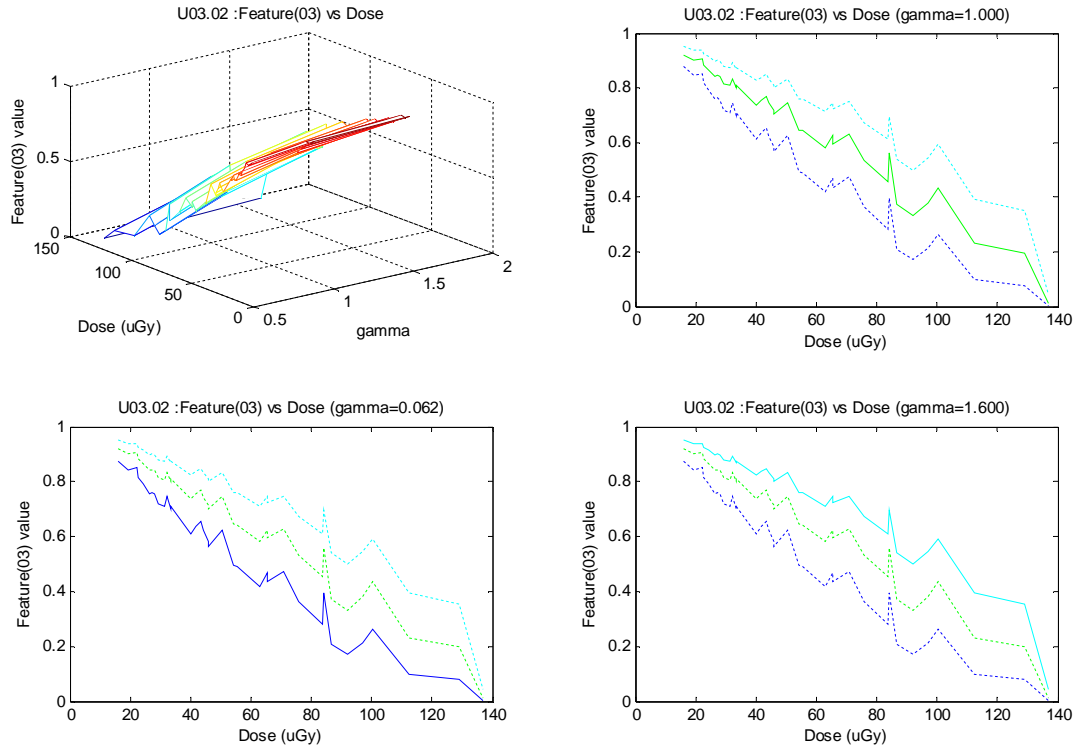


Figure 56: PredModel-2A/B, textural "signature" profile for MEAN feature function at different exposure rates (dose) and gamma correction values.

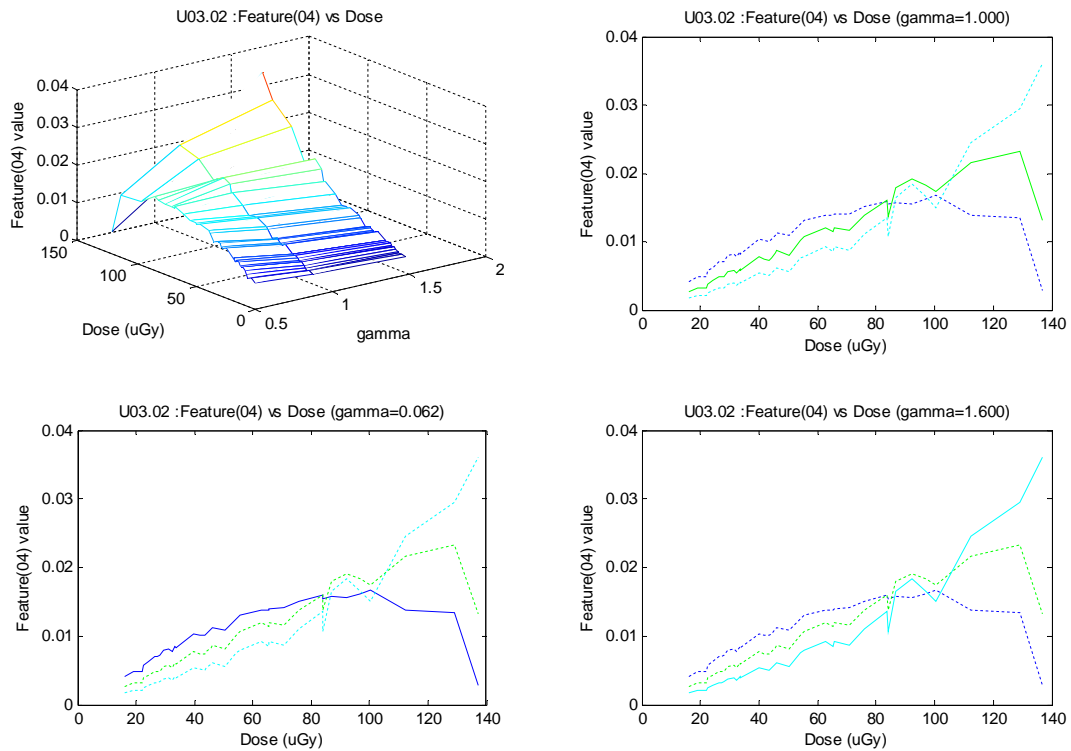


Figure 57: PredModel-2A/B, textural "signature" profile for STDEV feature function at different exposure rates (dose) and gamma correction values.

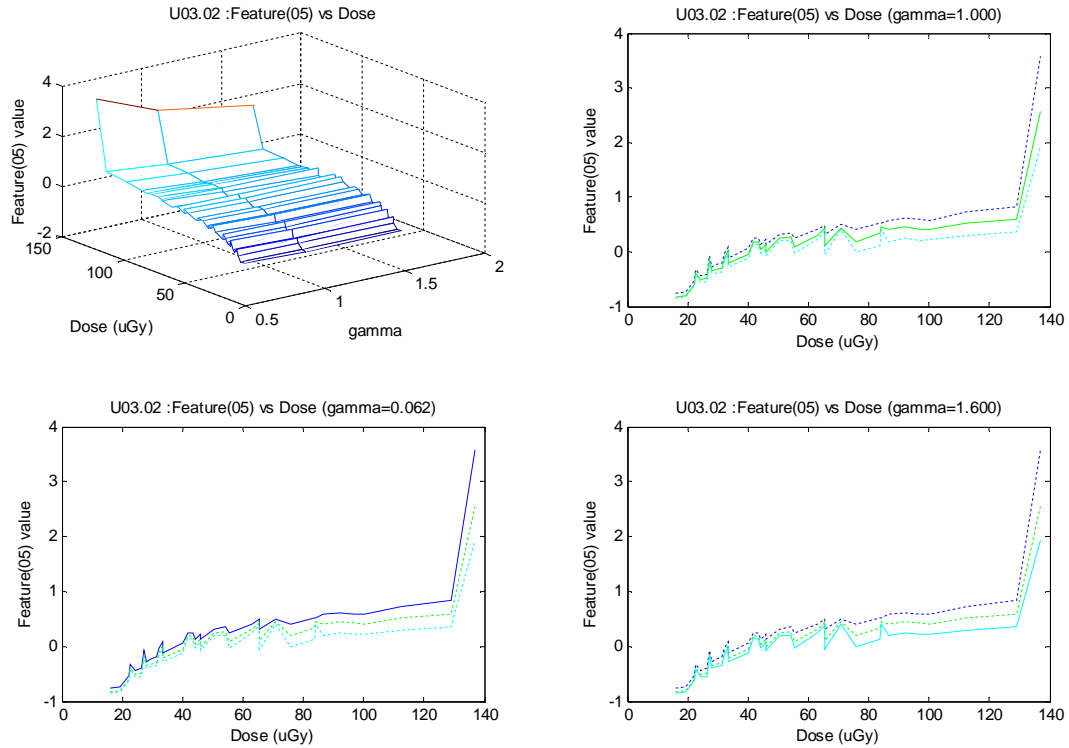


Figure 58: PredModel-2A/B, textural "signature" profile for SKEWNESS feature function at different exposure rates (dose) and gamma correction values.

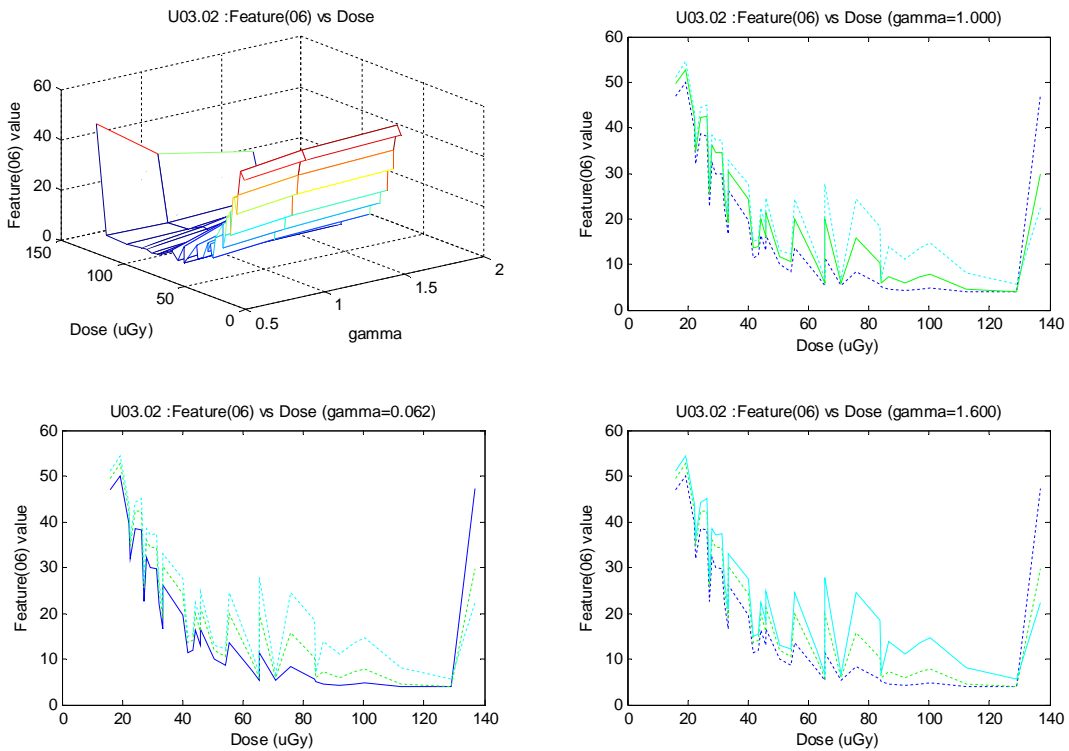


Figure 59: PredModel-2A/B, textural "signature" profile for KURTOSIS feature function at different exposure rates (dose) and gamma correction values.

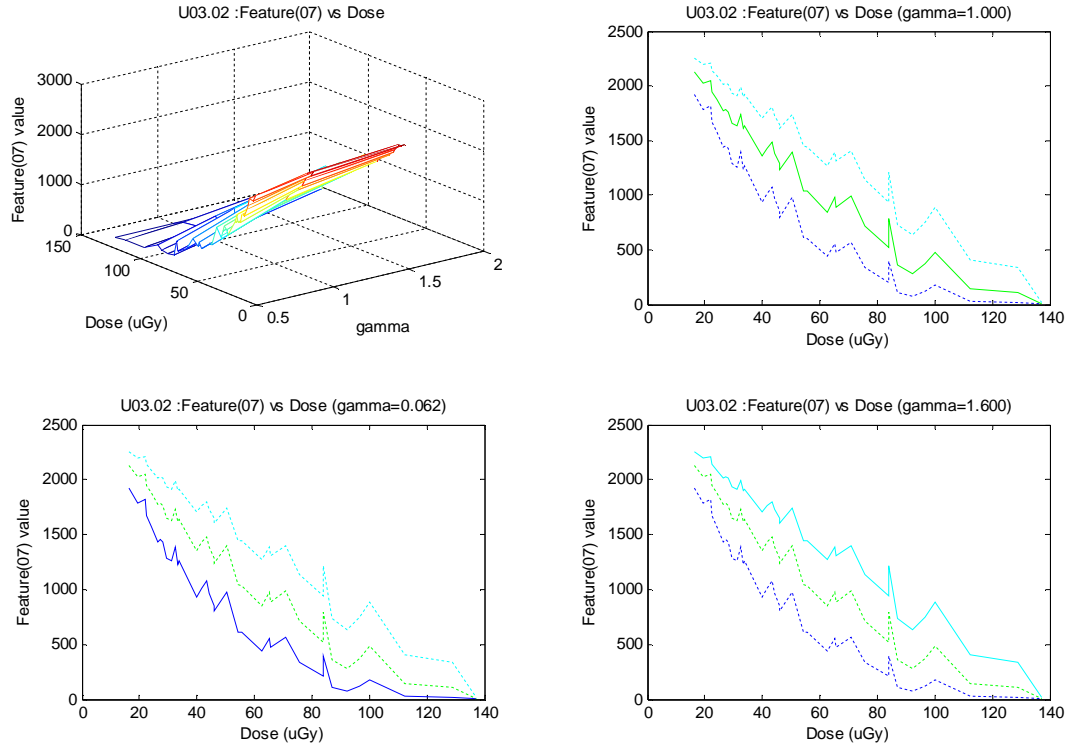


Figure 60: PredModel-2A/B, textural "signature" profile for POWER feature function at different exposure rates (dose) and gamma correction values.

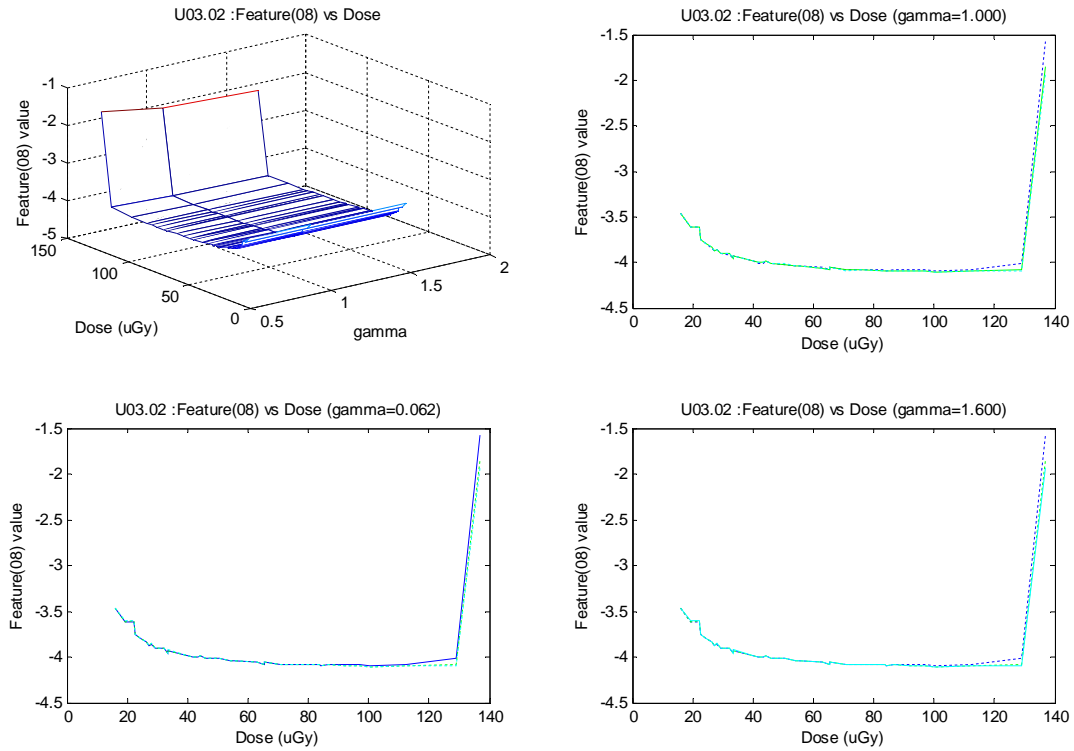


Figure 61: PredModel-2A/B, textural "signature" profile for ENTROPY feature function at different exposure rates (dose) and gamma correction values.

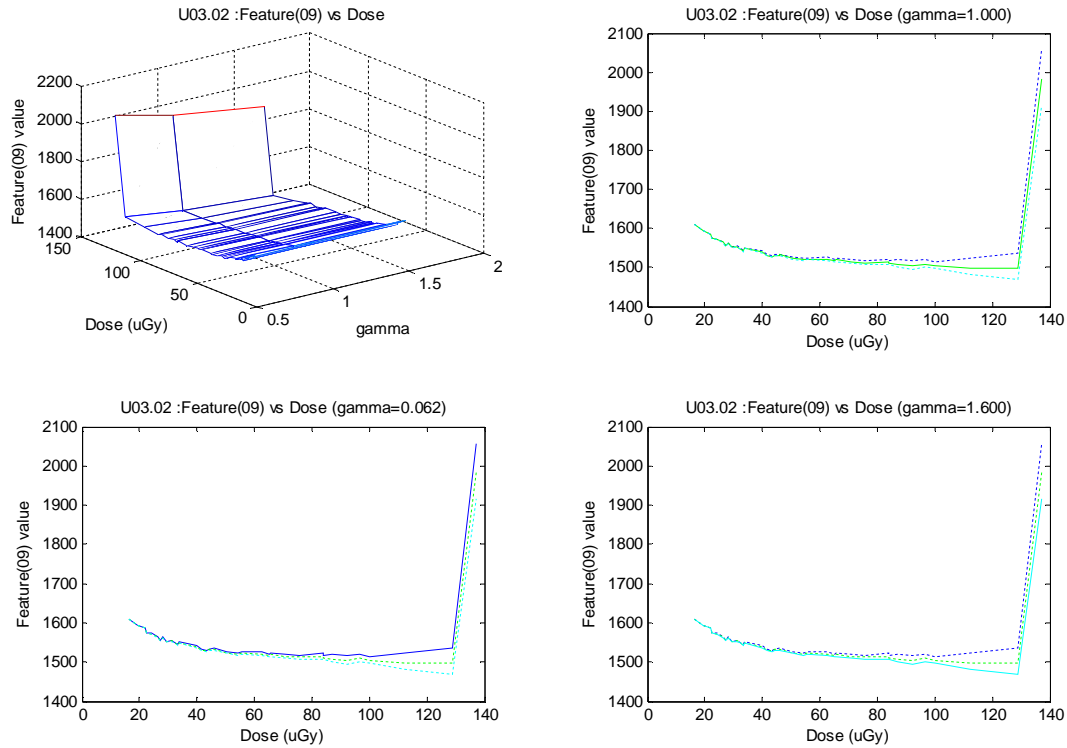


Figure 62: PredModel-2A/B, textural "signature" profile for ZCCOUNT feature function at different exposure rates (dose) and gamma correction values.

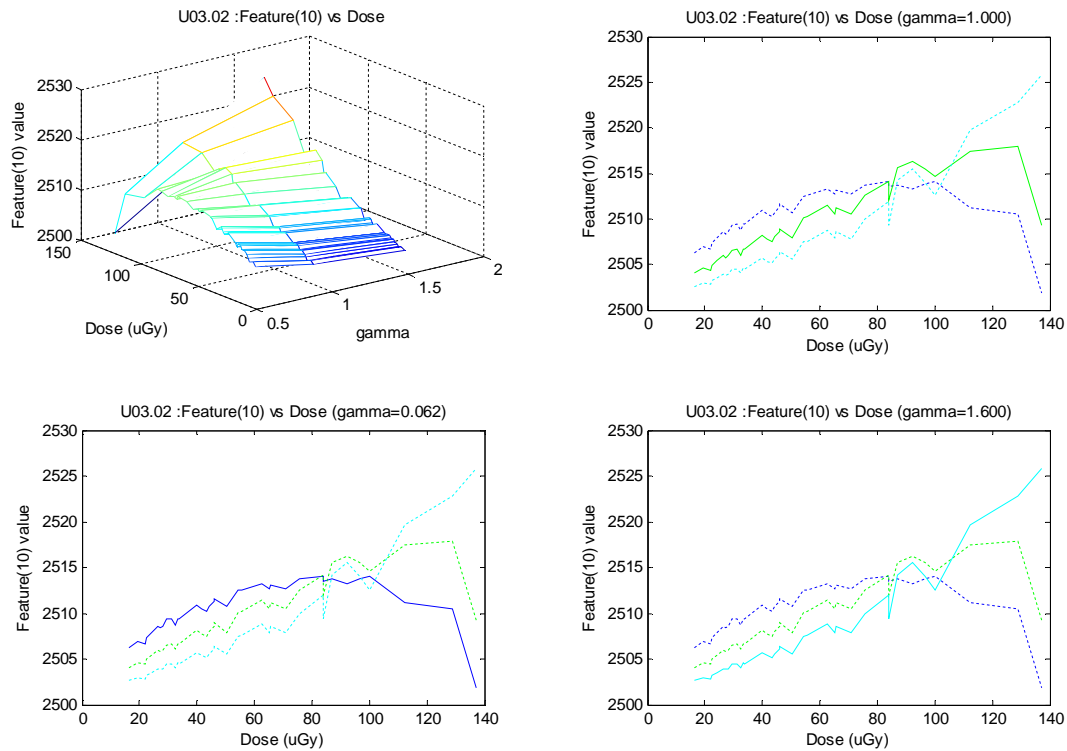


Figure 63: PredModel-2A/B, textural "signature" profile for SURFACE feature function at different exposure rates (dose) and gamma correction values.

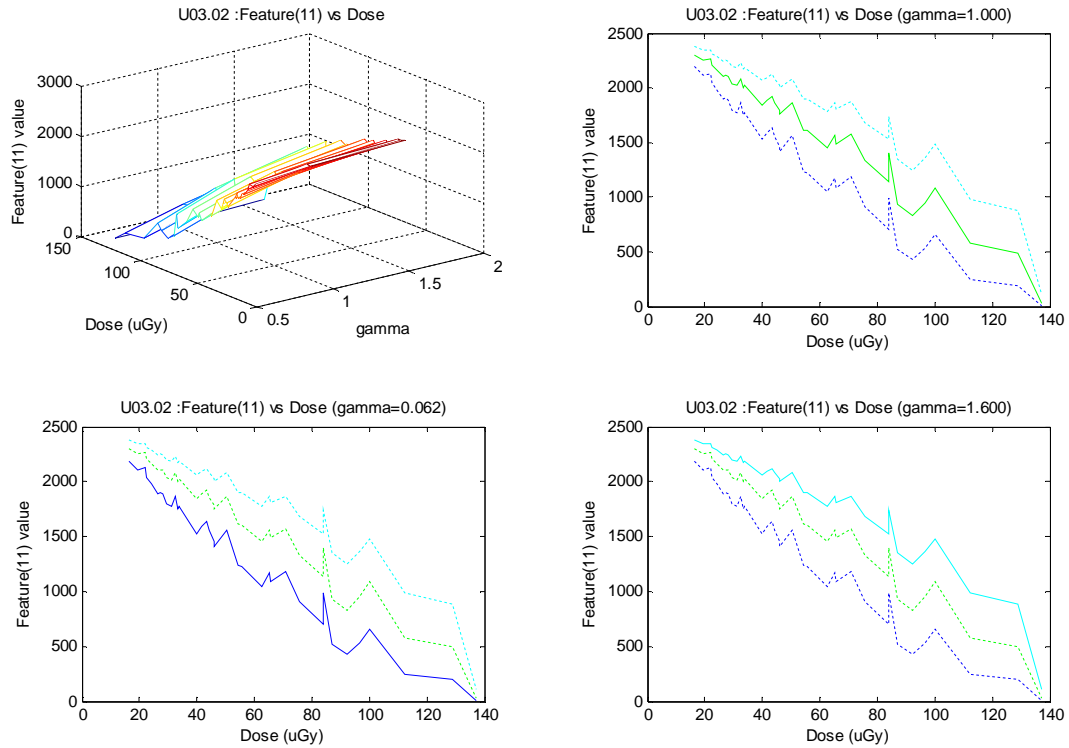


Figure 64: PredModel-2A/B, textural "signature" profile for VOLUME feature function at different exposure rates (dose) and gamma correction values.

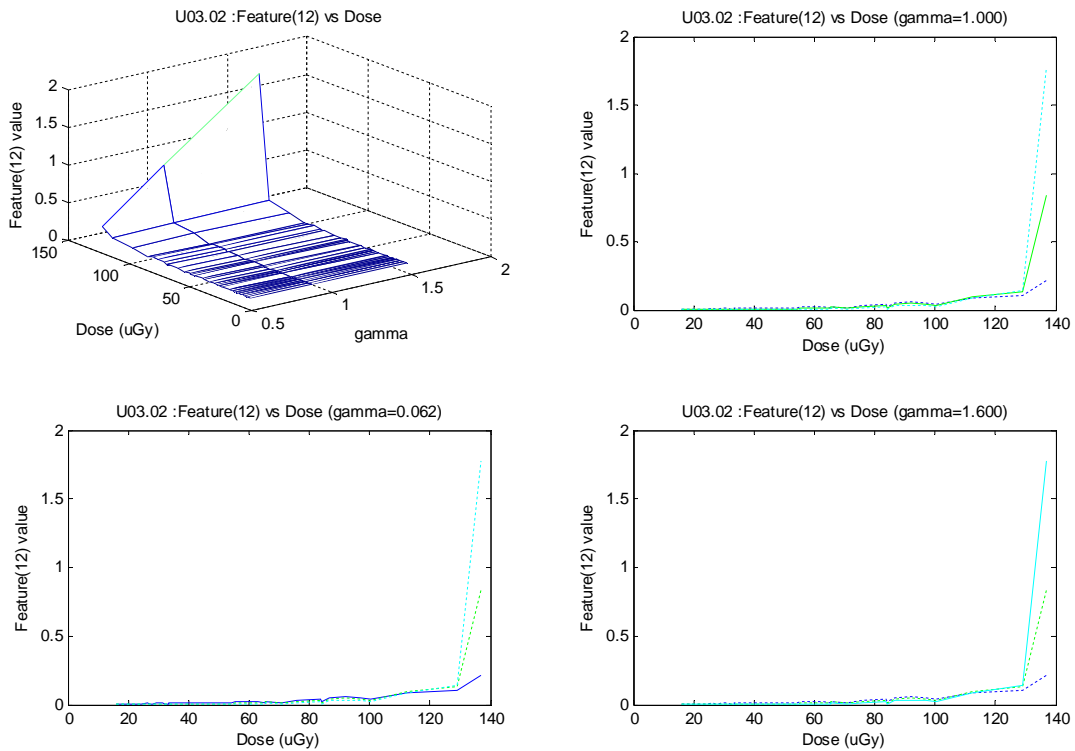


Figure 65: PredModel-2A/B, textural "signature" profile for SF12 feature function at different exposure rates (dose) and gamma correction values.

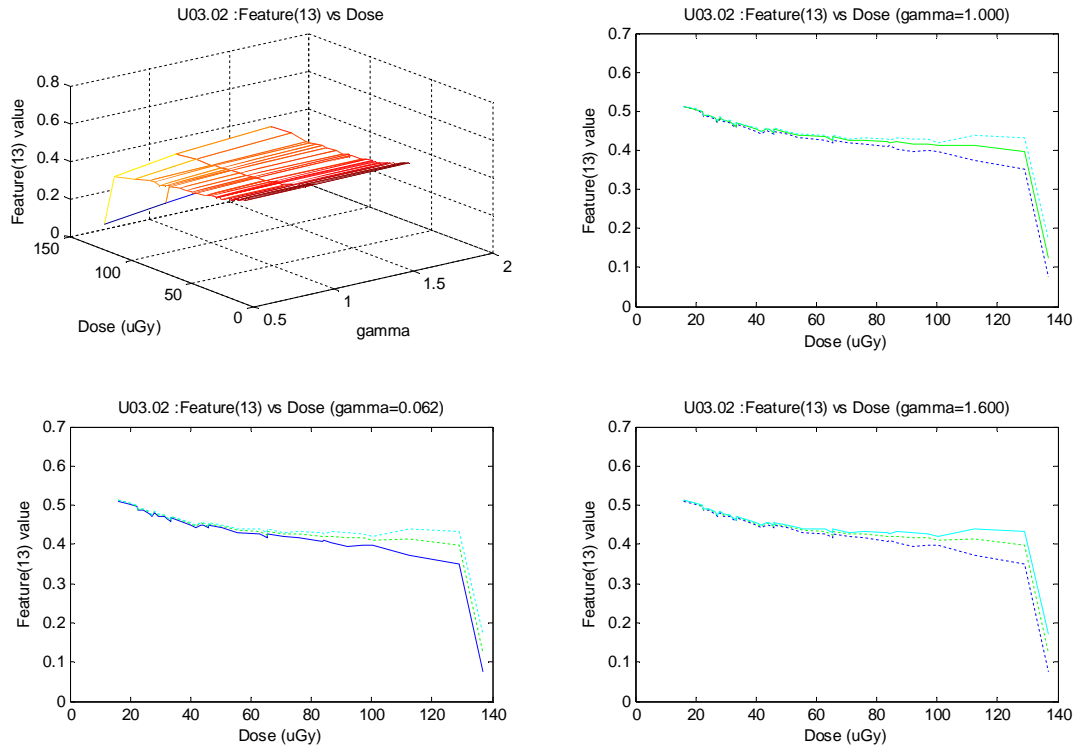


Figure 66: PredModel-2A/B, textural "signature" profile for SF13 feature function at different exposure rates (dose) and gamma correction values.

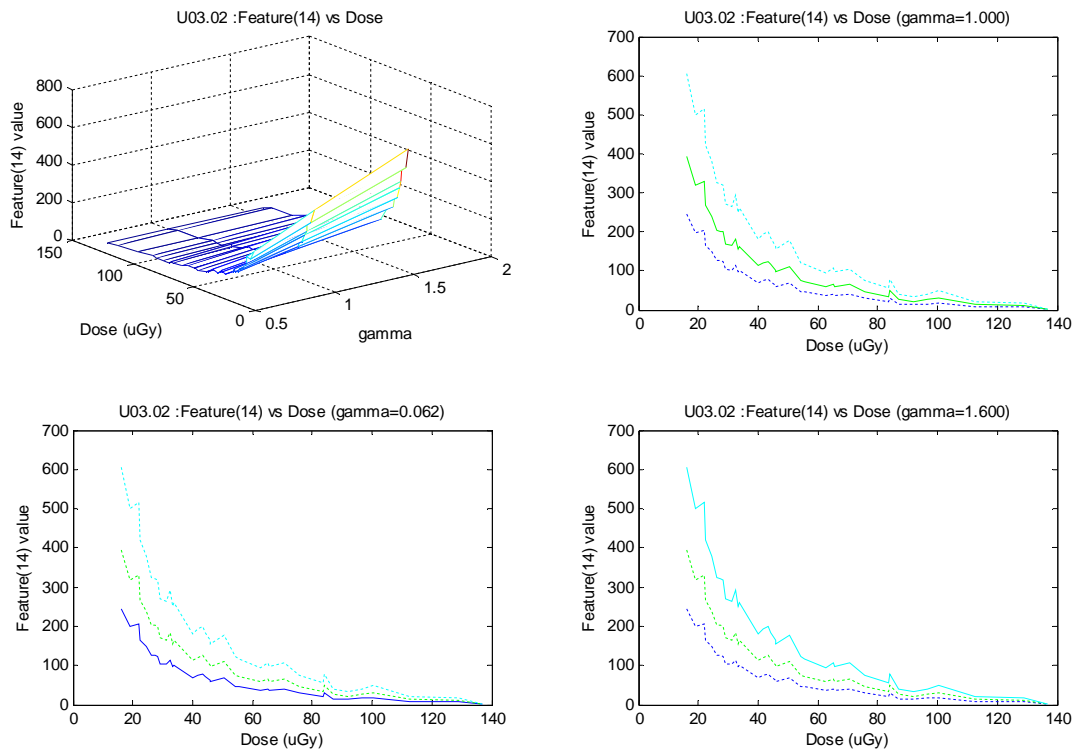


Figure 67: PredModel-2A/B, textural "signature" profile for SF14 feature function at different exposure rates (dose) and gamma correction values.

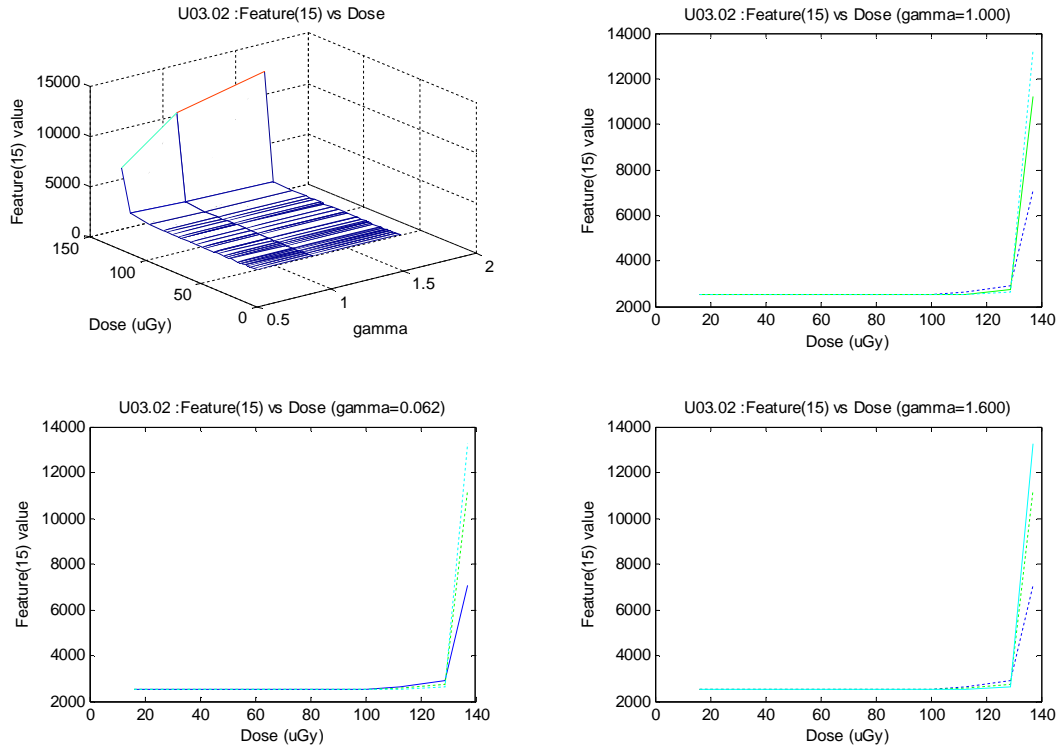


Figure 68: PredModel-2A/B, textural "signature" profile for SF15 feature function at different exposure rates (dose) and gamma correction values.

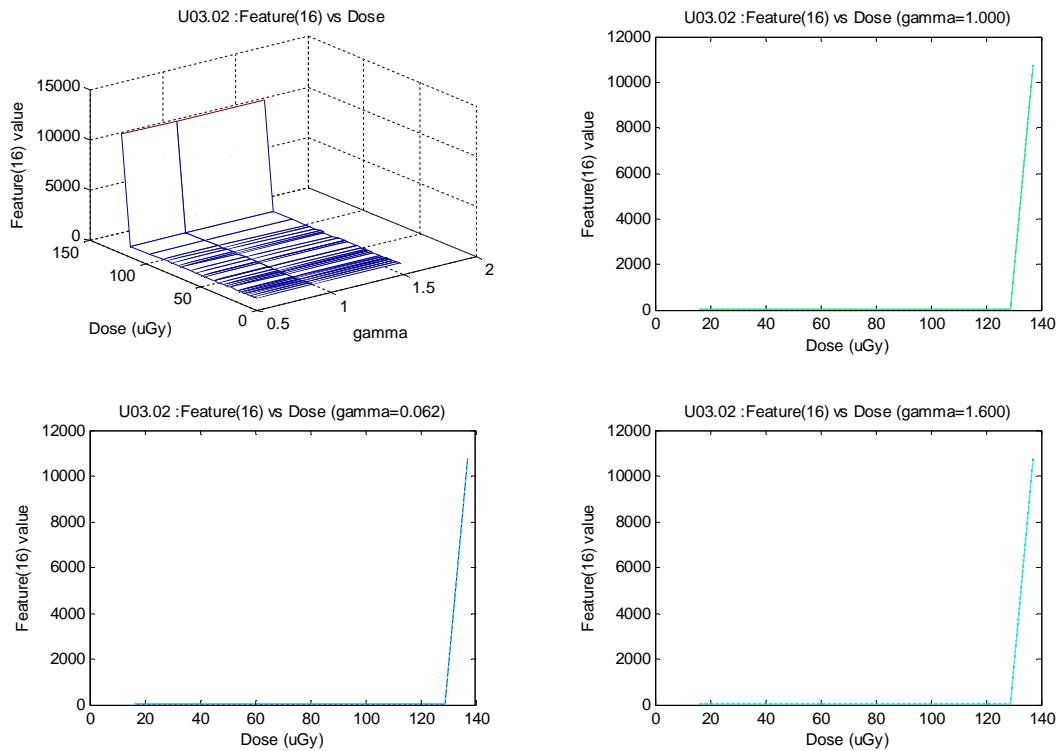


Figure 69: PredModel-2A/B, textural "signature" profile for SF16 feature function at different exposure rates (dose) and gamma correction values.

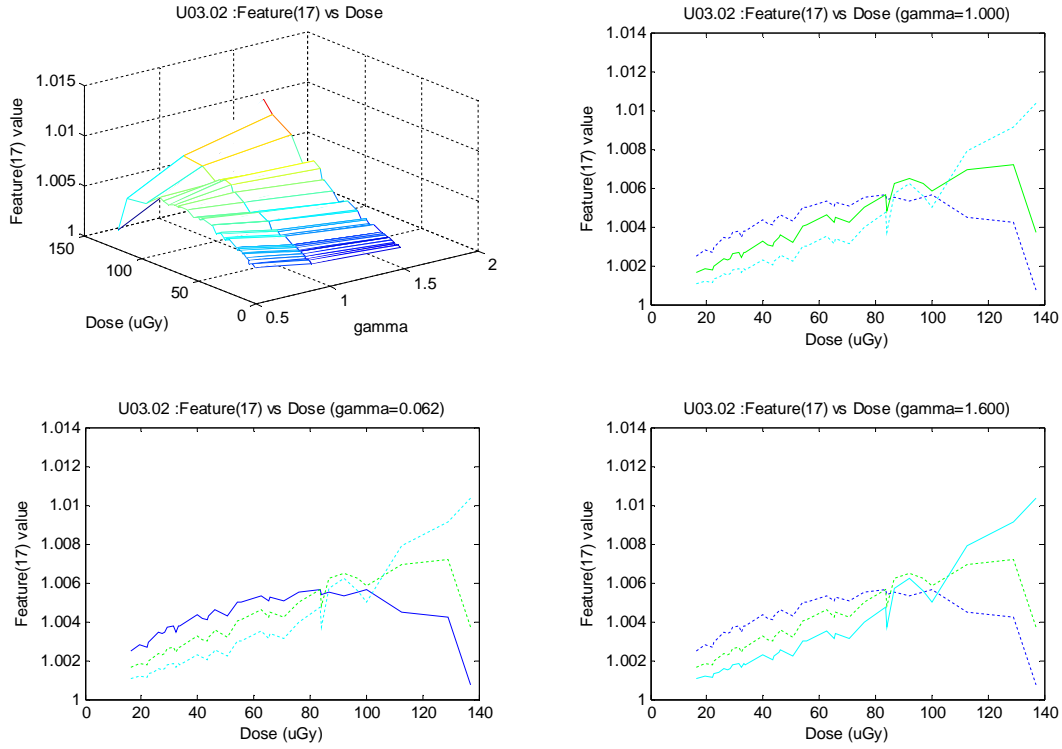


Figure 70: PredModel-2A/B, textural "signature" profile for SF17 feature function at different exposure rates (dose) and gamma correction values.

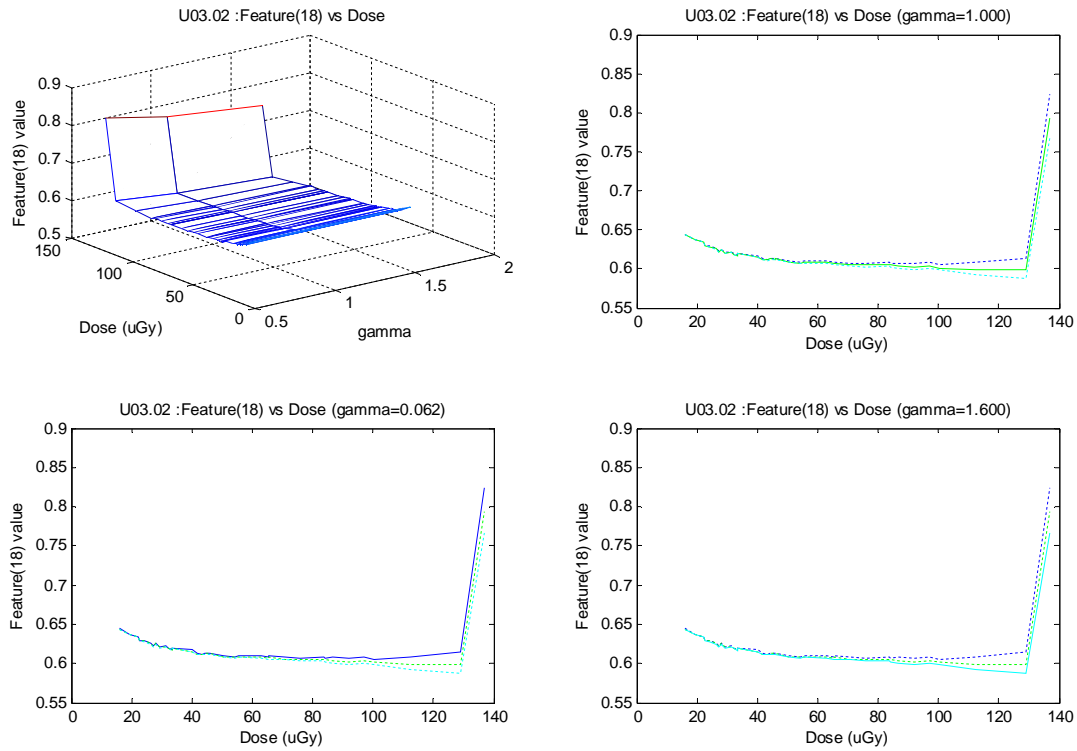


Figure 71: PredModel-2A/B, textural "signature" profile for SF18 feature function at different exposure rates (dose) and gamma correction values.

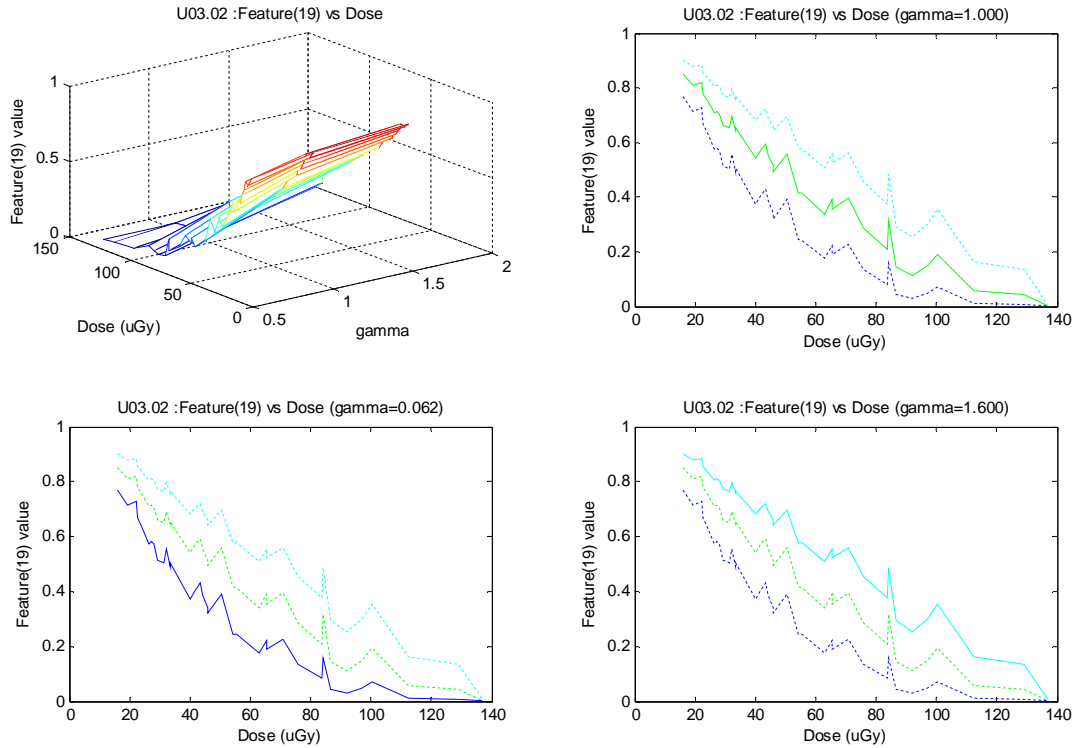


Figure 72: PredModel-2A/B, textural "signature" profile for SF19 feature function at different exposure rates (dose) and gamma correction values.

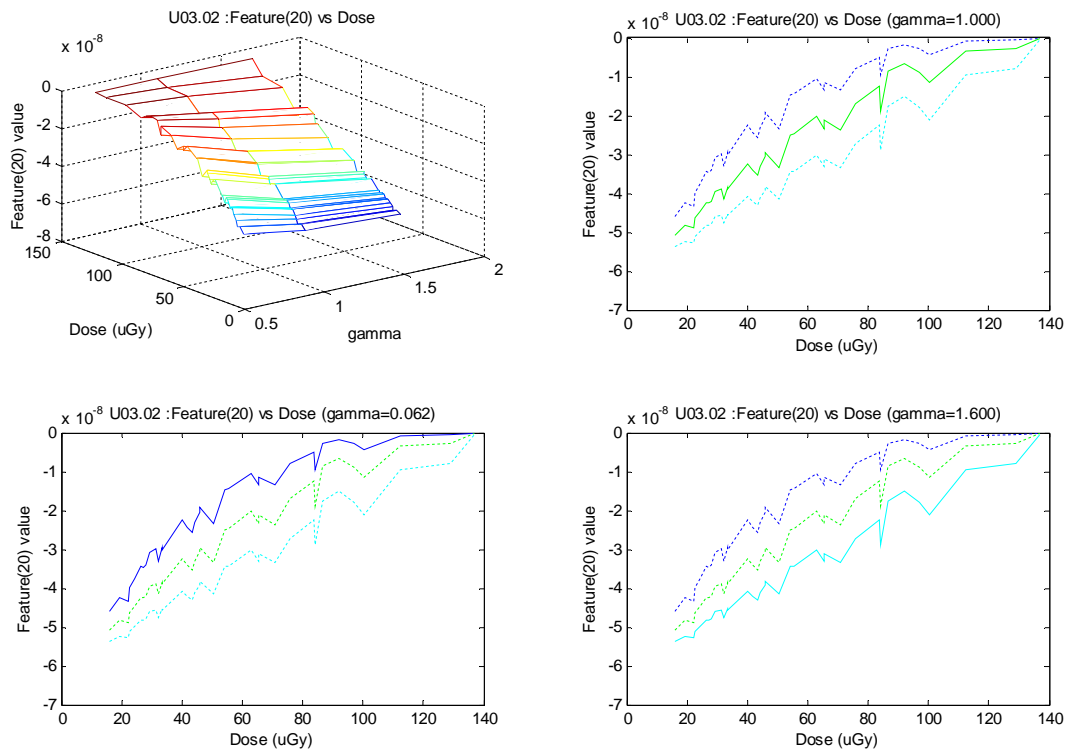


Figure 73: PredModel-2A/B, textural "signature" profile for SF20 feature function at different exposure rates (dose) and gamma correction values.

The feature functions were assessed in terms of resolution, stability and smoothness of response curves against the available range of measured dose. Similarly to the analysis conducted by PredModel-1B, the PredModel-2A/B investigated the statistical properties of each of the 20 feature functions, applied for each image set separately and then combined for the final assessments. In order to relate these plots to the ones generated by PredModel-1B (Figures 17-38), "image scanning column" property should be considered as fixed, i.e. for a specific "snapshot" during the line-scanning procedure. For example, the SF20 function 2-D plots in Figures 36-38 and the corresponding 1-D plot of Figure 73 demonstrate a similar, logarithmic-like, transition curve, when a single scanning column is considered in the 2-D plots. Therefore, it is clear that the response curves already calculated for the simulated image sets (DB1 and DB2) and the corresponding curves calculated over the new image sets (DB3) display similar functional and statistical characteristics.

From the results presented in the previous plots, it can be easily verified that feature functions already identified as "good" candidates for textural content recognition work equally well for the new DB3 image set. Functions MIN, MAX, MEAN, POWER, VOLUME and SF19 have shown a similar, exponentially decreasing, response curve when measured against various doses. Function SF20 demonstrates a similar behavior, only in this case the response curve is a standard logarithmic plot.

Function STDEV has already been identified as best fit for tissue recognition against the background, but with limited value over the intra-tissue areas. This property can be recognized when reviewing Figure 57. However, if various gamma correction levels ($\gamma=0.62$) are also considered, the same function demonstrates a characteristic window-like response curve. This type of transitions could be extremely useful when trying to match an expert's quality evaluation, where the optimal exposure settings can be found somewhere between excessively low and excessively high exposure rates. Similar response curves can be identified also for feature functions SURFACE (Figure 63) and SF17 (Figure 70). Finally, feature function SF14 (Figure 67) seem to have a response curve similar to the initial selection of seven feature functions, however, the transition plot drops rapidly towards zero and remains almost constant for the most part of the dose range.

With respect to pre-processing, gamma correction over the full greyscale range seems to have had limited to no effect in the response curve. Almost in all cases, the effects of using symmetric gamma correction levels below (0.62) and above (1.60) the nominal value (1.00) was the introduction of a positive or negative shift of the transition plot in the form of Y-axis bias. As an exception, functions STDEV, SURFACE and SF17 demonstrated an explicit behavior of transforming the initial exponential-like curve into a window-like curve when using gamma levels below nominal. In general, the introduction of gamma correction as a pre-processing stage before the actual textural feature calculations have shown stable and consistent behavior in all cases, without any affect on the base statistics of the raw data and, in some cases, evidence of enhancing the information content of specific, otherwise irrelevant, features. Due to the nature and sensitivity of the design of the line-scanning control loop, the extent of similar pre-processing stages is to be considered later on.

2.8.4 Effects of special areas and background artifacts

For completeness purposes, two additional cases of data analysis were considered. Specifically, a clearly defined area of malignant mass in tissue “U01” (Figure 40, red area) was considered separately for full texture analysis, in order to assess the statistical differences in feature values against the normal tissue analysis thus far. Additionally, textural analysis was also conducted in specific areas of image sets “U03.02” and “U04.03” (Figure 40, blue areas), in order to investigate the statistical properties of the evaluated textural features when only the implicit background (perspex layers and tissue plastic wrapping) is considered.

For the malignant mass analysis, the full set of 20 textural feature dataset was calculated and the analysis was conducted in accordance to the one applied for the normal tissue areas. From the full set of 80 graphs, only 8 combined plots, the ones corresponding to the selected 8 features, are presented in Figures 74-81.

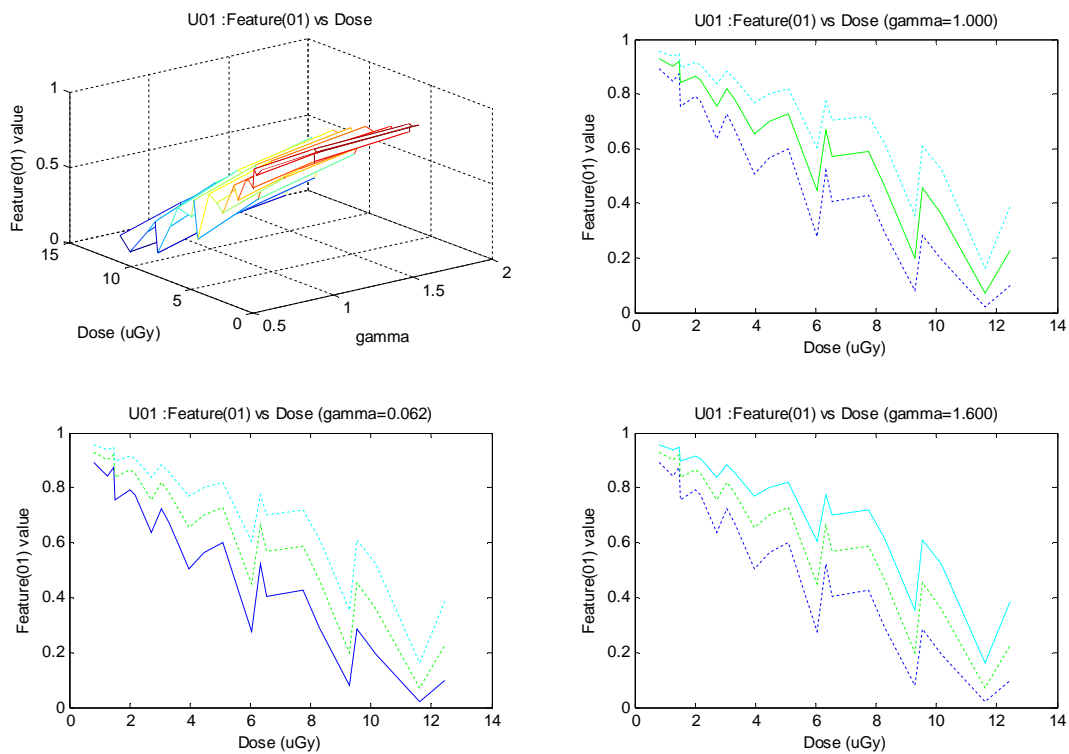


Figure 74: PredModel-2A/B, textural “signature” profile for MIN feature function at different exposure rates (dose) and gamma correction values, for the malignant tumor area.

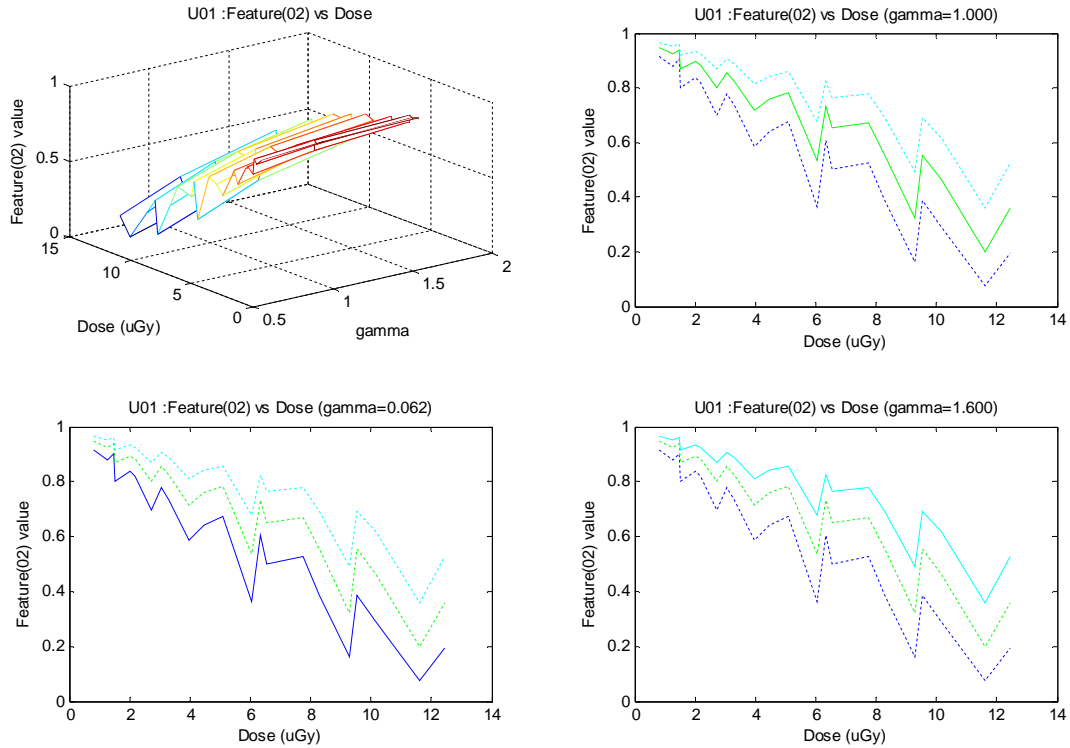


Figure 75: PredModel-2A/B, textural “signature” profile for MAX feature function at different exposure rates (dose) and gamma correction values, for the malignant tumor area.

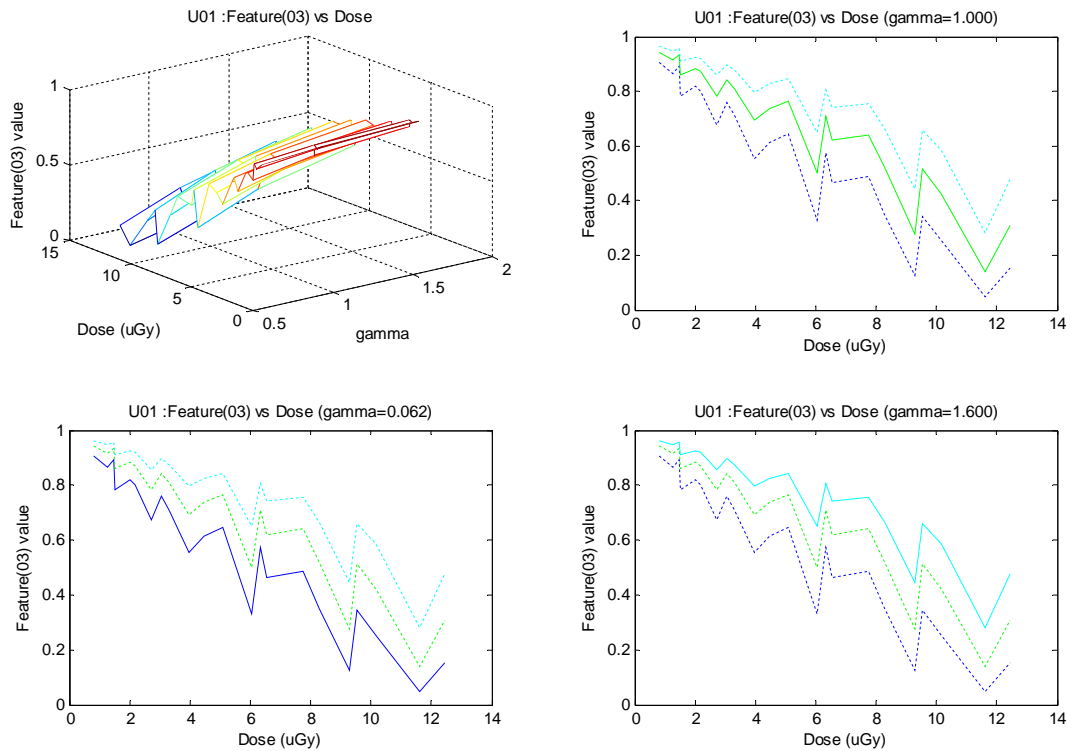


Figure 76: PredModel-2A/B, textural “signature” profile for MEAN feature function at different exposure rates (dose) and gamma correction values, for the malignant tumor area.

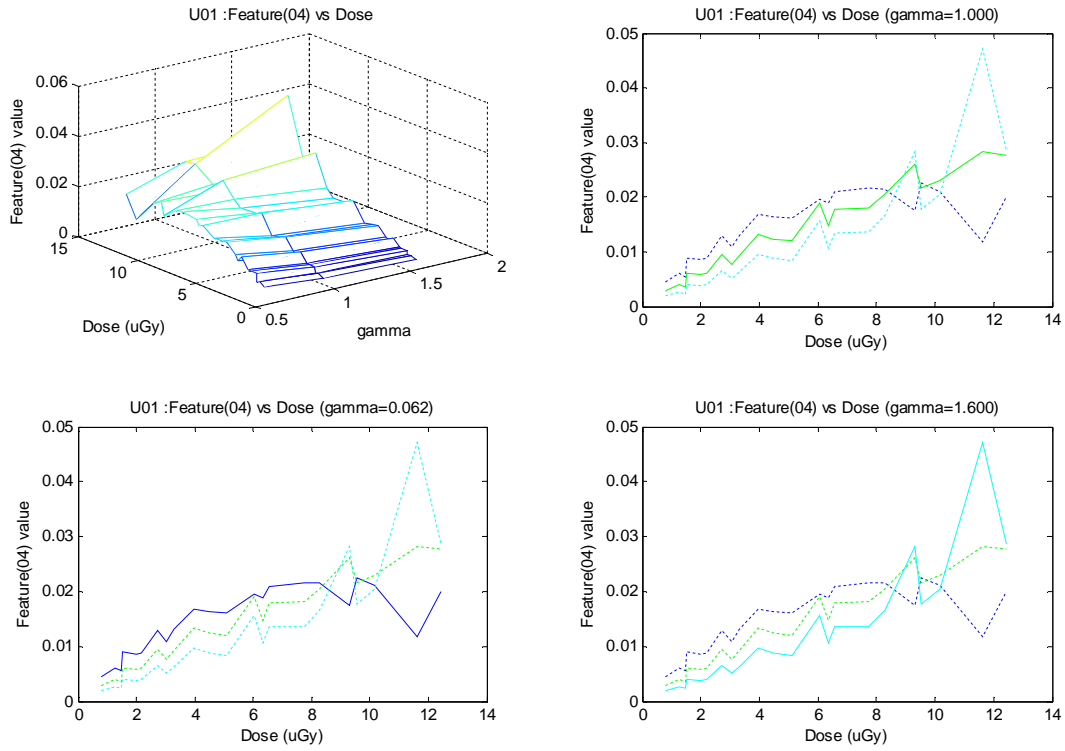


Figure 77: PredModel-2A/B, textural "signature" profile for STDEV feature function at different exposure rates (dose) and gamma correction values, for the malignant tumor area.

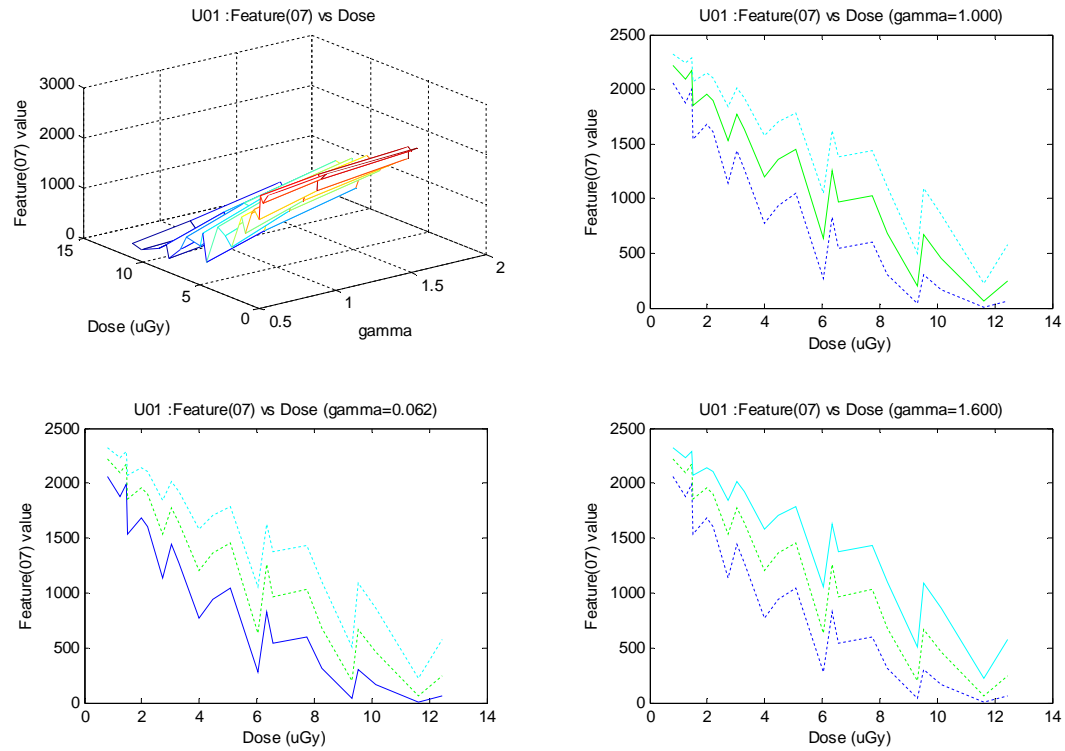


Figure 78: PredModel-2A/B, textural "signature" profile for POWER feature function at different exposure rates (dose) and gamma correction values, for the malignant tumor area.

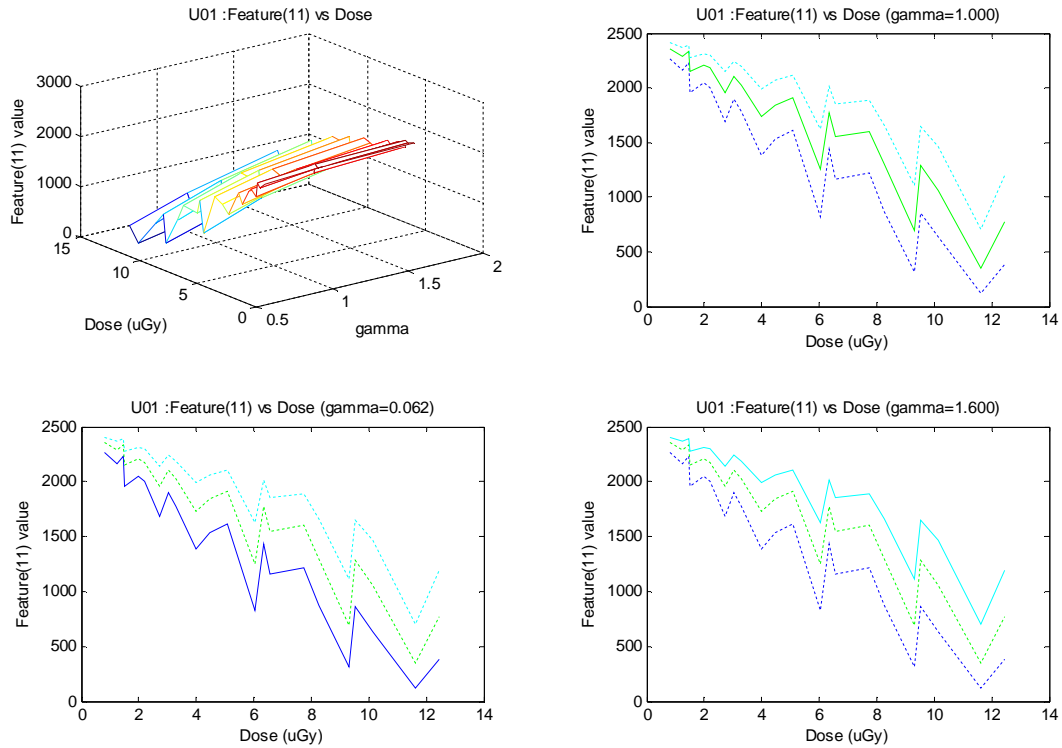


Figure 79: PredModel-2A/B, textural "signature" profile for VOLUME feature function at different exposure rates (dose) and gamma correction values, for the malignant tumor area.

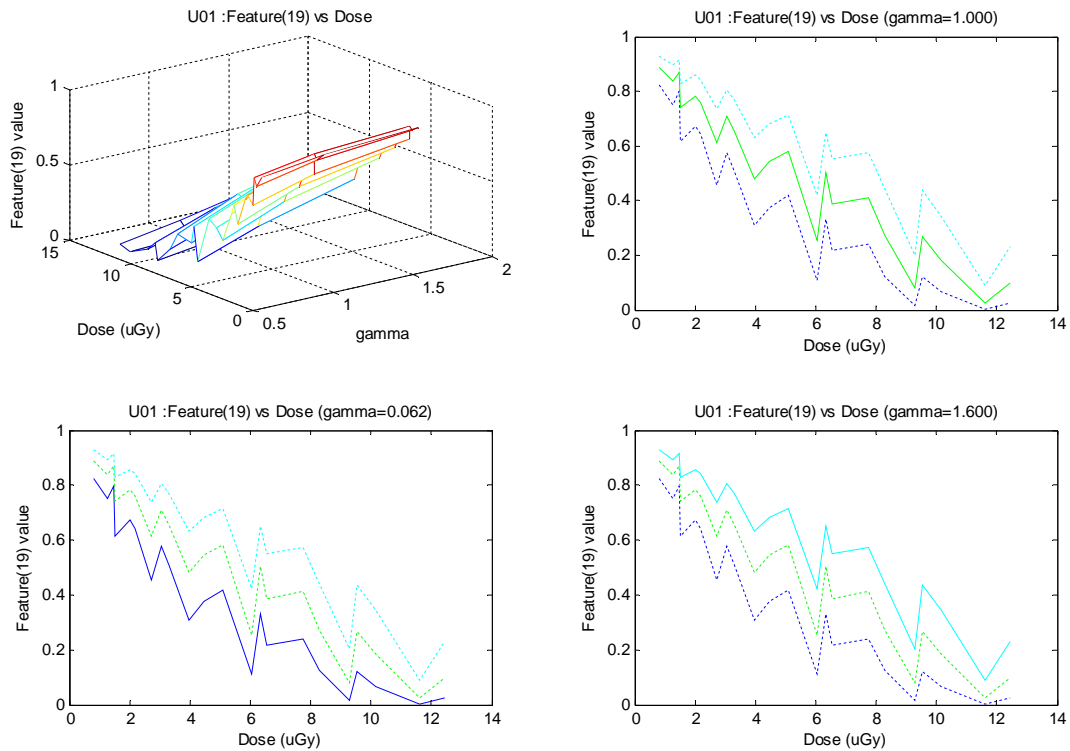


Figure 80: PredModel-2A/B, textural "signature" profile for SF19 feature function at different exposure rates (dose) and gamma correction values, for the malignant tumor area.

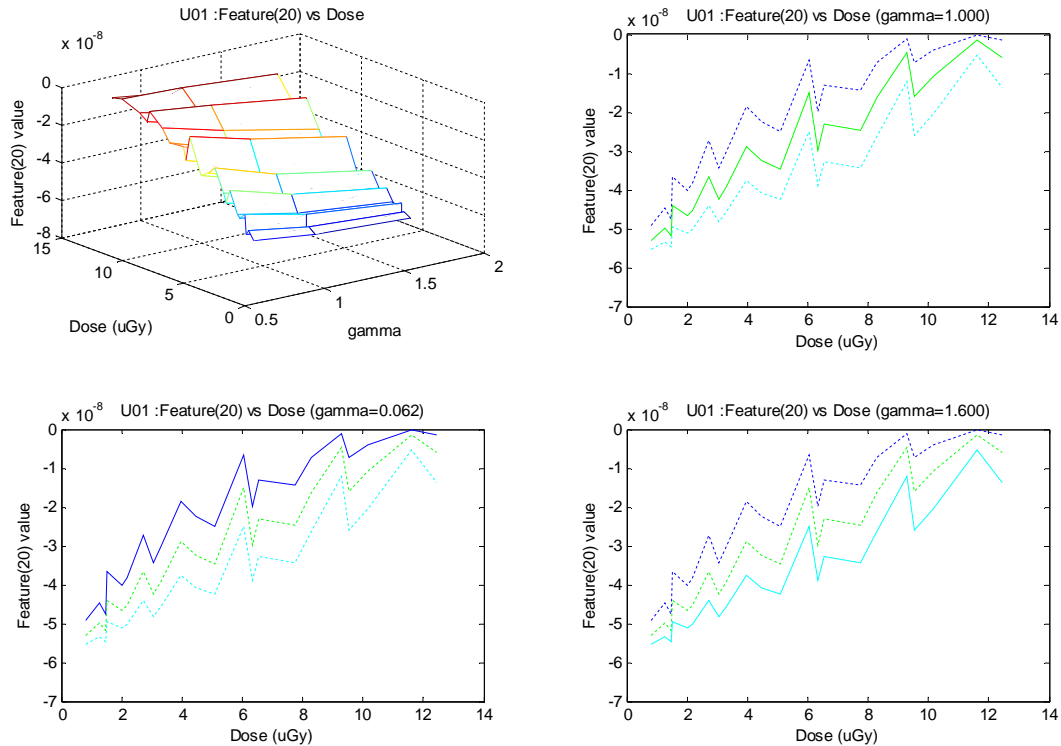


Figure 81: PredModel-2A/B, textural "signature" profile for SF20 feature function at different exposure rates (dose) and gamma correction values, for the malignant tumor area.

As expected, the general form of the transition curve for the malignant tissue is roughly the same as for the normal tissue, while the statistics related to power and elevation volume characteristics (features: POWER, VOLUME, SF19, SF20) are slightly higher in absolute value due to the overall increased mean value of brightness. The relatively consistent behavior of these textural feature extractors over both normal and pathological tissue justifies their usage for stable image quality estimator over the entire breast area. Internal structural details within the malignant tumor can be recognized in a similar way as for the normal tissue areas, even if the increased overall brightness makes this task harder for the naked eye. However, there is no clear indication of direct correlation to the discrimination of pathological findings, related to malignant tumors, and these slight differences in statistics. This is a direct conclusion from the fact that the diagnostic task in mammography is usually too difficult and complex to be described by first-order statistics that all the current (20) feature functions employ.

Next, the full set of 20 textural feature dataset was calculated for the areas of background artifacts/patterns (Figure 40, blue areas) over the image sets "U03.02" and "U04.03", and the analysis was conducted in accordance to the one applied for the normal tissue areas. From the full set of 160 graphs, only 8 combined plots, the ones corresponding to the selected 8 features for image set "U03.02", are presented in Figures 82-89.

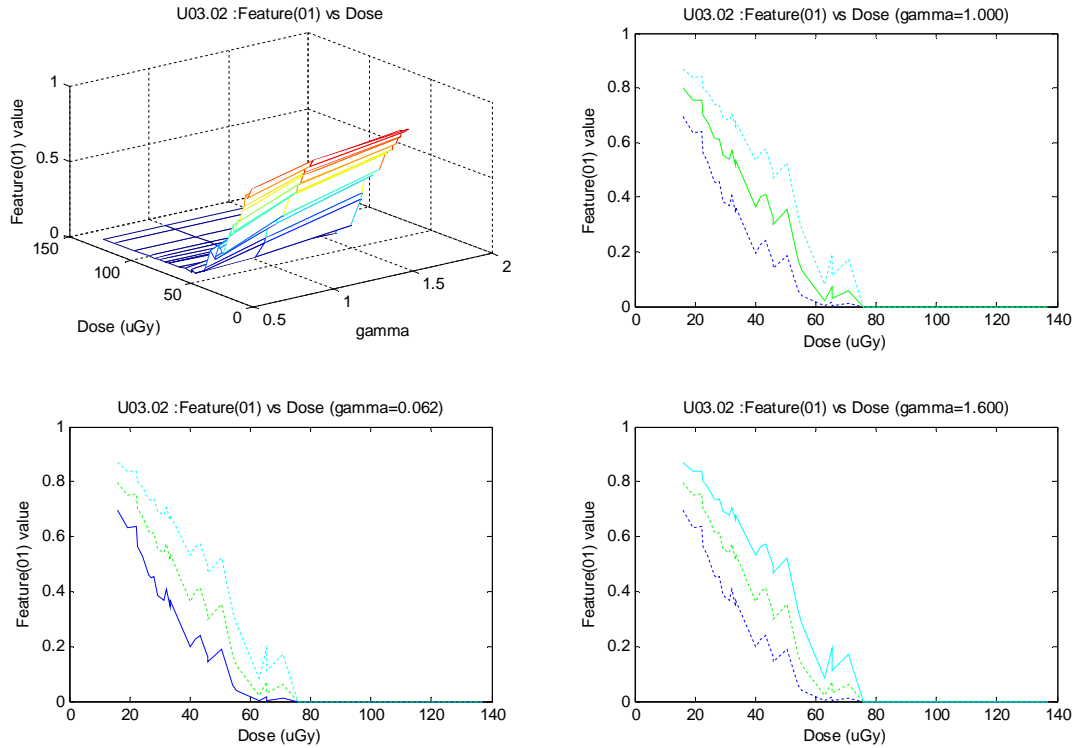


Figure 82: PredModel-2A/B, textural “signature” profile for MIN feature function at different exposure rates (dose) and gamma correction values, for the background area.

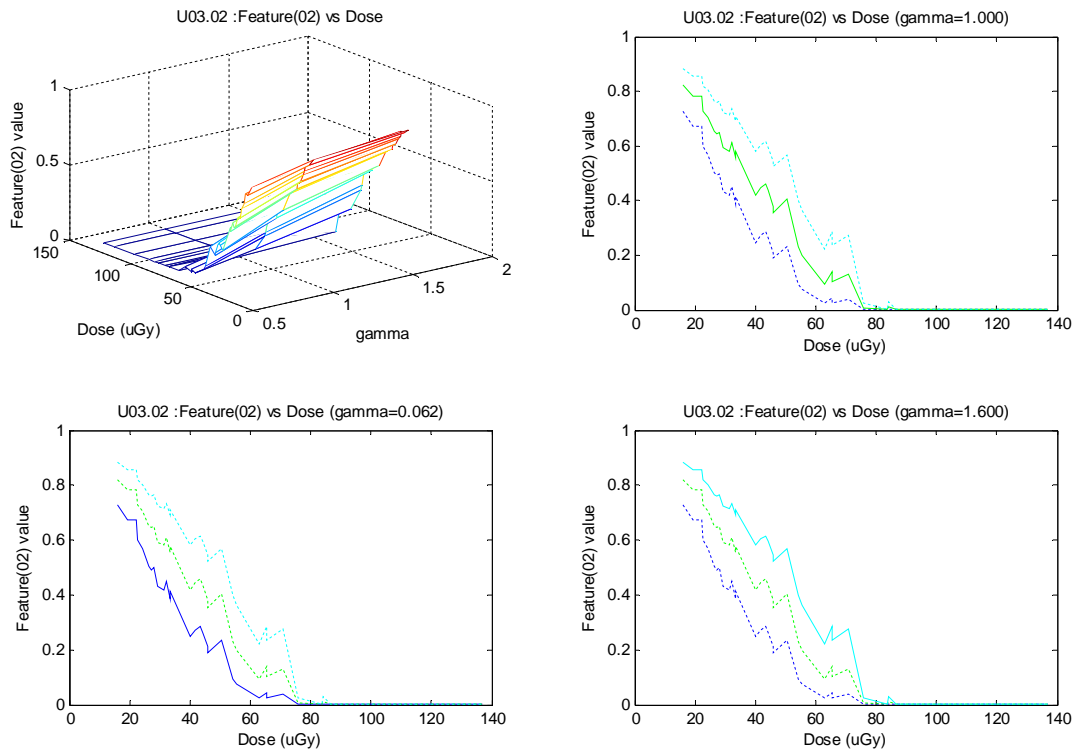


Figure 83: PredModel-2A/B, textural “signature” profile for MAX feature function at different exposure rates (dose) and gamma correction values, for the background area.

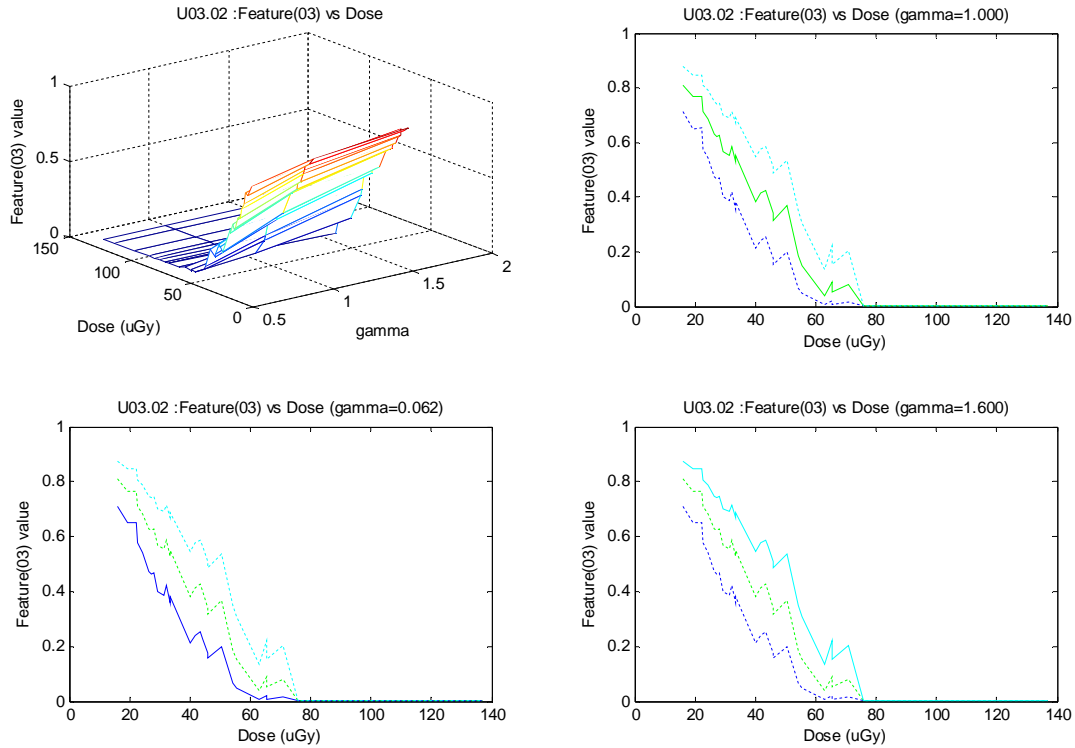


Figure 84: PredModel-2A/B, textural "signature" profile for MEAN feature function at different exposure rates (dose) and gamma correction values, for the background area.

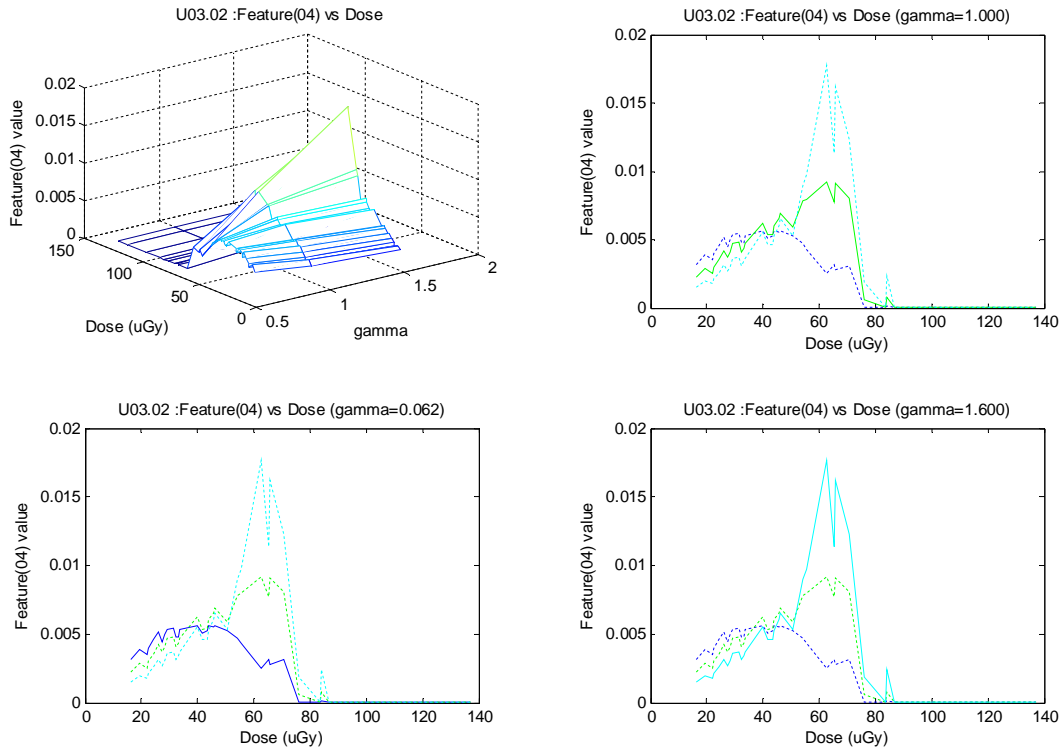


Figure 85: PredModel-2A/B, textural "signature" profile for STDEV feature function at different exposure rates (dose) and gamma correction values, for the background area.

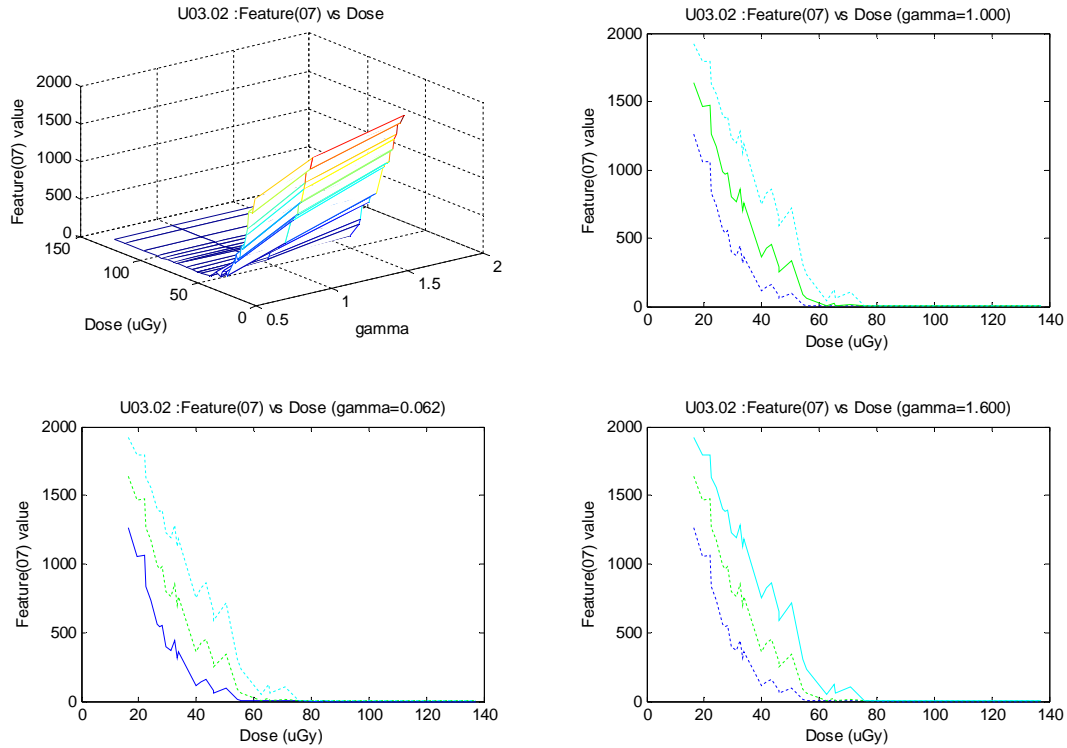


Figure 86: PredModel-2A/B, textural “signature” profile for POWER feature function at different exposure rates (dose) and gamma correction values, for the background area.

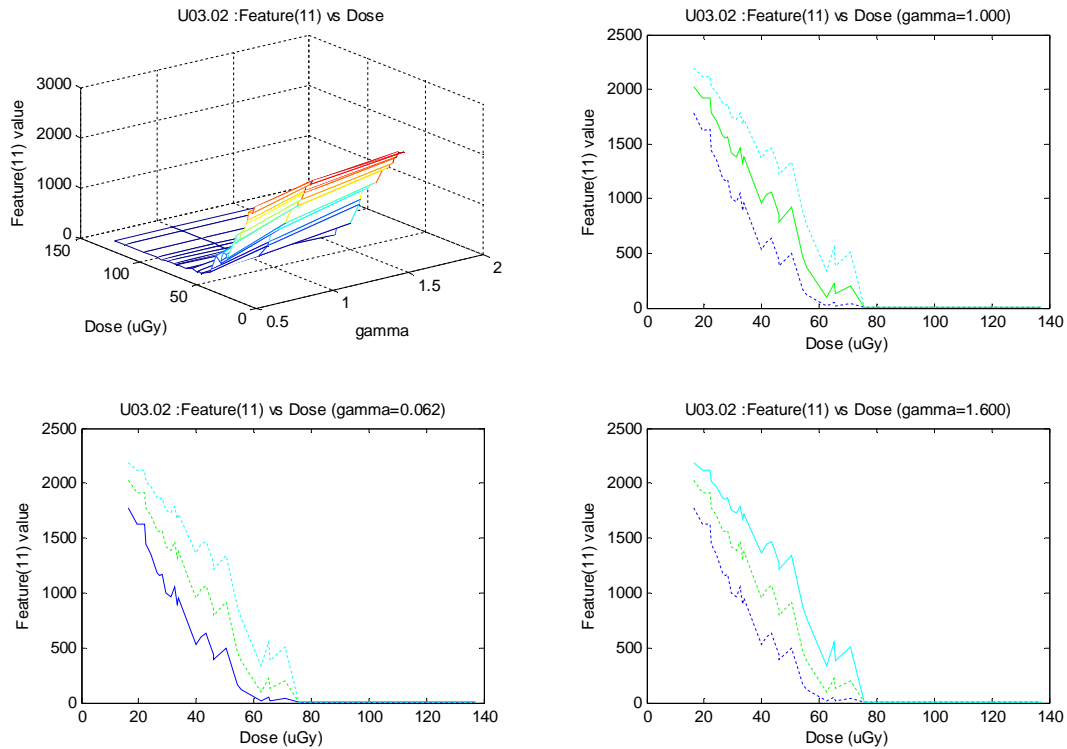


Figure 87: PredModel-2A/B, textural “signature” profile for VOLUME feature function at different exposure rates (dose) and gamma correction values, for the background area.

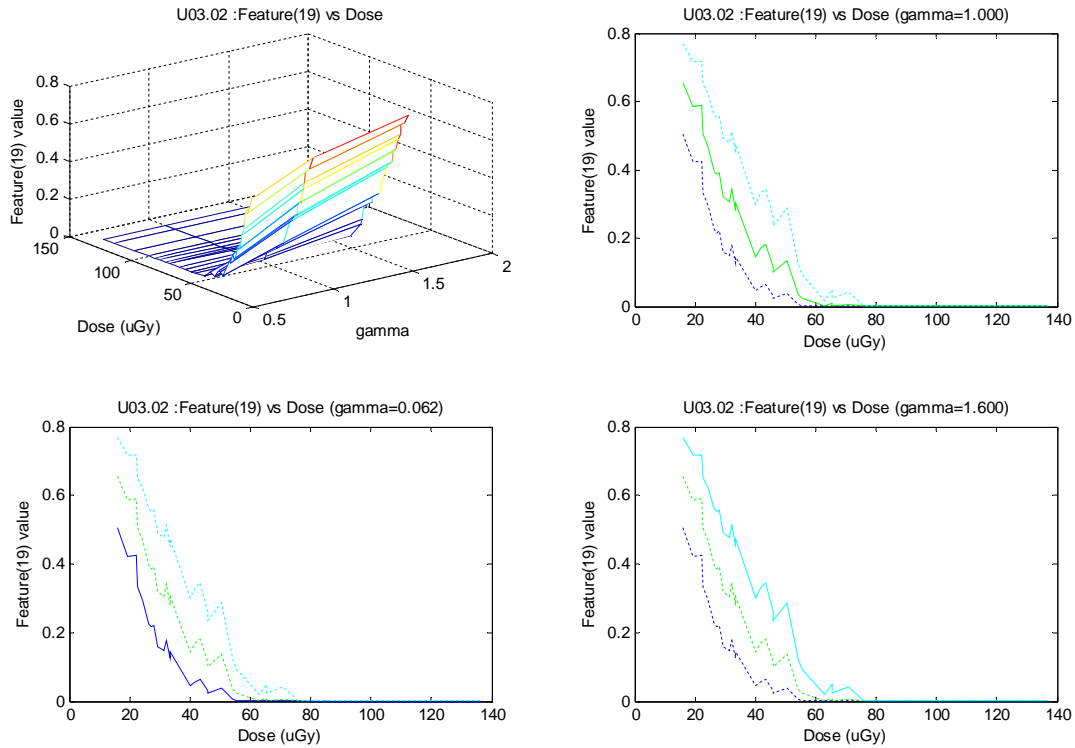


Figure 88: PredModel-2A/B, textural "signature" profile for SF19 feature function at different exposure rates (dose) and gamma correction values, for the background area.

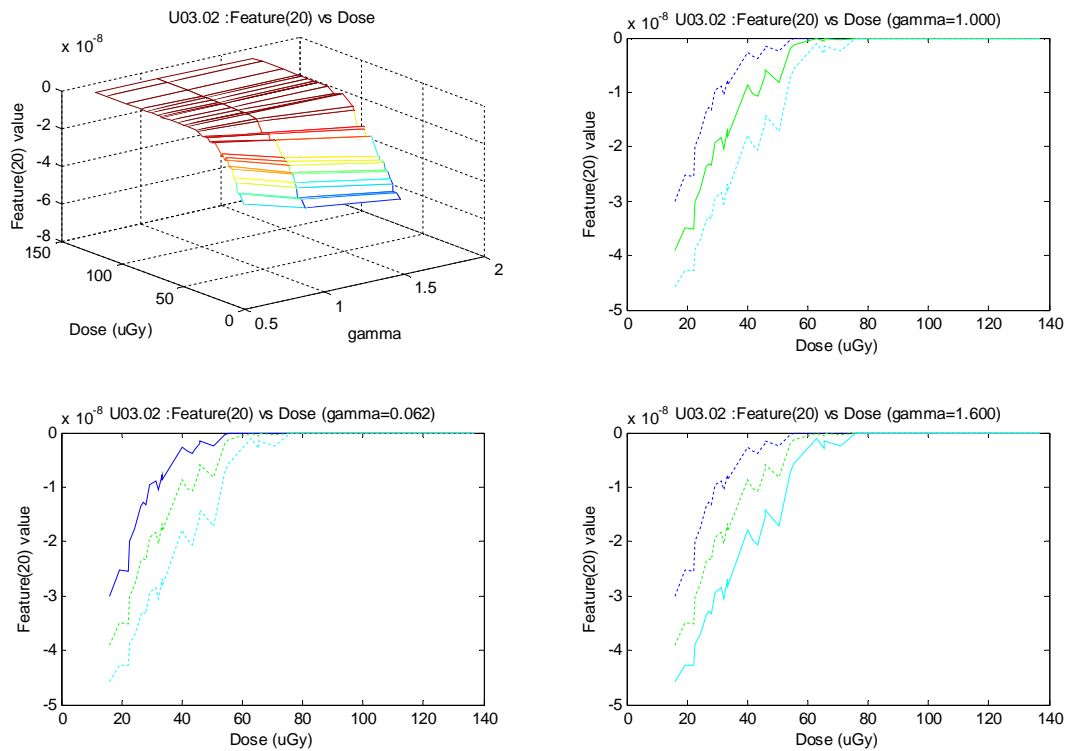


Figure 89: PredModel-2A/B, textural "signature" profile for SF20 feature function at different exposure rates (dose) and gamma correction values, for the background area.

Plots from Figures 82-89, i.e. background texture analysis, can be directly compared to the corresponding plots from Figures 74-81, i.e. normal tissue texture analysis, as they refer to the same image set "U03.02". From these comparative studies it is clear that feature values and the corresponding transition curves were different. Response curves that referred to background texture demonstrated sharper slopes and smoother transitions, over more limited areas of the dose range. Furthermore, the exact feature values for background texture varied over smaller ranges above and below zero, whereas the tissue texture exhibited more extreme values.

Comparative analysis of background and normal tissue areas, conducted for both "U03.02" and "U04.03" image sets, has verified the limited statistical influence of background patterns to the textural feature datasets that were calculated over the tissue areas. Although the inherent statistics are different, the information content of the tissue areas seem to be much higher than that of the background artifacts, that can be considered as a convolution of the expected X-ray noise and the background patterns generated by the perspex layers and the plastic wrappings of the tissue samples. In any case, the signal-to-noise ratio is high enough to validate the feature analysis conducted over the new DB3 image database.

2.9 Textural characterization of images of mammographic test objects

Mammography phantom images, previously acquired at Elettra and at UCL (see WP 3 monthly report for August 2004), were used to investigate possible candidates for indicators of interesting feature presence. The digital images were divided in boxes of different sizes (25x25 – 60x60 pixel²), and the following parameters were tested as potential feature functions:

- 1) standard deviation normalized to mean value (STDn)
- 2) skewness (which is a measure of data distribution symmetry)
- 3) kurtosis (which is a measure of whether the data distribution is peaked or flat relative to a normal distribution)
- 4) maximum gradient (the latter was defined as the maximum absolute value of box derivative: a 2D array containing image box derivative computed row by row)

The effect of some preprocessing procedures on the behavior of important statistical quantities was studied.

It was observed if the ability of a particular parameter in detecting the presence of a well known object increased or decreased after applying one of the following software tools: a cubic spline smoothing algorithm¹, the histogram equalization and a mean smoothing + edge

¹ The cubic smoothing spline s to the given data x, y is constructed, for the specified smoothing parameter $p \in [0..1]$ and the optionally specified weight w . The smoothing spline minimizes

$$p \sum_i w(i)(y(i) - s(x(i)))^2 + (1 - p) \int (D^2 s)^2$$

enhancement linear filter. The latter was used by [A. Bazzani, et.al. "An SVM classifier to separate false signals from microcalcifications", Phys. Med. Biol., Vol. 46, 1561-1663, 2001] in a SVM classifier as a first method step.

It is really important to underline that the standard deviation alone cannot be used, but it is necessary to normalize it to the mean value. In fact, if we take into account for the sake of simplicity only the quantum noise, the image regions without the imaged object have a std value much larger than those regions containing the sample since the number of photons impinging the image receptor is larger for the sample free path in respect to the sample transmission path where the number of photons is drastically reduced due to the absorption inside the phantom. Vice versa, the standard deviation normalized to mean value (STDn), which obeying to Poisson statistics is proportional to the inverse of photon number square root, is lower for sample free image regions. Larger STDn values should therefore indicate those image regions containing non-uniformities due to feature presence.

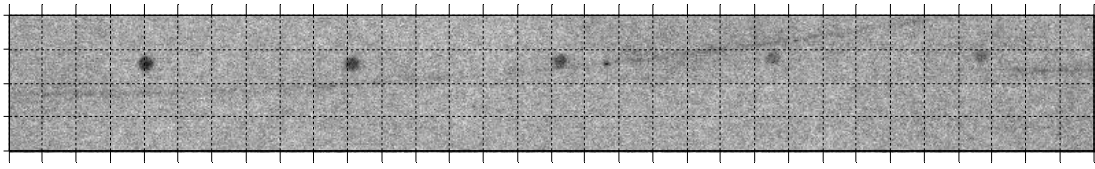
2.9.1 Study of the effect of pre-processing

At first the Leeds phantom image acquired (at 17 keV and 0.6 mGy of Mean Glandular Dose (MGD)) with the imaging plate (IP) was investigated. In particular, the image region containing the high contrast small objects details, which should simulate microcalcifications, was examined. The details size is 0.5 mm and first five of the diminishing contrast series were taken into account. The image reported in figure 90 was divided in boxes of 25x25 pixels² (pixel size=50µm) and the STDn was computed for each box. Figure 91 shows the STDn of each figure 90 25x25 pixels² box plotted row by row. For example STDn of phantom image box row 2 and column 4 (see figure 90) corresponds to the fourth point of STDn plot of data 2 (figure 91). It has to be stated that in all graphs where it is written standard deviation, the latter refers to the STDn. Returning to figure 91 results, the STDn assume larger values for those figure 90 image boxes containing the details. In particular, if the detail is contained in two adjacent boxes, as for the first from left detail of figure 90, the STDn of both boxes assumes a larger value with respect to the background. The STDn resulted dependent on the detail contrast, lower the latter lower the STDn.

Figures 92, 93 and 94 show respectively the skewness, kurtosis and maximum gradient of each figure 90 25x25 pixels² box plotted row by row. The skewness was found to be very sensitive to the detail presence and in respect to the STDn less dependent to their contrast. While, the kurtosis effectiveness in founding the details resulted not particularly promising. The kurtosis max value corresponded to box row 2 and column 15 of figure 90 image, which contains a small dark spot due to IP defect, while the difference between kurtosis values associated to Leeds phantom details and the background was less important than the difference the STDn and the skewness presented between details and background boxes.

with $w=\text{ones}(\text{size}(x))$ the default value for w . For $p = 0$, s is the least-squares straight line fit to the data, while, on the other extreme, i.e., for $p = 1$, s is the variational, or natural cubic spline interpolant. As p moves from 0 to 1, the smoothing spline changes from one extreme to the other.

As visible in figure 94, the maximum gradient was found to be completely inappropriate to reveal the presence of the small contrast objects. Image variations due to noise obscure those due to detail presence. Since the feature recognition has to be done on low dose images, which consequently will be quite noisy, the use of the maximum gradient for feature recognition is useless.



1 4 8 12 16 20 24 28

32

Figure 90. A detail of Leeds phantom image, acquired at 17 keV and 0.6 mGy MGD, containing the small high contrast objects

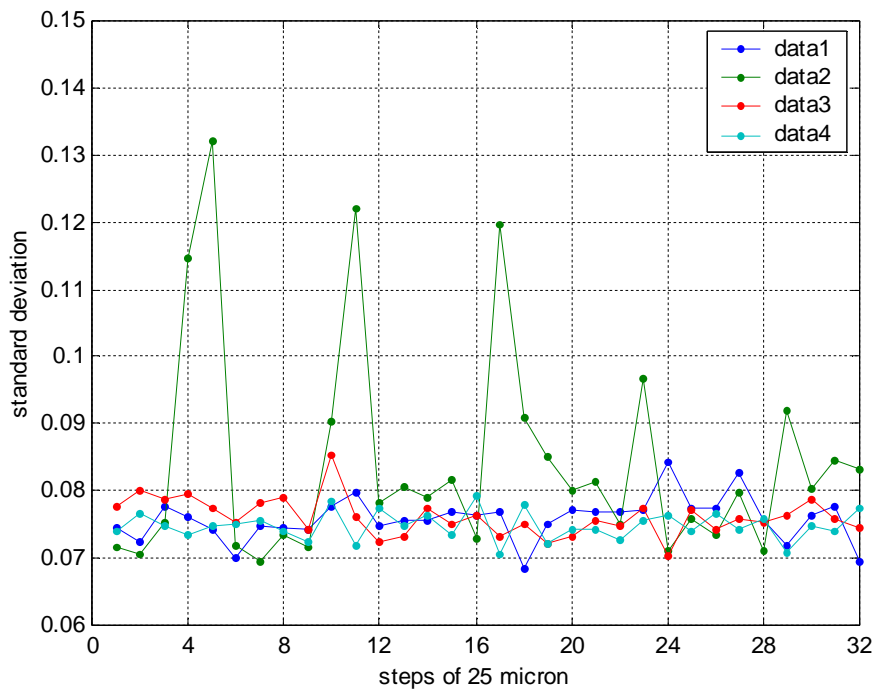


Figure 91. STDn of each Leeds phantom image (figure 90) 25x25 pixels2 box plotted row by row

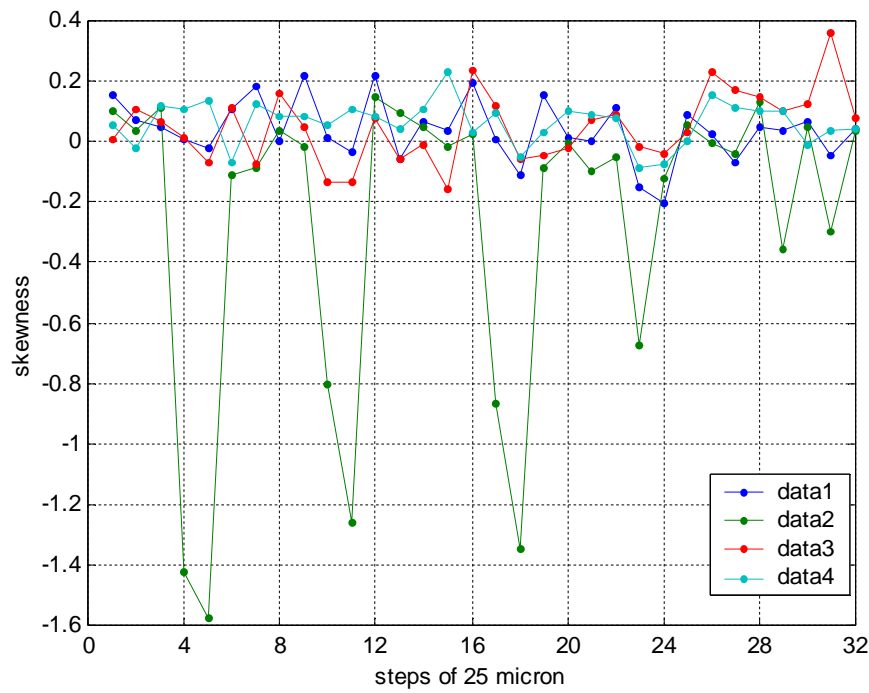


Figure 92. Skewness of each Leeds phantom image (figure 90) 25x25 pixels2 box plotted row by row

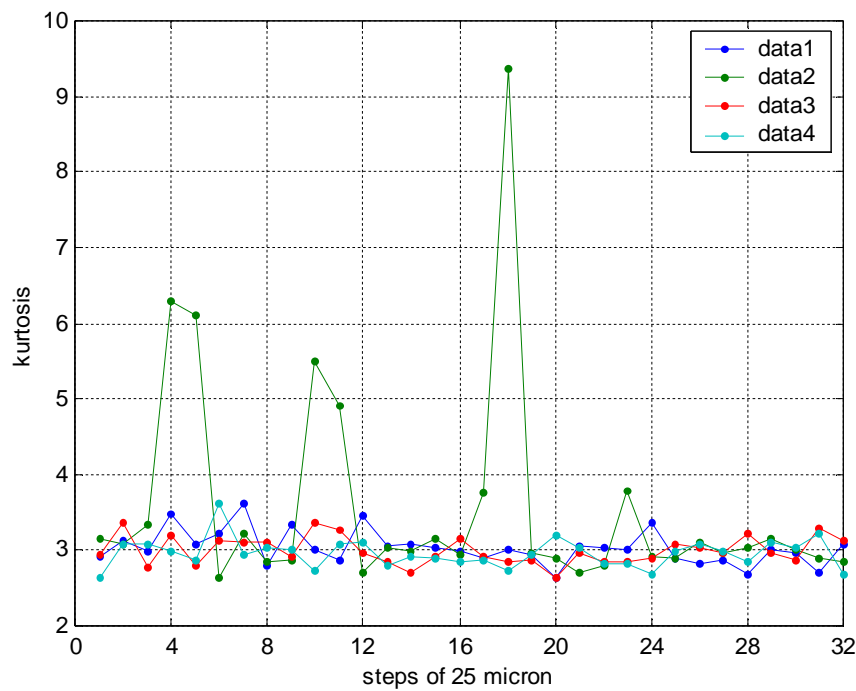


Figure 93. Kurtosis of each Leeds phantom image (figure 90) 25x25 pixels2 box plotted row by row

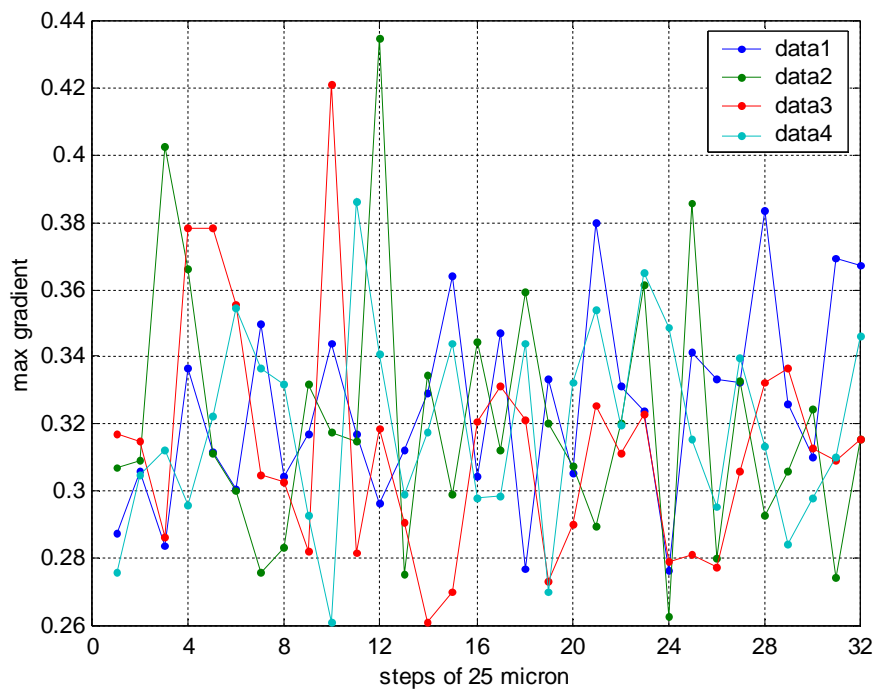


Figure 94. Max gradient of each Leeds phantom image (figure 90) 25x25 pixels2 box plotted row by row

The Leeds phantom detail image was then subjected to a smoothing spline algorithm, which aim is to reduce image noise. Smoothed image is shown in figure 95. As visible in figure 96, which reports maximum gradient of each 25x25 pixels2 box of smoothed phantom image (figure 95), re-computing the maximum gradient evaluation on the smoothed data permits now to 'recognize' the detail presence. The STDn and the skewness were also calculated for the smoothed image (figure 95). The STDn and the skewness of smoothed data are reported respectively in figures 97 and 98. The smoothing spline tool improves the STDn effectiveness in identifying details (figure 97). In fact, the difference between STDn of detail free boxes and those containing them is larger for the smoothed image in respect to the raw one. Whereas the smoothing procedure modifying box data distribution reduces the skewness ability in identifying details (figure 98).

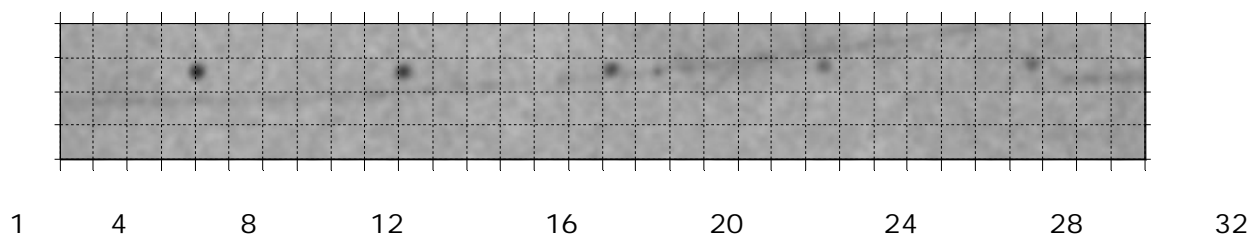


Figure 95. Leeds phantom image (figure 90) subjected to a cubic smoothing spline algorithm

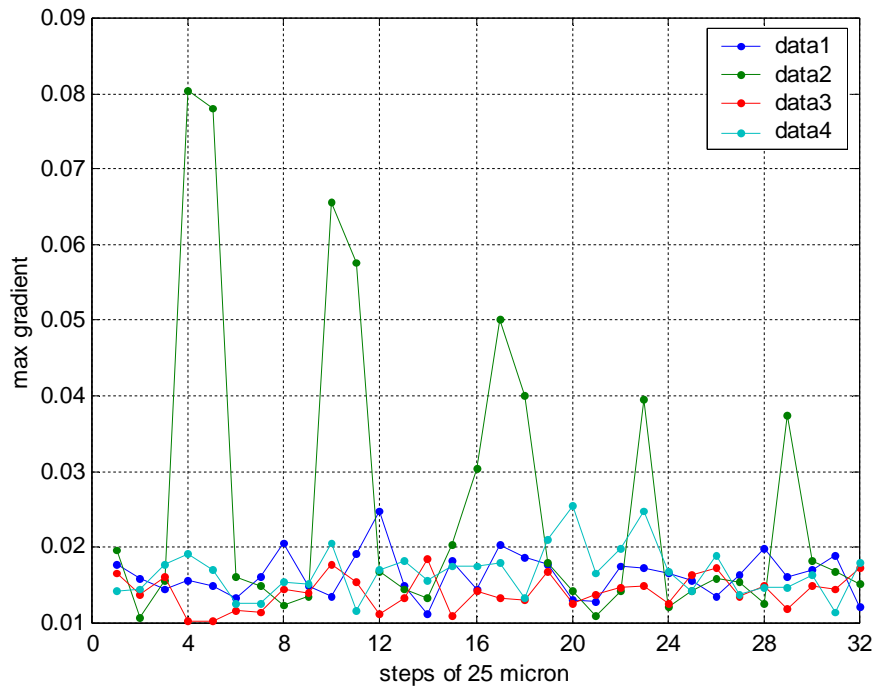


Figure 96. Max gradient of each Leeds phantom smoothed image (figure 95) 25x25 pixels2 box plotted row by row

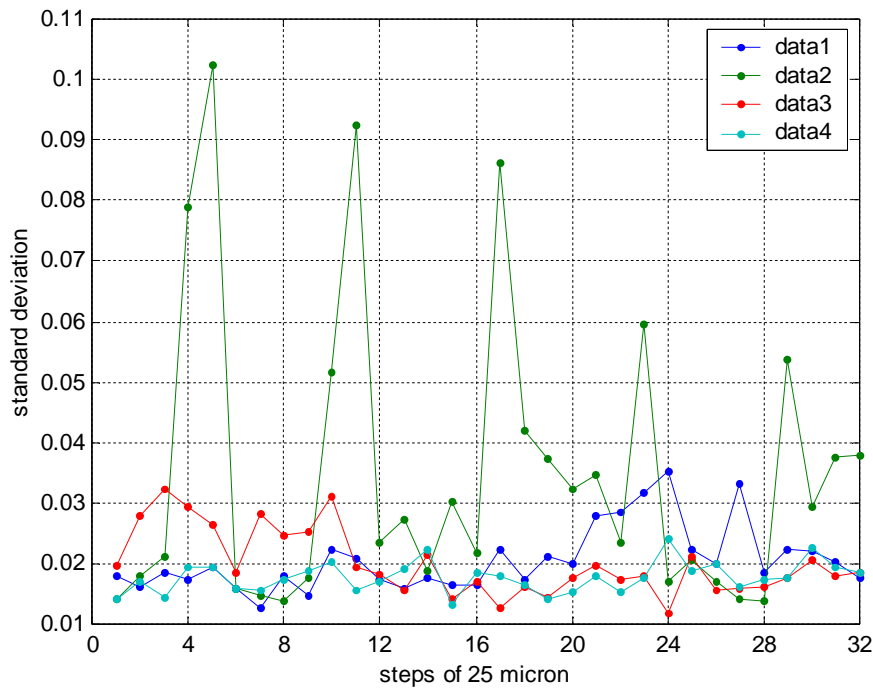


Figure 97. STDn of each Leeds phantom smoothed image (figure 95) 25x25 pixels2 box plotted row by row

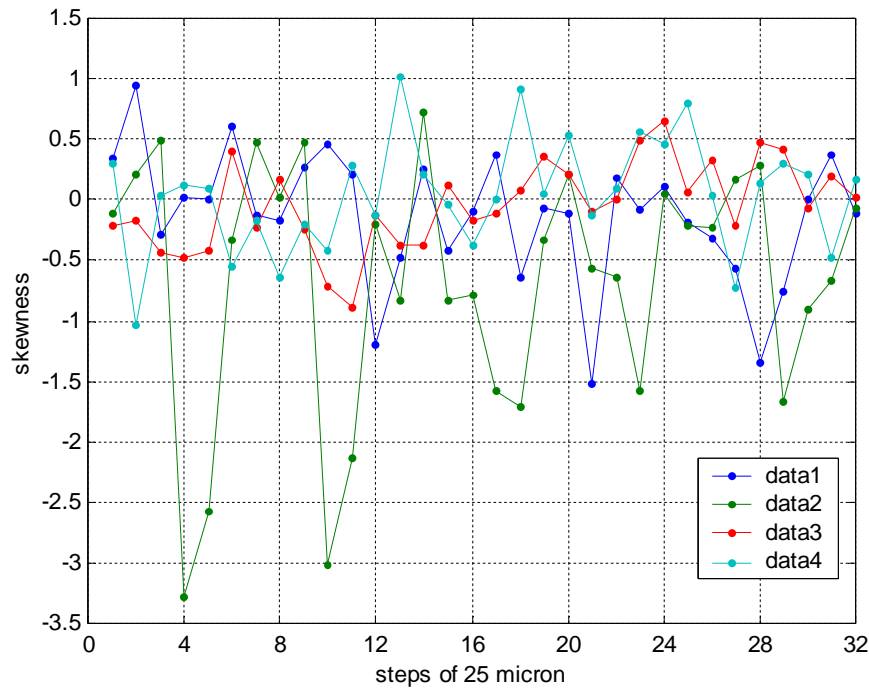


Figure 98. Skewness of each Leeds phantom smoothed image (figure 95) 25x25 pixels2 box plotted row by row

Figure 99 shows Leeds image (figure 90) after a linear histogram equalization. The goal of histogram equalization is to obtain a uniform data histogram by redistributing original intensity distributions. The effect is to improve image contrast. But the effect on STDn and skewness is poor. As visible in figures 100 and 101, which report respectively STDn and skewness of histogram equalized image, the STDn and in particularly the skewness suffer the loss of their capacity in recognizing detail presence after the original data have been subjected to the histogram equalization.

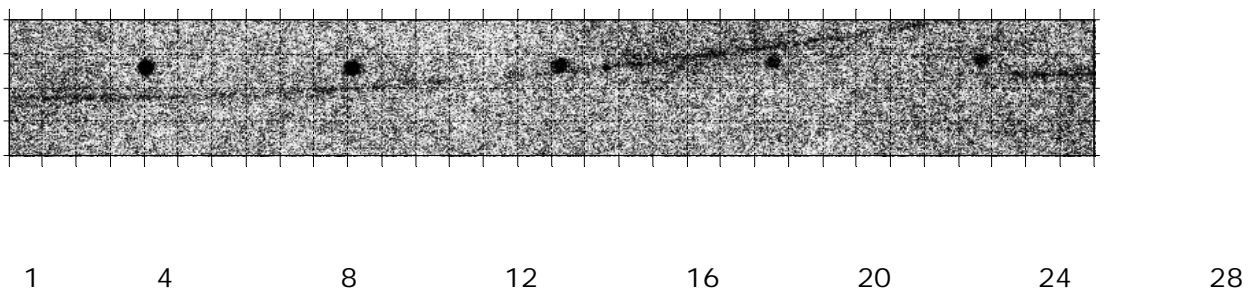


Figure 99. Leeds phantom image (figure 90) subjected to a histogram equalization

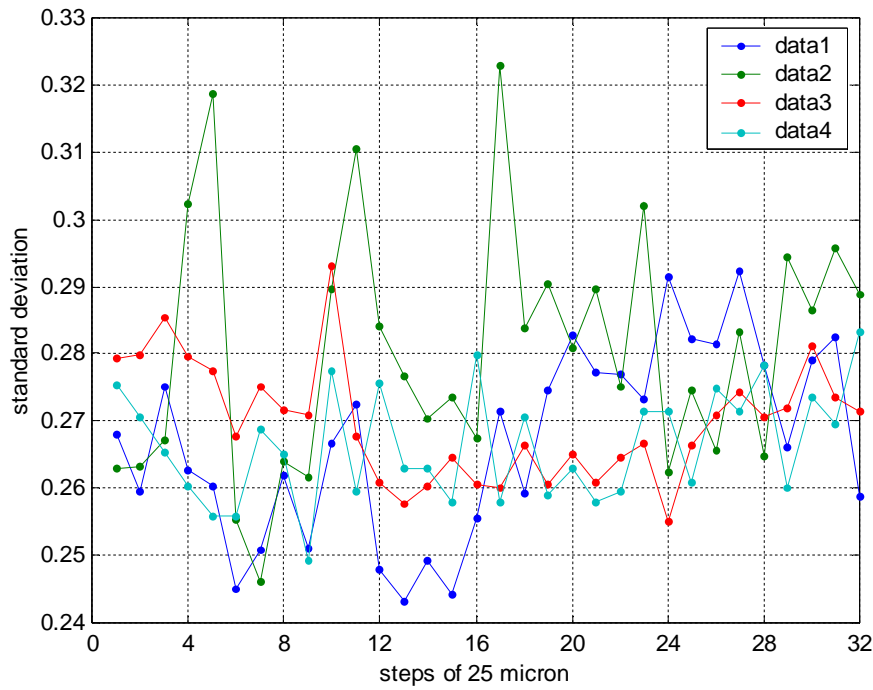


Figure 100. STDn of each Leeds phantom histogram equalized image (figure 90) 25x25 pixels box plotted row by row

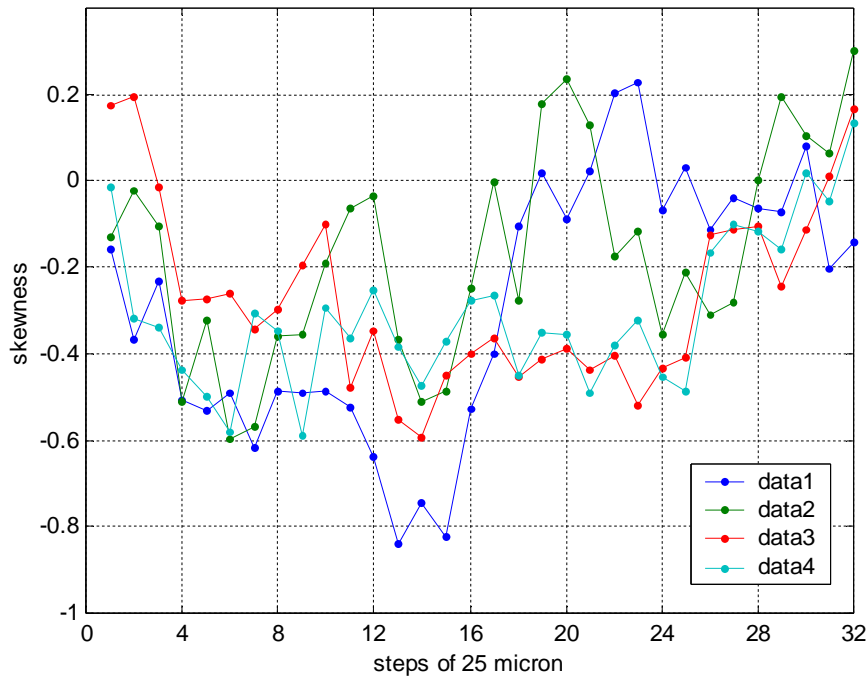


Figure 101. Skewness of each Leeds phantom histogram equalized image (figure 90) 25x25 pixels box plotted row by row

The next tool taken into account was a mean smoothing and edge enhancement linear filter. The principle behind edge enhancement is the hypothesis, that different organs are represented by different pixel intensities, and hence that organ boundaries can be characterized by rapid intensity changes in the image. However, it is obvious that intensity discontinuities may also originate from noise in the image. Therefore, noise must be suppressed by the use of suitable filter kernels, or during edge enhancement itself. In this case a mean smoothing filter, which reduces the amount of intensity variation between one pixel and the next, is used. The effect of the smoothing + edge enhancement filter on the original image is visible in figure 102, while the effect on the STDn and on the skewness is shown in figures 103 and 104, which report respectively the STDn and the skewness of filtered image. The use of the filter does not bring any improvement in both STDn and skewness capacity in reveal detail occurrence. As a matter of fact, the difference between STDn of detail free boxes and those containing them is larger for the raw image in respect to the filtered one. The same holds also for the skewness.

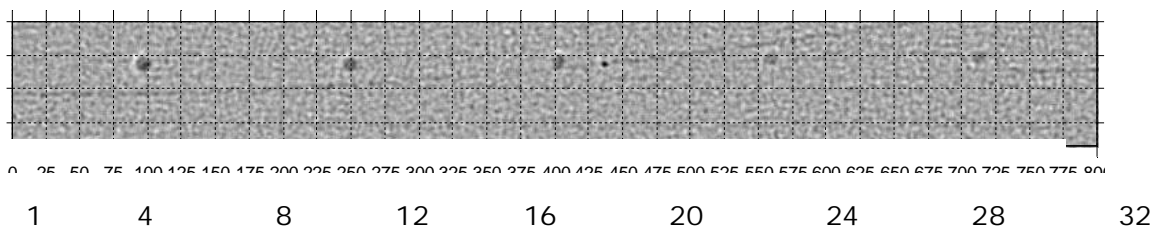


Figure 102. Leeds phantom image (figure 90) subjected to a mean smoothing and edge enhancement filter

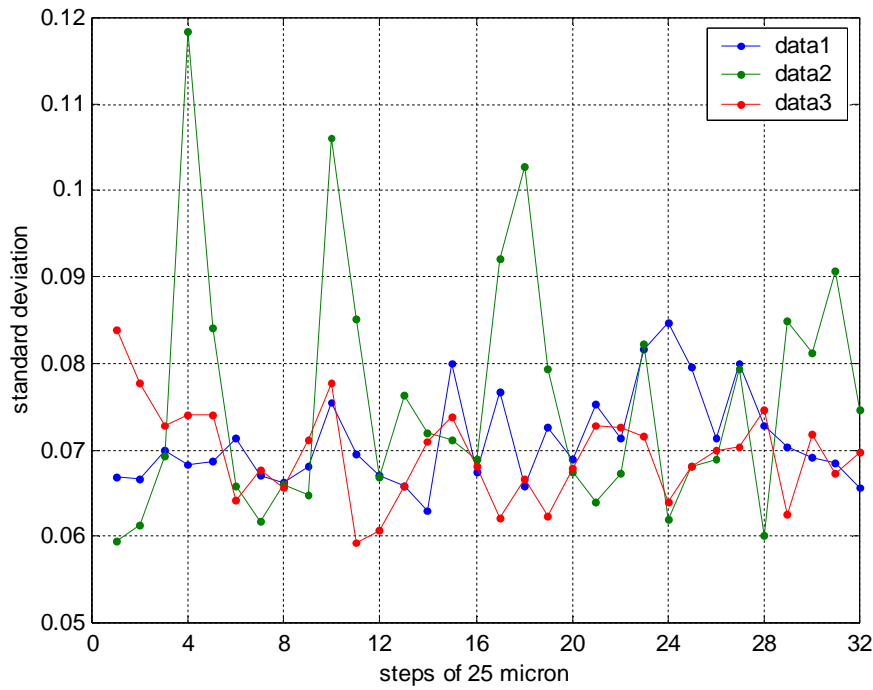


Figure 103. STDn of each Leeds phantom image subjected to a mean smoothing and edge enhancement filter (figure 102) 25x25 pixels2 box plotted row by row

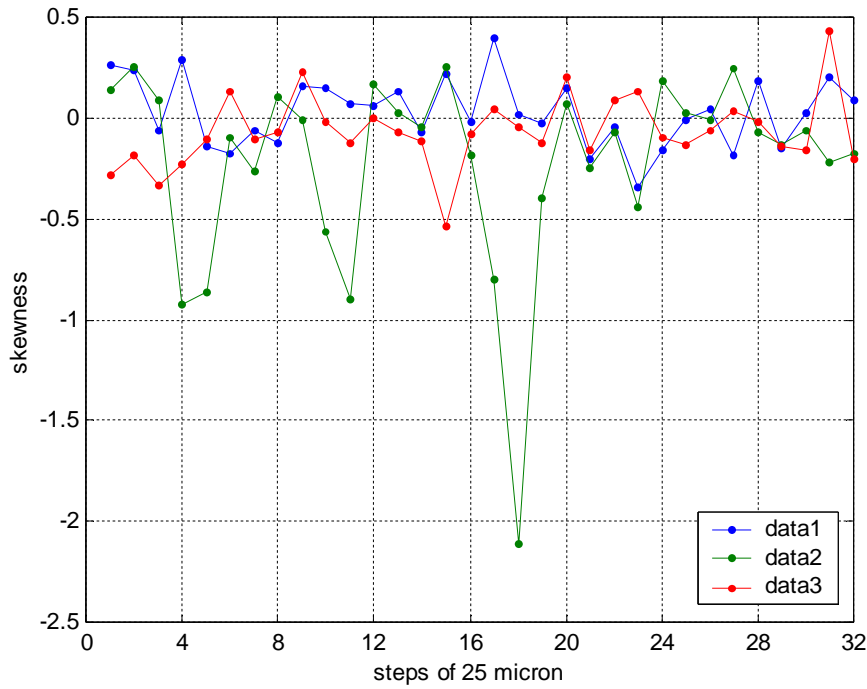


Figure 104. Skewness of each Leeds phantom image subjected to a mean smoothing and edge enhancement filter (figure 102) 25x25 pixels2 box plotted row by row

From this analysis it was not found any particular improvement in subjecting the raw image to the investigated pre-processing tools before using the STDn and the skewness as feature 'extractor'. It is important to underline that these results were found at both the employed energies and for the investigated exposure range.

2.9.2 Study of statistical quantities for feature detection

The utility of the STDn and the skewness was tested on the anthropomorphic phantom ('Rachel') images acquired with the IP. In figure 105(a) is shown the Rachel image (at 17 keV and 0.8mGy MGD), which was subjected to a logarithmic compression. The dynamic range of an image can be compressed by replacing each pixel value with its logarithm. This has the effect that low intensity pixel values are enhanced. Applying a pixel logarithm operator to an image can be useful in applications where the dynamic range may too large to be displayed as it happened with the Rachel phantom linear image. In figures 105 (c) and (d) are reported respectively the STDn and the skewness map of the Rachel image. The STDn and the skewness were computed for 30x30 pixels² boxes of the linear (not log compressed) Rachel image. As in evidence in figure 105(c), the STDn resulted well suited to detect sample boundaries and the regions containing large and not particularly contrasted features. In fact, quite uniform phantom image regions are associated to STDn values lower than those associated to regions containing some features. Also the skewness reveals the sample boundaries. But, differently from the STDn, the skewness resulted not sensitive to large and not particularly contrasted features. However, the skewness was found to be very skilled in recognizing high contrast small objects. Figure 105(b) shows a detail of Rachel phantom image containing two small high contrast objects. The STDn and the skewness values associated to the boxes containing the two small objects are indicated by two arrows in figure 105 (c) and (d). The presence of the two details was clearly put in evidence by the skewness, while it was weakly indicated by the STDn. This aspect can be better highlighted looking at figure 105 (e), where the horizontal profiles extracted from the STDn and the skewness map associated to image regions containing the two small object are reported. The skewness value of a box containing a high contrast small object is drastically lower than the values the skewness assumes in the neighbouring background. As said, the skewness is a measure of data distribution symmetry. The skewness for a normal distribution is zero, and any symmetric data should have a skewness near zero. Negative values for the skewness indicate data that are skewed left and positive values for the skewness indicate data that are skewed right. This characteristic can be also exploited when identifying sample boundaries. Figure 105(f) shows two horizontal profiles extracted from the STDn and the skewness map and related to the Rachel image region containing two phantom edges. Approaching the phantom edge from the background results first in a skewness drop (the box pixel values are mainly those of the background (high pixel values) and there are few phantom low pixel values, which skew the data distribution to left). Exactly at the phantom edge the skewness is near zero (high value pixels are equal in number of low value pixels). While leaving the edge to enter into the sample region results in a skewness value increase. In this case the box pixel values are

dominated by sample low values and the few background high pixel values skews the data distribution to right.

Hence, at the phantom boundaries the skewness assumes the following three values: a minimum (local), a value near zero, a maximum (local). While the STDn assume a maximum at the image box for which the skewness assumes the value near zero (figure 105(e)). Whereas, in the presence of a small high contrast object, the skewness reaches a marked minimum value and the STDn a relatively large value, both at the same image box: that containing the detail.

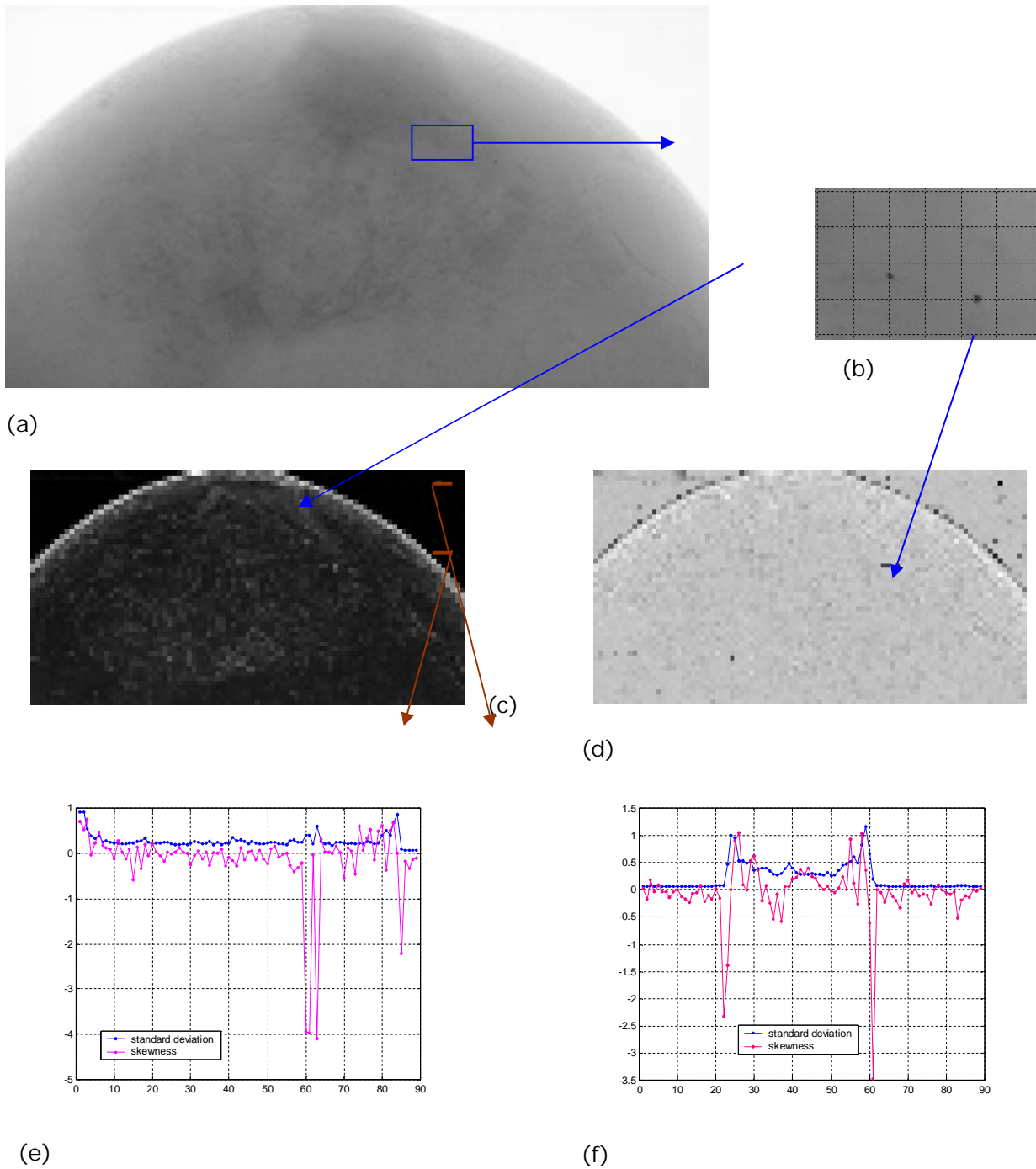
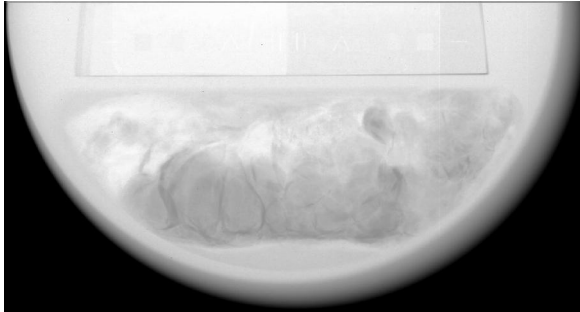
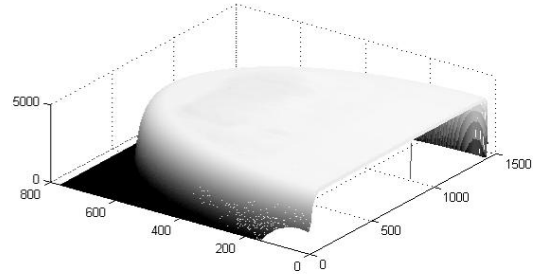


Figure 105. (a) Anthropomorphic phantom 'Rachel' image (log compressed) acquired at 17 keV and 0.8 mGy MGD. (b) A detail of 'Rachel' phantom image containing two high contrast small objects. (c) STDn map of each 'Rachel' phantom image 30x30 pixels² boxes. (d) Skewness map of each 'Rachel' phantom image 30x30 pixels² boxes. (e) STDn and skewness horizontal profiles related to 'Rachel' image region containing the two high contrast small objects. (f) STDn and skewness horizontal profiles related to 'Rachel' image region containing two phantom edges

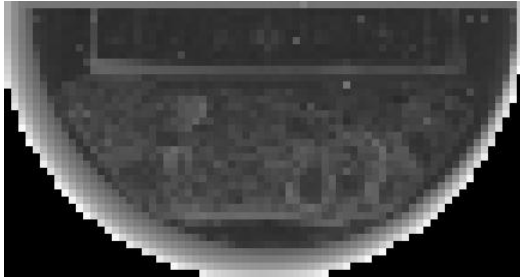
It is also important to point out the fact that the STDn assumes larger values in the image region occupied by the phantom in respect to the background. If the standard deviation alone, without normalization, had been used, the opposite would have happened.



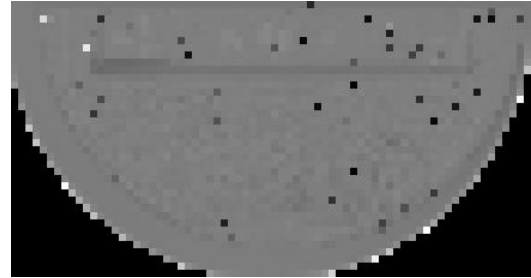
(a)



(b)



(c)



(d)

Figure 106. (a) Bart's phantom image (histogram equalized) acquired at 28 kV and 40 mAs. (b) 3D representation of the Bart's phantom image before applying the histogram equalization. (c) STDn (log compressed) map of each Bart's phantom image 20x20 pixels² boxes. (d) Skewness map of each Bart's phantom image 20x20 pixels² boxes.

The effectiveness of the STDn and the skewness was then tested using the images of the Bart's phantom, which were acquired with an a-Se flat panel detector (FPD) and a conventional x-ray tube. Figure 106(a) shows the Bart's phantom image acquired with 28 kV and 40 mAs. The employed FPD furnishes in output an image, where the original pixel values have been inverted. As a consequence and as visible in figure 106(a), the background (the image regions without the sample) are those with the lowest pixel values. In particular, in the considered image, the background was saturated and is characterized by zero pixel values. The image, only for visualisation purposes, was subjected to the histogram equalization in order to increase the contrast. Figure 106(b) reports a 3D representation of the Bart's phantom image before applying the histogram equalization. The phantom presents a steep edge and the contrast between the sample and the background obscures the image contrast due to the features contained into the sample. In figures 106 (c) and (d) are reported respectively the STDn and the skewness maps of the Bart's phantom image (the original) (figure 106(a)), which was divided in boxes of 20x20 pixels². A box size of 20x20 pixels² was chosen because

the FPD pixel size (127 μm) is quite larger than that of the IP (50 μm). It has also to be stated that figure 106(c) shows the logarithm of the STDn, since the values of the latter corresponding to phantom edges, which are very steep, are considerably larger than STDn values inside the sample. Together with the boundaries, the STDn recognizes the regions containing large and not particularly contrasted features. Also in this case, quite uniform phantom image zones are associated to STDn values lower than those associated to regions containing some features. The latter performance is not provided by the skewness, which instead put in evidence the presence of high contrast objects.

The skewness behaviour at the sample boundaries (with the background) differs from that obtained with the Rachel image (fig.105) since in the Bart's phantom image the background is saturated. As a consequence, a skewness profile related to an image region containing the sample boundaries does not present a minimum-maximum pair in correspondence of the edge, but only a maximum. Returning, to the high contrast small objects, figure 107(a) shows a Bart's phantom image detail containing two dark spikes. As visible in figure 107(b), which magnifies the two details, both the spikes consist of only one low value pixel. The presence of the latter is clearly 'recognized' by the skewness, as in evidence in figure 107(d), which reports the skewness map of Bart's phantom image detail (figure 107(a)). The STDn presents, in correspondence of the two boxes containing the spikes, a value larger in respect to the surrounding boxes, but the relative difference is smaller than the difference between the skewness of dark spike boxes and the background ones.

It has to be underlined that since the image has the pixel values inverted, a dark spike actually corresponds to an exceedingly high pixel value probably due to detector malfunctioning and not to a small contrast object. The latter will be characterized by a bright spike in the final-inverted image. The Bart's phantom image (figure 107(a)) contains also two extremely high pixel values and the skewness related to the image boxes containing those values presents two local maxima.

So the 'sign' of the skewness can identify if a relatively high box STDn value is due to a 'dark' or a 'white' spike. This important result emerged also in the following presented analysis.

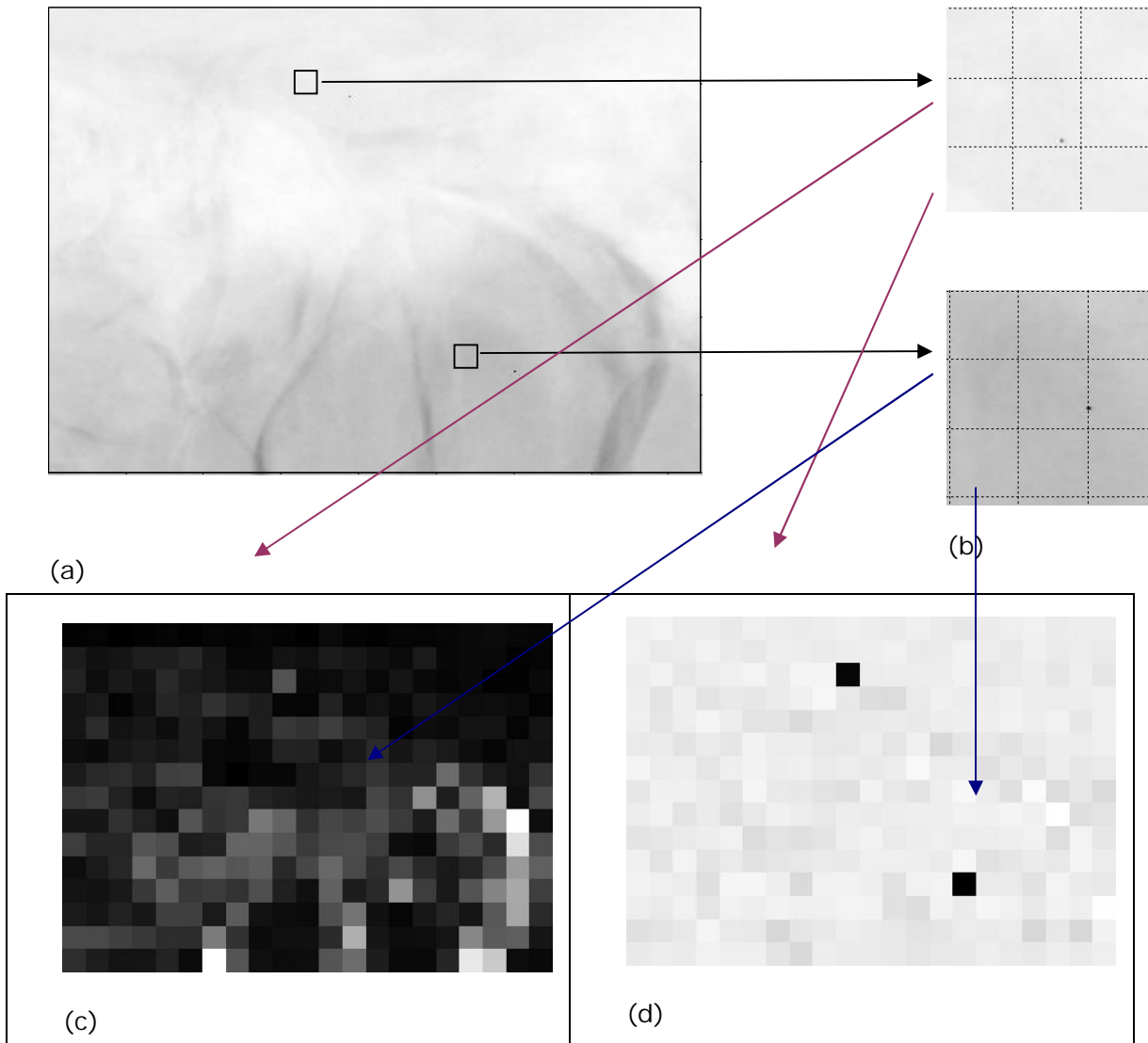


Figure 107. (a) Bart's phantom image detail containing two dark spikes. (b) Magnification of the image regions containing the two dark spikes. (c) STDn of each Bart's phantom image detail (figure 107(a)) 20x20 pixels² boxes. (d) Skewness map of each Bart's phantom image detail (figure 107(a)) 20x20 pixels² boxes.

The third set of investigated images was acquired with the CCD detector and the sample was the Rachel phantom. Since the detector area is quite small (29 x 29 mm²), 2D images of a phantom region were obtained by scanning the sample through the x-ray beam, which was previously aligned with the CCD. The beam height was 3.5 mm, while the scanning step was set equal to 3 mm. In this way every scan contains a part (0.5 mm in height) common to the adjacent one. At first, the image has been reassembled without using this additional information. As visible in figure 108, the 'whole' image consists of two data columns each formed of 23 2045x253 pixels² sub-images. The latter were previously corrected for dark noise (dark noise subtraction) and beam/detector non-uniformities (white field normalization).

The image reported in figure 108 was subjected to a logarithmic compression only for visualization purposes.

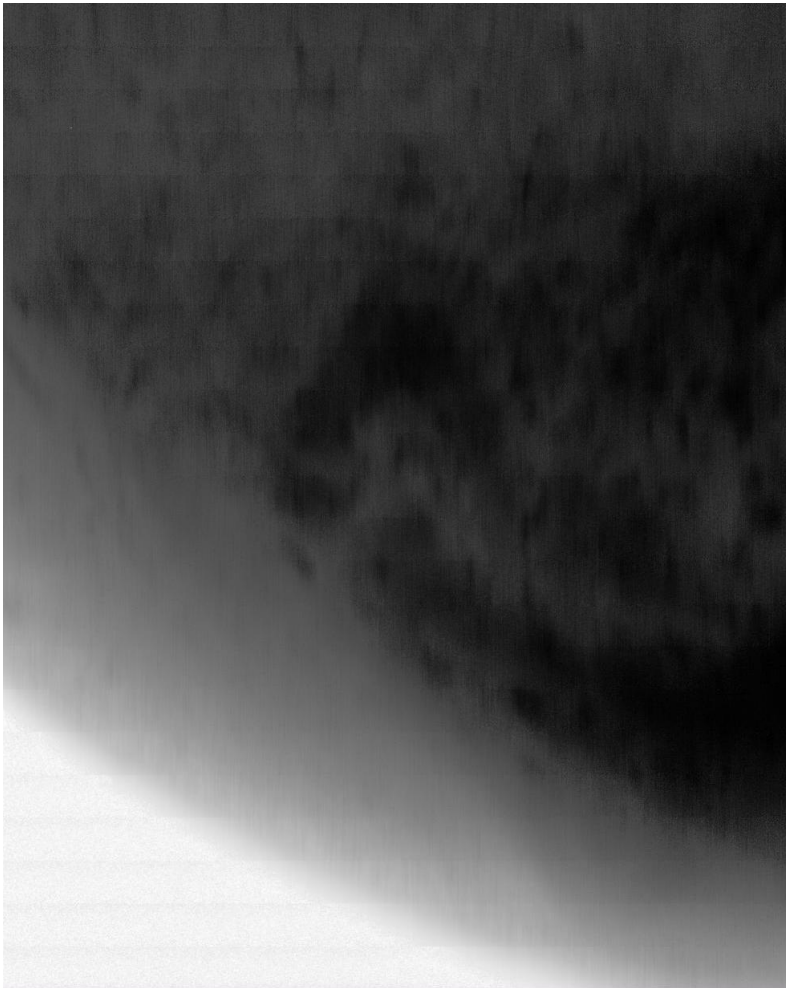


Figure 108. The image (log compressed) of a 'Rachel' phantom region acquired with the CCD at 19 keV and 0.7 mGy MGD.

Figures 109 (a) and (b), show respectively the STDn and skewness map of the Rachel phantom image (figure 108) which was divided in 60x60 pixels² boxes since the CCD pixel size is quite small: 14 μm . The STDn recognizes well the phantom boundaries and the regions containing some extended features. The left-bottom sample side is quite uniform and the corresponding STDn values are lower than the STDn values of the other sample regions. As it pertains the skewness, the latter indicates the sample boundaries and the presence of both dark and bright spikes. Figures 109 (c) and (d), show respectively a 3D representations of sample details regions containing a bright and a dark spike. The arrows in figure 109, show the skewness values corresponding to the boxes containing the above mentioned spikes. The bright spike presents a high (positive) skewness value (significantly larger in respect to the surrounding background), while the dark spike presents a low (negative) skewness value (significantly smaller in respect to the surrounding background). For both the spikes, the associated STDn does not differ from the STDn of the surrounding background. This is due to

the large size of the boxes the image was divided in to compute the STDn and the skewness. Larger the box size, lower the 'capacity' of the STDn to detect the presence of a single pixel spike. While, the skewness ability in detect the presence of a single pixel, which value is quite different from its background, does not suffer from the box size increase.

Figure 109(e) shows the STDn and the skewness profiles corresponding to an image region, which contains a bright spike and the phantom edge. As examined, the skewness value of an image box containing a pixel, which value is quite larger in respect to the other box pixels, is larger than zero. For the same image box, also the STDn should assume a value larger than the STDn of the surrounding background. It has to be underlined that the STDn value depends on the box size and the value relative difference between the bright pixel and the other box pixels. If that difference is small e/or the box size is quite large, the STDn can not reveal the bright pixel presence. As it regards the sample boundaries, the STDn assumes a maximum value in correspondence of a sample edge, while the skewness presents the following sequence: minimum (local), zero and maximum (local) in correspondence of a sample edge. Precisely, as found when analyzing Rachel phantom images acquired with the IP, the skewness value at the image box for which the STDn assumes a maximum, is near zero; while the skewness is considerably large and considerably low in the adjacent boxes.

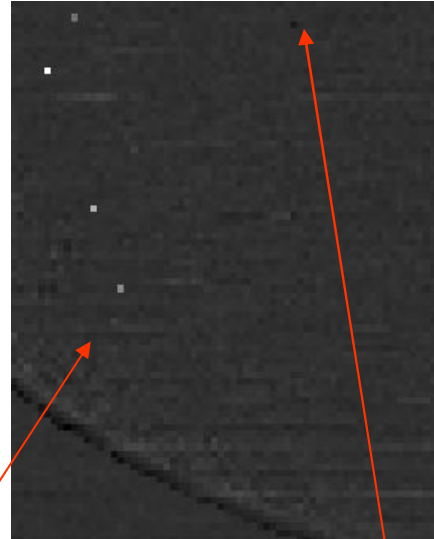
At this point the image reported in figure 108, was 'reconstructed' using the information contained in the overlapping subsequent scans. Each scan was multiplied by a constant in order to render equal the mean value of the common region between two successive sub-images.

Figure 110 shows a detail of the Rachel image after (a) and before (b) the above mentioned correction. The effect of the latter on the STDn and on the skewness was not relevant. In fact, as visible in figure 110, which reports respectively the STDn and skewness of both corrected and not Rachel image detail (figures 110 (c), (d), (e) and (f)), the correction procedure has not brought any significant change in both STDn and skewness values.

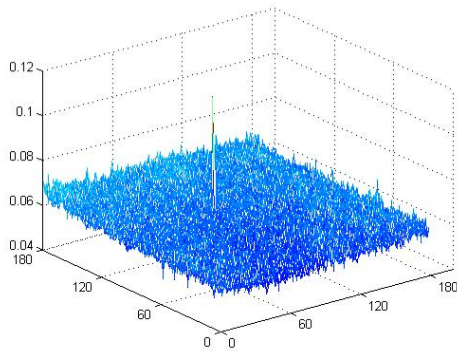
From results emerged in this study, it was found that the kurtosis and the maximum gradient are not suitable to detect feature presence. While, the STDn and the skewness resulted well suited to detect phantom boundaries. In particular the information furnished by the STDn and the skewness can be combined together to better recognize phantom edges. In fact the skewness value at the image box containing half sample and half background pixel values, for which the STDn assumes a maximum, is close to zero; while the skewness is considerably large and considerably low in the adjacent-lateral boxes. Another important result regards the STDn capacity in recognizing the presence of large and not particularly contrasted features. Whereas, the skewness was found to be excellently suited to recognize small (even one pixel) high contrast objects and their nature, i.e. if the object is a dark or black spot. The latter characteristic can permit to distinguish between a detector malfunctioning (associated to an extremely bright spike) and the presence of a microcalcification (associated to a dark spike).



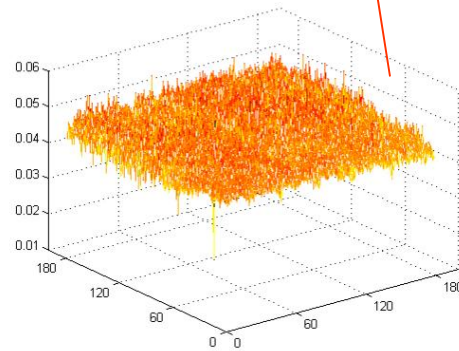
(a)



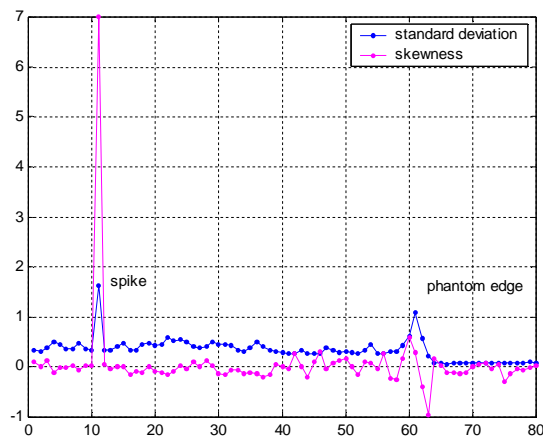
(b)



(c)

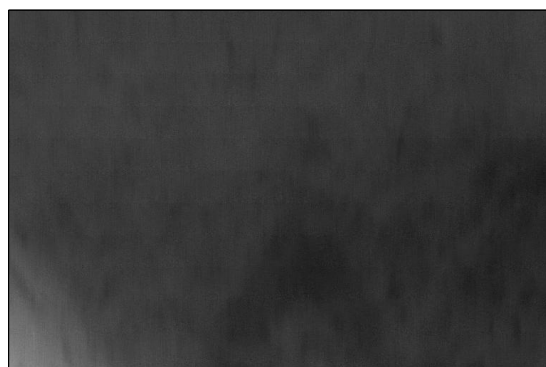


(d)

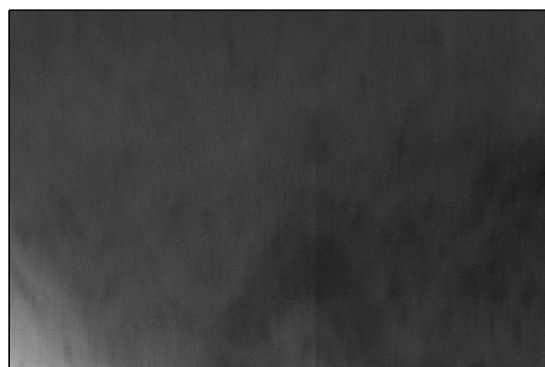


(e)

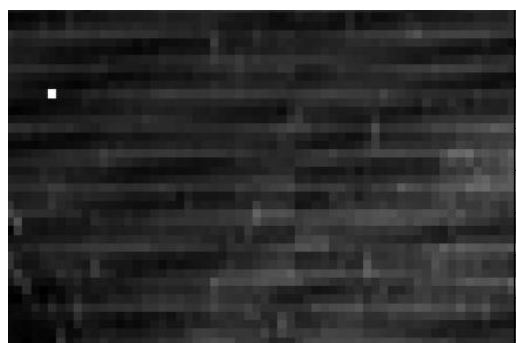
Figure 109. (a) STDn of each 'Rachel' phantom image (figure 108) 60x60 pixels² boxes. (b) Skewness of each 'Rachel' phantom image (figure 108) 60x60 pixels² boxes. (c) 3D representations of 'Rachel' image (figure 108) detail region containing a bright spike. (d) 3D representations of 'Rachel' image (figure 108) detail region containing a dark spike. (e) STDn and skewness vertical profiles corresponding to an image region (figure 108), which contains a bright spike and the phantom edge.



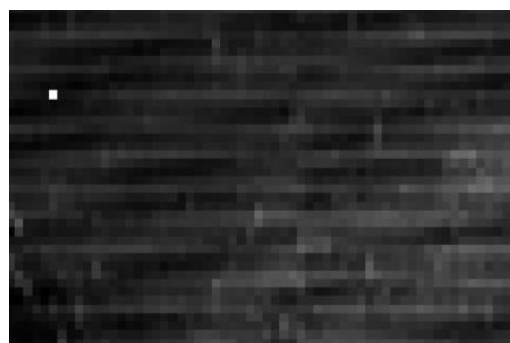
(a)



(b)



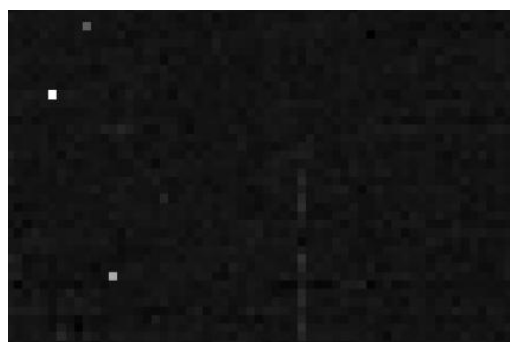
(c)



(d)



(e)



(f)

Figure 110. (a) A 'Rachel' phantom image (figure 108) detail before the correction for adjacent sub-images nonuniformities. (b) A 'Rachel' phantom image (figure 108) detail after the correction. (c) STDn of each figure 110(a) 60x60 pixels² boxes. (d) STDn of each figure 110(b) 60x60 pixels² boxes. (e) Skewness of each figure 110(a) 60x60 pixels² boxes. (f) Skewness of each figure 110(b) 60x60 pixels² boxes

3. Implementation & Performance Issues

In accordance to the proposed sensor IC design and hardware considerations, all texture feature functions were considered under the SIMD architecture and possible consequences in the organization of the final code [18-19].

The basic SIMD architecture requirement is that the code can be effectively executed with multiple instances of input data. In the case of a line-scanning imaging system this means that the pixel data should be able to be processed as they arrive in the buffers, using multiple sensor IC modules that work in parallel processing different parts of the input. It is essential that branching functions and global data access is limited to the absolute minimum, in order to gain the most from parallel data processing in every clock cycle.

The complete set of the 20 feature functions are based on 1st order statistics or similar processing patterns. Even if all 20 functions were to be used in the final system, careful execution planning would enable the complete evaluation of all of them in no more than two stages – the first for calculating all functions that use only raw pixel data as input and the second for calculating the synthetic feature functions that require previous calculation of others first. In any case, the structure of all feature functions is essentially based on a sequential access through the entire set of pixel values currently within the boundaries of the sampling box. This means that the complexity in storage requirements and processing time is always directly proportional to the total number of pixels available at the input: 100 pixels when size is 10x10, 625 pixels when size is 25x25, or 2500 pixels when size is 50x50. Although the choice on sampling box size must be carefully balanced between high-quality texture “signature” and fast processing, the inherent structure of the code remains the same and fully compatible for SIMD implementation.

As a demonstrative example, the following source code excerpts can be used a guideline for translating any of the feature functions from Matlab (original source) into C/C++ source code and finally into Assembly for IC programming:

MATLAB sample:

```
function npower=func_SF19( I )  
    npower = sum(sum(I.^2))/(size(I,1)*size(I,2));
```

C/C++ sample:

```
int func_SF19( unsigned char *pixel, int boxsz )
{
    int    i, j, sum=0, px, npower;

    for ( i=0; i<boxsz; i++ )
        for ( j=0; j<boxsz; j++ )
        {
            px = *(pixel+(i-1)*boxsz+j);
            sum = sum + px*px;
        }

    npower = sum / (boxsz*boxsz);
    return(npower);
}
```

x86 Assembly sample:

```
...
DSEG      SEGMENT

BOX_SZ    DW      50
ICOUNT    DW      50
JCOUNT   DW      50
SUMDW     0
NPOWER    DW      0

DSEG      ENDS
...

FUNC_SF19 PROC

    PUSHA

    MOV     SUM,0

L1: CMP     JCOUNT,0
    JNG     L0

L2: CMP     JCOUNT,0
    JNG     L1
    MOV     DI,JCOUNT
    MOV     BX,ICOUNT
    SUB     BX,1
    MUL     BX,BOX_SZ
    MOV     AX,PIXEL[BX][DI]
    MUL     AX,AX
```

```
ADD    SUM,AX

SUB     JCOUNT,1
JMP     L2

SUB     ICOUNT,1
JMP     L1

L0:MOV  AX,BOX_SZ
MUL     AX,AX
MOV     CX,AX
MOV     AX,SUM
DIV     CX

MOV     NPOWER,CX

POPA

RET

FUNC_SF19 ENDP
```

In general, preliminary analysis through PredModel-1A, PredModel-1B and PredModel-2A/B has proven that efficient low-level texture analysis is possible with limited computational resource requirements. Consistent performance profiles against exposure settings can be formulated when using even single feature functions that relate to complexity and structural analysis, thus constituting a solid base for the design of a feedback loop for real-time control.

4. Further Progress Requirements

The current study for textural feature functions evaluation was initially based on a typical set of mammographic images that were used as the base for an exposure simulation model. Later, a new set of breast tissue images was employed to validate the analysis results and the initial feature functions selection.

In order to complete the general specifications for the design of the control loop, including the sensor IC and the X-ray profiles, experts' quality assessment over the entire set of breast tissue images is essential in order to identify the clinically optimal acquisition parameters and, subsequently, match the response curves of the selected feature functions to the expert's one [20].

Final stages of subsequent work should be focused, but not limited to, the following major issues:

1. Acquire a complete set of experts' quality assessment over the entire set of breast tissue images (DB3).
2. Investigate the statistical correlation of the response curves between the selected feature functions and the experts' one.
3. Define a complete set of transformations, including any pre-processing on the raw image data, as well as the feature datasets, in order to realize the required matching towards the response curve of the expert's quality assessments.
4. Define a complete set of rules, thresholds and profiles for the implementation of a realistic sensor IC intelligent control module, for dental and mammographic applications.
5. Investigate alternative approaches and levels of providing higher levels of intelligence in the sensor/imaging system through the application of sophisticated image processing.

Suggestive References:

- [01] J Suckling et al (1994) "The Mammographic Image Analysis Society Digital Mammogram Database" *Excerpta Medica, International Congress Series 1069*, pp375-378.
<http://www.wiau.man.ac.uk/services/MIAS/MIASweb.html>
- [02] ACR (1999) "ACR Standard for the performance of screening mammography", *ACR Standards - Screening Mammography*, pp.201-208.
- [03] ACR (2001) "ACR Standard for the performance of whole breast digital mammography", *ACR Standards - Whole Breast Digital Mammography*, pp.213-218.
- [04] M.A.Périard, P.Chaloner, "Diagnostic X-Ray Imaging Quality Assurance: An Overview", *Radiation Protection Bureau, Environmental Health Directorate Health Protection Branch, Health Canada*, (1996).
- [05] RANZCR Mammography QC Manual – Physicist's Test Sheets.
- [06] J.H.Launders, S.M.Kengyelics, A.R.Cowen, "A comprehensive image quality evaluation of a selenium based digital X-ray imaging system for thorax radiography", *Med.Phys.* 25(6) 1999, pp.986-997.
- [07] S.Vedantham, A.Karellas, S.Suryanarayanan, "Full breast digital mammography with an amorphous silicon-based flat panel detector: Physical characteristics of a clinical prototype", *Med.Phys.* 27(3) 2000, pp.558-567.
- [08] O.Pawluczyk, B.J.Augustine, M.J.Yaffe, et.al., "A volumetric method for estimation of breast density on digitized screen-film mammograms", *Med.Phys.* 30(3) 2003, pp.352-364.
- [09] A.Miettinen, M.Pirinen, "The dose and image quality in mammography practice in Finland", *STUK-B-STO 52 / Dec.2003*, Radiation and Nuclear Safety Aauthority, Finland.
- [10] K.Bliznakova, Z.Bliznakov, V.Bravou, "A three-dimensional breast software phantom for mammography simulation", *Phys.Med.Biol.* 48 (2003) 3699–3719.
- [11] C.J.Martin, D.G.Sutton, P.F.Sharp, "Balancing patient dose and image quality", *Applied Radiation and Isotopes*, 50 (1999) pp.1-19.
- [12] P.Duvauchelle, N.Freud, "A computer code to simulate X-ray imaging techniques", *Nucl.Instr.Meth.Phys.Res., B* 170 (2000), pp.245-258.
- [13] R.M.Haralick, K.Shanmugam, I.Dinstein, "Textural features for image classification", *IEEE Trans.Sys.Man.Cyb.*, Vol.SMC-3, No.3, Nov.1973, 610-621.
- [14] R.M.Haralick, "Statistical and structural approaches to texture", *Proc.IEEE*, Vol.67, No5, May 1979, 786-804.
- [15] L.V.Ackerman, A.N.Mucciardi, et al., "Classification of benign and malignant breast tumors on the basis of 36 radiographic properties", *Cancer*, Vol.31, 1973, 342-352.
- [16] M.Mavroforakis, H.Georgiou, D.Cavouras, et.al., "Textural Features and Descriptive Diagnostic Data in Mammographic Mass Classification", 14th Int.Conf.DSP, 2002.

- [17] Peter R. Massipust, *Fractal Functions, Fractal Surfaces and Wavelets*, Academic Press, 1994.
- [18] Joar Martin Østby, "Low level image processing from a hardware perspective – The SIMD approach for a general hardware framework", SINTEF ICT, Jun.2003.
- [19] Joar Martin Østby, "Key-points about SIMD and digital intelligence for the WP3 participants", SINTEF ICT, Jun.2003.
- [20] S.Theodoridis, D.Cavouras, H.Georgiou, "I-ImaS: Preliminary Analysis Report and Proposed Design", Dept. of Informatics & Telecomm., Univ. of Athens, Greece, Mar.2004.
- [21] S.Theodoridis, D.Cavouras, H.Georgiou, "I-ImaS: Preliminary Analysis Report and Proposed Design", Dept. of Informatics & Telecomm., Univ. of Athens.
- [22] A.Peterzol, "I-ImaS report on image analysis", Dipartimento di Fisica, Università degli Studi di Trieste.

APPENDIX A

RIEDS – Radiographic Imaging Evaluation & Documentation System

Site:		Survey Date	
		Medical Physicist	
X-Ray Unit Manufacturer		Contact	
X-Ray Unit Model		Email	
Last QC Report Date		Signature	

I-ImaS

Intelligent Imaging Sensors for
Industry, Health and Security

RIEDS – Radiographic Imaging Evaluation & Documentation System version 1.2

Documentation set:

- Form A: X-ray Equipment Specifications Assessment
- Form B: Image Acquisition – Experiment Settings
- Form C: Image Acquisition – Experiment Logging
- Form D: Image Quality Evaluation – Technician’s QC
- Form E: Image Quality Evaluation – Physician’s QC – Mammo
- Form F: Image Quality Evaluation – Physician’s QC – Dental

Results:

Images Acquired: _____
Image Resolution (pixels): _____
Graylevel Depth (bits): _____
Detailed Equipment Description: ☐ YES ☐ NO

RIEDS – Radiographic Imaging Evaluation & Documentation System
version 1.2

I-ImaS

Intelligent Imaging Sensor for Industry, Health and Security

Workpackage-3

Contact: Harris Georgiou, xgeorgio@di.uoa.gr

1. Introduction

As part of the I-ImaS project, the RIEDS prototype (Radiographic Imaging Evaluation and Documentation System) is the basic tool for planning and executing a series of radiological experiments for image sets acquisition. It contains a package of template documents in the form of data sheets that are to be filled before, during and after the image acquisition process.

The main goals for having a detailed set of documentation and logging templates are related to quality control, backtracking information and explicit image annotation, all necessary for the construction of images that employ high quality and detailed descriptions.

The RIEDS prototype includes a total of 6 template sheets for documenting various aspects and parameters of the equipment, the data acquisition environment and the retrieved images. Specifically, these sheets are:

- Form A: X-Ray Equipment Specifications Assessment
- Form B: Image Acquisition – Experiment Settings
- Form C: Image Acquisition – Experiment Logging
- Form D: Image Quality Evaluation – Technician's QC
- Form E: Image Quality Evaluation – Physician's QC (Mammo)
- Form F: Image Quality Evaluation – Physician's QC (Dental)

The system is concluded with additional electronic data container files that are filled after processing the data, as well as a prototype experiment planning chart that is constructed after defining the goals of the experiments and the specifications of the equipment.

2. Identification Codes

The RIEDS uses a detailed set of unique identifiers for all the elements involved in the experiment. Specifically, codes are applied for the project name, the equipment, the target used as the X-ray subject, the experiment runs and the image sets acquired. There are no strict rules on naming conventions for these identifiers, however the naming rules should be applied consistently and provide uniqueness.

For I-ImaS, the following naming conventions could be used:

- Project ID: "I-ImaS" (common name used throughout the documents)
- Machine ID: Lxx (latin letter identifying location + two-digit numeric code)
 - UCL: L="U", xx=10...19
 - Trieste: L="T", xx=20...29
 - ACTA: L="A", xx=30...39
- Target ID: zz (location-specific X-ray subject identifier)
- Test Set ID: NNN (set of images acquired under similar equipment settings)
- Image ID: nnnn (unique image identifier within the current test set)

Based on these naming conventions, the combined Unique Image Identifier (UID) can be constructed as follows:

< ProjectID . MachineID . TargetID . TestsetID . ImageID >

For example: "I-ImaS.U10.01.003.0023" can be translated as image No 23 of set No 3, depicting subject #1 on equipment No 10 at UCL.

All the UID codes should be accompanied with accurate timestamps, containing at least date information. For compatible date/time representation, the ISO 8601 standard format can be used for date-only representation, e.g. the "YYYY-MM-DD" format can be used.

3. Phase A – Experiment Planning

Before conducting the experiment, several properties have to be identified and documented, in order to log the exact characteristics of equipment and to plan the required experiment settings.

Form A is used to record the equipment specifications. There are specific fields for logging the tube potential (kVp) and tube current (mA or mAs) ranges, usually required to distribute the acquisition parameters and plan the experiment. Other equipment-related parameters include focal spot sizes, filtering properties, grid properties, detector specifications, etc. Output image characteristics are described by pixel size, spatial resolution and graylevel depth. Finally, there are additional fields for recording AERC settings available, optical density modes, etc.

After the equipment characteristics are recorded in every detail, Form B can subsequently be used to record the exact settings of these equipment-related parameters that are involved in the experiment. These settings are considered fixed and common throughout the entire experiment, thus there is no need to include them along with every single image set that is acquired but instead record them once for the entire experiment.

Using the information from Form A and Form B, specifically the data related to the tube capabilities in kVp and mAs ranges, the exact settings can be planned and noted in the corresponding Experiment Planning Chart.

4. Phase B – Image Acquisition

During the experiment, acquired images are annotated using Form C. The fields contain information about the initial exposure settings set by the technician, the true values used (may differ slightly from the initial), as well as dose measurements. The same sheet can be used to record multiple images or entire test sets.

As the full UID naming convention might be too lengthy for the actual file names, the acquired images can be stored with a shorter abbreviation of the UID, for example using the "TestsetID.ImageID" part as the file name and the rest of the UID as a hierarchical directory structure for organizing the storage of the complete set. Image format should be chosen carefully for lossless and optionally compressed storage, as it may affect future work on data quality and software development.

5. Phase C – Image Evaluation

After the images are acquired and stored, they are evaluated by trained radiologists, as well as expert physicians of the specific medical field.

Form D contains technical measurements on the acquired image, specifically related to image quality. Resolution is considered through spatial resolution (SR), high-contrast resolution (Hi-CR) and low-contrast resolution (Lo-CR). True intensity if the projected target is measured via optical density values inside (OD1) and outside (OD2) the disc. Finally, there is also a subjective evaluation of noise level (rms%), as well as beam quality measurements (HVL – Half Value Length). The same sheet can be used to record multiple images or entire test sets.

Forms E and F are used by the expert physicians on the specific field of study, specifically mammograms and dental images, in order to produce a detailed image

quality evaluation with regard to various clinical aspects and content-related features of the image. Integer ranking grades are noted in a symmetric range between -5 and +5. If less detailed ranking is needed, the active range can be limited accordingly, e.g. between -2 and +2. Due to the extent of the ranking tables needed for detailed image quality characterization, one sheet is used per image.

6. General Guidelines

All documents included in the RIEDS prototype were created in accordance with standard quality control assessment procedures, employed in periodic equipment validations in real clinical environments [1]. Although RIEDS is focused on image quality evaluation, rather than quality control for the equipments, the same rules apply with regard to consistency in using it as an annotation tool.

For maximum integrity and usability of the resulting data, as well as the acquired X-ray images, it is recommended that properly trained personnel are used when conducting and documenting the experiments.

References

- [1] RANZCR Mammography QC Manual – Physicist's Test Sheets

RIEDS / FORM A: X-Ray Equipment Specifications Assessment

Machine ID²:		Project ID¹:	
Site:			
X-Ray Unit Manufacturer			Survey Date
X-Ray Unit Model			Medical Physicist
Last QC Report Date			Contact
		Email	
		Signature	

Tube Potential	kVp	Minimum Setting	Maximum Setting	Step Setting	Nominal Setting	
Tube Current	mA	Minimum Setting	Maximum Setting	Step Setting	Nominal Setting	
	mA					
	mAs					
Focal spot size	μm	Minimum Value	Maximum Value	Nominal Value		
Magnification factor		Minimum Value	Maximum Value	Nominal Value		
Filter types available		Mo/Mo	Mo/Rh	Rh/Rh	W/Re	Other (specify)
		Y N	Y N	Y N	Y N	
Filter thickness	mm					
Grid types available		Configuration 1	Configuration 2	Configuration 3		
Grid thickness	mm					
Detector type						
Detector size	cm x cm	Configuration 1	Configuration 2	Configuration 3		
Pixel size	μm					
Number of Pixels	p x p					
Spatial Resolution	lp/mm					
Scan time		Minimum Value	Maximum Value	Nominal Value		

	sec			
Effective Exposure Time	msec	Minimum Value	Maximum Value	Nominal Value
Matrix size	p x p	Setting 1	Setting 2	Setting 3
Graylevel depth	bits/pixel			
AERC modes available		Configuration 1	Configuration 2	Configuration 3
Optical Density modes		Minimum Setting	Maximum Setting	Step Setting
Comments				

RIEDS / FORM B: Image Acquisition – Experiment Settings

Project ID¹:		Target ID³:
Machine ID²:		Experiment ID⁴:
Site:		Survey Date
		Medical Physicist
Contact		Signature
Email		

Tube Potential	kVp	Minimum Setting	Maximum Setting	Step Setting	Nominal Setting	
Tube Current	mA	Minimum Setting	Maximum Setting	Step Setting	Nominal Setting	
	mAs					
Focal spot size	µm	Setting Used				
Magnification factor						
Filter type used		Mo/Mo	Mo/Rh	Rh/Rh	W/Re	Other (specify)
	<input checked="" type="checkbox"/>	<input type="checkbox"/>	<input type="checkbox"/>	<input type="checkbox"/>	<input type="checkbox"/>	
Filter thickness	mm					
Grid type		Configuration Used				
Grid thickness	mm					
Detector type						
Detector size	cm x cm	Configuration Used				
Pixel size	µm					
Number of Pixels	p x p					
Spatial Resolution	lp/mm					
Matrix size	p x p					
Graylevel depth	bits/pixel					

AERC mode	Default: OFF	
Optical Density mode (AERC: on)	Default: OFF	
Target Used		
Target model		
Target type		
Target diameter	mm	
Target thickness	mm	
Comments		

RIEDS / FORM C: Image Acquisition – Experiment Logging

Machine ID²:		Project ID¹:		Target ID³:	
Site:		Survey Date		Experiment ID⁴:	
		Medical Physicist		# of Images	
Contact		Signature		Current Page	
Email				Total Pages	
				Test Set ID⁵:	

EMULSION		SETTINGS				RESULTS					
		Values Set				True Values				Air Kerma	MGD
Image ID ⁶	Filename	kVp	mA	sec	mAs	kVp	mA	sec	mAs	mGy	mGy

RIEDS / FORM D: Image Quality Evaluation – Technician's QC

Machine ID²:		Project ID¹:		Target ID³:		
Site:			Survey Date		Experiment ID⁴:	
			Medical Physicist		# of Images	
Contact			Signature		Current Page	
Email				Total Pages		
				Test Set ID⁵:		

EMULSION		IMAGE QUALITY EVALUATION								
		Resolution			Intensity				Noise	Beam Quality
Image ID ⁶	Filename	SR	Hi-CR	Lo-CR	OD1	OD2	Diff(2-1)	Diff (%)	rms (%)	HVL

RIEDS /FORM E: Image Quality Evaluation – Physician’s QC Mammography Template

Project ID¹: Machine ID²: Site:	Target ID³: Experiment ID⁴: Survey Date Medical Physicist Signature
Contact Email	

Test Set ID⁵:

Image ID⁶:

Image Quality Property	Scale										
	−5	−4	−3	−2	−1	0	+1	+2	+3	+4	+5
Typical Measurements											
Contrast Estimation											
Spatial Resolution Estimation											
Noise Estimation (%)											
Normal Elements											
Background / Tissue Discrimination											
Structural Details (veins, etc)											
Fatty Tissue (compressed+uncompressed)											
Dense Tissue (fibro-granular)											
Pectoral Muscle											
Main Boundary Edges (breast)											
Abnormal Elements (if present)											
Masses											
Spiculate Formations											
Micro-calcifications											
Stellate Lesions											
Asymmetric Density											
Asymmetric Ducts											
Axillary Nodes											
Lymphadenoma Patterns											
Other: _____											

RIEDS /FORM F: Image Quality Evaluation – Physician’s QC Dental Template

Project ID¹: Machine ID²: Site: Contact Email		Target ID³: Experiment ID⁴: Survey Date Medical Physicist Signature
Test Set ID⁵:	Image ID⁶:	

Image Quality Property	Scale										
	-5	-4	-3	-2	-1	0	+1	+2	+3	+4	+5
Typical Measurements											
Contrast Estimation											
Spatial Resolution Estimation											
Noise Estimation (%)											
Background / Tissue Discrimination											
Intraoral Elements											
Teeth Enamel and Dentine											
Caries Lesion											
Periodontal Lesions											
Periapical Lesions											
Bone											
Bone Lesions											
Soft Tissues											
Restoration Materials											
Extraoral Elements											
Bone											
Teeth											
Soft Tissues											
Sharpness											
Slice Thickness											
Other: _____											

RIEDS: Experiment Planning Chart

Page of [illegible]

APPENDIX B

PredModel-1A:

Sample source code for textural feature functions (Matlab)

```
%-----  
  
function val=f_tex_min( I )  
  
val = min( I(:) );  
  
%-----  
  
function val=f_tex_max( I )  
  
val = max( I(:) );  
  
%-----  
  
function val=f_tex_mean( I )  
  
val = mean( I(:) );  
  
%-----  
  
function val=f_tex_std( I )  
  
val = std( I(:) );  
  
%-----  
  
function val=f_tex_skewness( I )  
  
if min(I(:)) == max(I(:))  
    val = 0;  
else  
    val = skewness( I(:) );  
end  
  
%-----  
  
function val=f_tex_kurtosis( I )  
  
if min(I(:)) == max(I(:))  
    val = 0;  
else  
    val = kurtosis( I(:) );  
end  
  
%-----  
  
function val=f_tex_power( I )  
  
%val = sum(sum(I.^2))/(size(I,1)*size(I,2));  
%val = sum(sum(I.^2));
```

```

%-----

function H=f_tex_hist( I, Nbins )

QI=floor(normalize(I(:),'minmax')*Nbins);
H=zeros(1,Nbins);
[maxi,maxj]=size(QI);
for i=1:maxi,
    for j=1:maxj,
        k=QI(i);
        if (k<1), k=1; end;
        if (k>Nbins), k=Nbins; end;
        H(k)=H(k)+1;
    end;
end;
H=H/(maxi*maxj);

%-----

function val=f_tex_entropy( I, Nbins )

H=f_tex_hist(I,Nbins);
s=0;
for i=1:length(H),
    if (H(i)>0), s=s+H(i)*log(H(i)); end;
end;
val=s;

%-----

function val=f_tex_zccount( I, ZClev )

[maxi,maxj]=size(I);
c=0; zcv=zeros(1,4);
for i=2:maxi,
    for j=2:maxj,
        zcv(1:4)=[(I(i-1,j-1)-ZClev) (I(i-1,j)-ZClev) (I(i,j-1)-ZClev) (I(i,j)-
ZClev)];
        if (length(find(zcv<=0))>0), c=c+1; end;
    end;
end;
val=c;

%-----

function val=f_tex_surf( I )

val=size(I,1)+size(I,2)-1;
for x=1:size(I,2)-1,
    for y=1:size(I,1)-1,
        val = val + 1 + abs(I(x,y)-I(x+1,y)) + abs(I(x,y)-I(x,y+1));
    end;
end;

```

```
        end;  
end;  
  
%-----  
  
function val=f_tex_vol( I )  
  
val = sum( I(:) );  
  
%-----
```